On the Influence of Small-Scale Topography on Dense Plumes, with a Special Focus on the Filchner Overflow Plume

Elin Darelius
PhD Thesis in Physical Oceanography

Geophysical Institute
University of Bergen
Norway

2007

Pour toi.

Abstract

Dynamical processes of importance to dense overflow plumes are studied, with a special focus on the Filchner Overflow plume, Antarctica. The Filchner Overflow Plume consists of cold and dense Ice Shelf Water formed under the Filchner-Ronne Ice Shelf in the southwestern Weddell Sea, which spills over the sill of the Filchner Depression at a rate of 1.6 Sv.

The influence of small-scale topography on plume paths and mixing is explored theoretically and experimentally, and it is shown that submarine ridges, like canyons, can steer dense plume water downslope. An analytical model describing the topographically steered flow is developed and applied to a number of idealized ridge topographies, allowing for an estimation of their transport capacity, i.e. the maximum amount of water that they can channel downslope. Model results are compared with observations from the Filchner area and with laboratory experiments, and they agree well. The secondary circulation associated with these flows is visualized and measured in the laboratory using a Laser Doppler Velocimeter. The model is applied to two prominent ridges crosscutting the continental slope in the Filchner area, and their transport capacity is estimated to be 0.3 and 0.6 Sv respectively; a substantial part of the total outflow. The effect of topography (ridge, canyon, smooth slope) and flow regime (laminar, eddy, wave) on mixing was studied experimentally. It was found that for the topographically steered flows the increased entrainment rate was more important than the increased descent rate and that the total mixing increased. The small-scale topography proved to have a larger impact on mixing than the large-scale characteristics of the flow. Dense overflow plumes are an important link in the large-scale ocean circulation and we show that small-scale topography (10 km) has a large impact on the plume-path and entrainment and that it should be considered when describing or modeling these flows.

In addition, data from moored instruments and CTD data from the Filchner region are analyzed. The mooring data show pronounced oscillations in the temperature and velocity records with periods of about 35 hours, 3 days and 6 days that existing theories cannot explain satisfactorily. The oscillations are generally barotropic, episodic and strongest east of the two ridges. Twenty-five years of CTD data are synthesized to give a mean picture of the plume, and these data do not support the three plume pathways proposed in previous work.

Acknowledgements

Writing a thesis is not a one-man job, and I owe you all many thanks for finishing mine. First and foremost a large *TACK* to Anna, without whom I would have given up a long time - and many equations - ago, and also to my other supervisors, Svein and Tor, who have been helpful and supportive wherever they, or I, have been in the world. My years as a PhD-student have brought me a long way - literally. Thanks to everyone who made that possible - to BCCR, WUN and Meltzer for financial support, and to Anders S. for taking care of my banana tree while I was away. Many thanks to Peter R. for inviting me to Seattle and UW, to Eric for turning me into an experienced lab-rat and canyon-sculpturer (worthy of being on the list next to Slartibartfast!), and to Eleanor for sharing your windowless office and selling my bike. Thanks to Gregory and Anna for bringing me along for a ride on the rotating table in Grenoble, to Samuel and Henry for technical assistance and for the introductory course in laboratory French, to Justin for sharing frustrations over hotel towels and French codexes and to Anders E. for the long, late, rotating hours. Thanks to Svein for arranging my participation on the scientific cruise to Antarctica, where I learned how cold AABW really is. Thanks also to Inger and SvD for letting me take part in their work during two busy but wonderful weeks in Stockholm, to Keith for welcoming me at BAS and Cambridge and to Povl and Tjarda for housing me there. A thank you also to everyone who has arranged summer-schools and meetings in Bremerhafen, Finse, Longyearbyen, Grindelwald, Liège, Oslo, Cambridge, Bornö, Geilo... I am grateful to Lars, who let me use his model and who patiently explained to a non-modeler/non-fortraner how it works and how to get it running, and to everyone who was been involved in the collection and preparation of the observational data that I have used.

"Borta bra men hemma bäst" - thanks to all and everyone at GFI and BCCR for turning three years of hard work into good memories. A special thank to Arne, Karolina, Lars-Henrik, Knut, Idar, Ilker, Tor E., Peter H. and Karen for inspiring discussions, help, and careful reading of manuscripts, and to everyone at the "young table" in the canteen for many good laughs. A special thank to Brita, for kindly installing and reinstalling my computer... and to Morten for not doing so. Many thanks also to Cathy who proofread the thesis.

"Livet är inte bara geofysik" - thanks to everyone who made me remember that life is not all about cold water and advection terms - thanks to friends and family, to Fabien, who stepped into my canoe - and my heart - a few weeks before the work of this thesis started, and who will stay there long after it is done, to Karolina, Siri and Kristel for making Tverrgaten the best place to live, to Astrid for keeping me warm and green, to Karen, Anna and Connie for help and support when I really needed it, to everyone who has joined me *"på tur"* in a beautiful Norway, to Lenny and Didier for convincing Fabien to go with them to Turkey and the Red river... and finally to Norwegian for flying Bergen-Paris non-stop.

Bergen August 2007

Contents

Paper II: Topographic steering of dense overflows: laboratory experiments with V-shaped ridges and canyons

Paper III: Mixing in density currents induced by submarine canyons and ridges

Paper IV: On the structure and variability of the Filchner Overflow plume

1 Outline

This study investigates dynamical processes of importance to dense overflow plumes, with a special focus on the Filchner Overflow, Antarctica. The study is based on laboratory experiments as well as theoretical work and data analysis and does, to some extent, focus on topographic steering or the influence of small-scale topography to the plume. Short term variability and plume mixing are also covered.

The thesis consists of an introduction and four manuscripts. The introduction provides the scientific background (Section 2) and presents the study and a summary of the manuscripts (Section 3). It concludes with a discussion of the main results and future perspectives (Section 4). The appendices (A-B) contain complementary work not included in the manuscripts.

The four manuscripts are listed below:

- **Paper I:**
  Downward flow of dense water leaning on a submarine ridge
  E. Darelius and A.K. Wåhlin
  Deep Sea Research, Volume 56, Number 7 (2007)

- **Paper II:**
  Topographic steering of dense overflows: laboratory experiments with V-shaped ridges and canyons
  E. Darelius
  Manuscript

- **Paper III:**
  Mixing in density currents induced by submarine canyons and ridges
  A.K. Wåhlin, E. Darelius, C. Cenedese and G. Lane-Serff
  Submitted to Deep Sea Research

- **Paper IV:**
  On the structure and variability of the Filchner Overflow plume
  E. Darelius, L.H. Smedsrud, S. Østerhus, A. Foldvik and T. Gammelsrød.
  Manuscript

Paper I is devoted to submarine ridges and presents an analytical model showing that they, like submarine canyons, can steer dense water downslope. Laboratory experiments supporting the theoretical model - applied to both ridges and canyons - are presented in **Paper II**, while **Paper III** describes another set of laboratory experiments exploring the effect of topography on mixing and entrainment. In **Paper IV** the structure and variability of the Filchner Overflow plume is described based on data from current meter moorings and CTD (Conductivity-Temperature-Depth) measurements.

2 Scientific background

2.1 The role of dense overflow plumes in ocean circulation and climate

In the present climate, all deep oceans are filled with cold water originating at high latitudes (Orsi & Whitworth 2004, Warren 1981). Cooling and salinification through freezing and brine rejection in polar regions produce cold, dense water masses that sink and eventually flow equatorward at depth (Rahmstorf 2006, Rumford 1800). Meanwhile, light and warm surface water flows poleward, closing the much simplified loop (MacDonald & Wunsch 1996) that is commonly referred to as the thermohaline circulation (THC) (Wunsch 2002, Broecker 1997). The THC transports heat poleward[1] and has a central role in the climate (Rahmstorf 2006). The overflow sites, where dense water enters an ocean basin through a gap or a strait, are regions of major water mass transformation (Price & Baringer 1994) and important links in the THC, partly determining the long-term thermohaline equilibrium of the oceans and their dynamical response to changes in climatic forcing. Willebrand et al. (2001) compared results from models of the North Atlantic using three different numerical ocean models. Despite similar initial conditions and identical forcing, the results differed greatly, not only in details but also in important large-scale features such as the strength and properties of the thermohaline circulation. The authors concluded that the results, to a large extent, were dependent on the models' representation of the overflows in the Greenland-Scotland region. An understanding of overflows and the related processes - as well as a correct representation of them in climate models - is a necessity if one seeks to understand and predict our climate (Saunders 2001).

In the northern hemisphere, there are two major passages where dense water formed in the Arctic or in the Nordic seas (Hansen & Østerhus 2000) are able to cross the Greenland-Scotland ridge and flow south; the Faroe Bank channel (e.g. Mauritzen et al. (2005), Borenäs & Lundberg (1988)) and the Denmark Strait (e.g. Girton & Sanford (2003)), both of which are important overflow sites. Dense plumes are also found e.g. outside the Gibraltar Strait, where warm and saline water exits the Mediterranean Sea and in Storfjorden, Svalbard (e.g. Quadfasel et al. (1988)). In the southern hemisphere, the Filchner Overflow (Foldvik et al. 2004) is the most important overflow site, but dense cascades have also been observed in the Ross Sea (Gordon et al. 2004) and elsewhere around Antarctica (Baines & Condie 1998). Smaller plumes can be observed, probably intermittently, as dense water formed on continental shelves cascades down the continental slopes (Ivanov et al. 2004). A summary of the characteristics of the largest overflows is given by Gordon et al. (2007).

[1] Part of the oceanic heat transport is also carried by the horizontal circulation (Spall 2004, Mauritzen 1996).

2.2 Antarctic Bottom Water

Water of Antarctic origin occupies a major part of the deep ocean. The North and South Pacific, the Indian Ocean and the Atlantic Ocean are all partly filled with Antarctic Bottom Water (AABW, Fig. 1) (Orsi & Whitworth 2004). AABW is fresher but colder and denser than the water formed in the high, northern latitudes. The export of ventilated deep water from the Southern Ocean has been estimated to be 15 Sv (1 Sv = 10^6 m^3/s) (Broecker et al. 1998).

The Weddell Sea is traditionally thought to be the largest source of bottom water in the southern hemisphere (Orsi et al. 1999, Foldvik & Gammelsrød 1988, Deacon 1937), although rates and formation areas are a matter of debate (Schlitzer 2007, Jacobs 2004, Fahrbach et al. 2001, Broecker et al. 1998). The distribution of bottom temperature (Fig. 2) and oxygen content around Antarctica show, however, that the coldest and most oxygen rich water has its source in the Weddell Sea region (Orsi & Whitworth 2004). In the Weddell Sea, dense bottom water is formed through shelf processes and frontal zone mixing (Foster & Carmack 1976*b*), open ocean convection (Gordon 1978) and, as in the case of the Filchner Overflow, through interaction with the floating ice shelves.

The Filchner Overflow was detected in 1977, when hydrographic sections from the continental slope in the southwestern Weddell Sea revealed a plume of dense, supercooled water emerging from the Filchner Depression (Foldvik et al. 1985*b,c*). The plume consists of Ice Shelf Water (ISW) originating from the Filchner-Ronne Ice Shelf cavity, where it has been in cooled from contact with glacial ice at great depth. On the continental slope, the ISW mixes with the ambient water to form Weddell Sea Bottom Water (WSBW) and eventually Antarctic Bottom Water (AABW) that escapes the Weddell basin though gaps in the South Scotia Ridge (e.g. Carmack & Foster (1975)).

2.3 Plume Dynamics

Dense water entering an ocean basin through a gap or a strait will flow out along the continental slope as a dense plume. The following sections briefly explain basic plume dynamics and important processes and terms.

2.3.1 Geostrophic Balance

On oceanic scales, as in the case of a dense plume on a continental slope, the Coriolis force[2] will influence all motion. The Coriolis force is proportional to the speed and it is directed to the right (left) of the direction of motion in the northern (southern) hemisphere (from now on only the northern hemisphere is considered.) Dense water moving down a slope under the

[2]The Coriolis force is caused by the earth's rotation

a)

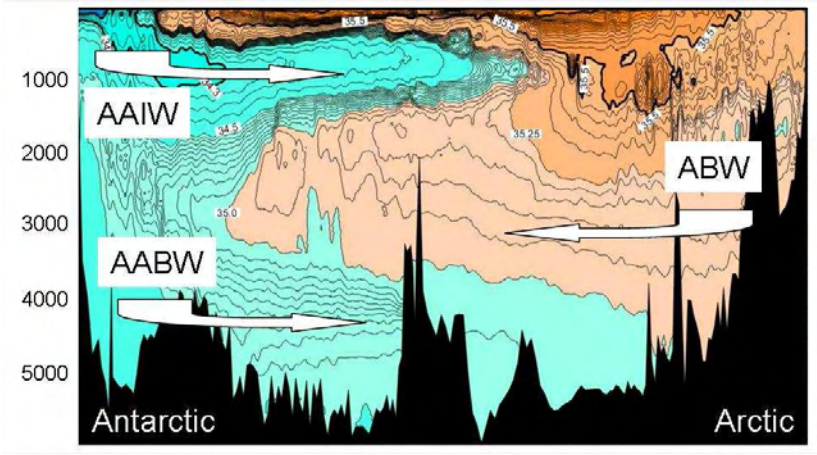

b)

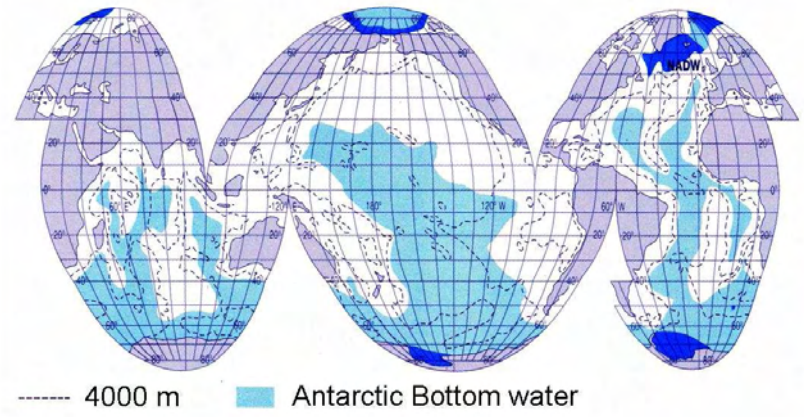

Figure 1: *a) Salinity transect across the Atlantic with the Antarctic (south) to the left and the Arctic (north) to the right showing Antarctic Bottom Water (AABW), Antarctic Intermediate Water (AAIW) and Arctic Bottom Water (ABW). b) Extent of Antarctic Bottom Water (AABW) in the world's oceans. Data from WOCE Hydrographic Atlas (Orsi & Whitwort, 2004).*

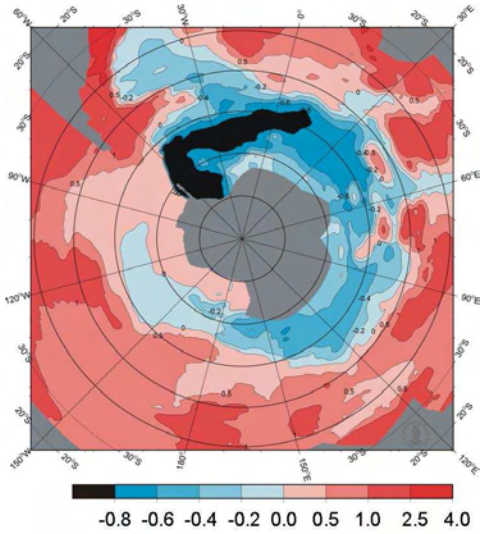

Figure 2: *Bottom temperature around Antarctica. Data from WOCE Hydrographic Atlas (Orsi & Whitwort, 2004).*

action of gravity will hence experience a force to the right, and tends to turn in that direction.

A flow is said to be in geostrophic balance if gravity, or more correctly the pressure gradient force, is balanced by the Coriolis force, i.e. when these forces are equally large and oppositely directed. The motion in a geostrophically balanced dense layer is perpendicular (to the right) to the local pressure gradient. Consider first a dense layer with constant thickness flowing on a constant slope. The pressure gradient is directed down the slope, and the geostrophically balanced flow will be directed *along the isobaths* with the shallow water to its right (Fig. 3.1). On the other hand a dome of dense water on a constant slope will move anticyclonically around its center. In addition to the rotational motion, the dome will translate along the slope with the Nof speed (Fig. 3.2-3) (Nof 1983)

$$U_{Nof} = \frac{g' tan\alpha}{f} \tag{1}$$

where g' [3] is the reduced gravity, α the bottom slope (see Fig. 3.3) and f the Coriolis force. The mean speed of any arbitrary shaped dense layer on a constantly sloping bottom (e.g. the layer with constant thickness considered above) is equal to the Nof speed.

Many large-scale flows are in geostrophic or close to geostrophic balance and the geostrophic approximation is often applicable.

[3] $g' = g\frac{\rho_2 - \rho_1}{\rho_2}$, ρ_1 and ρ_2 is the density of the upper and lower layer respectively

2.3.2 Ekman Drainage and Friction

The bottom boundary layer of a plume will always experience friction, even though the interior may be in near geostrophic balance. Under the influence of friction the velocity vectors decrease in magnitude and veer to the left when approaching the bottom from above (analogously to a wind induced current at the surface, Ekman (1905)). The velocity vectors trace out a vertical spiral, often referred to as the Ekman spiral (Fig. 4.1). The net motion within the bottom Ekman layer is referred to as the Ekman transport, and it is directed 90° to the left of the interior flow (Fig. 4.2).

During experiments with dense flows on sloping bottoms (e.g. Lane-Serff & Baines (1998)), a thin layer of downward moving dense fluid was observed on the downslope side of the main flow, which flowed geostrophically along the isobaths. Theory (Wåhlin & Walin 2001) suggests that the thickness of this "tongue" should be roughly equal to the Ekman layer thickness, $\delta = \sqrt{\nu/2f}$, where ν is the kinematic viscosity of water and f the Coriolis force, and that the speed of the dense tongue should be comparable to the Nof speed (eq. 1). Dense fluid is thus constantly drained from the downslope side of the plume, causing it to widen and flatten out (Fig. 4.3).

There are different approaches on how to include and parameterize the effect of friction. In streamtube models (e.g. Smith (1975) and Price & Baringer (1994), Section 2.4.1), which describe the bulk properties of the plume, and in the work by Killworth (2001), the plume properties are horizontally and vertically averaged and the plume is treated as a solid body.

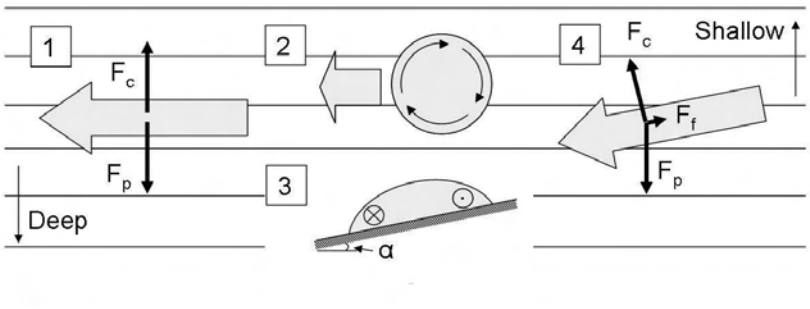

Figure 3: *Flow and force balance for dense plumes on a constant slope in the northern hemisphere (viewed from above with isobaths inserted). Flow is shown with gray and thin black arrows and forces with bold, annotated black arrows. (1) Geostrophic balance in a layer of constant thickness ($F_{Coriolis} = F_{Pressure}$). (2) Motion in (black arrows) and of (gray arrow) a dome of dense water. (3) Side view of a dome of dense water. ⊗/⊙ indicates interior flow into/out of the paper. (4) Force balance with friction in a layer of constant thickness. ($F_{Friction} + F_{Coriolis} = F_{Pressure}$)*

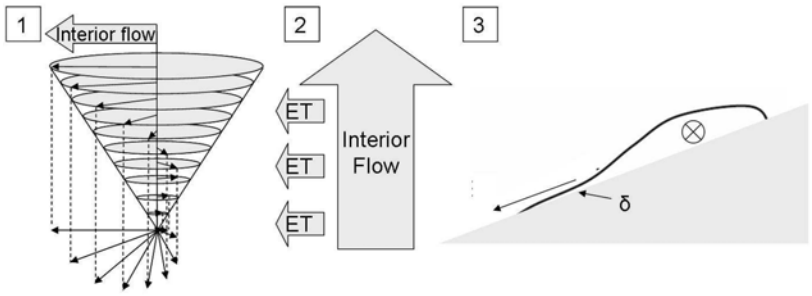

Figure 4: *(1) Velocity vectors at different levels above the bottom forming an Ekman spiral as the vectors veer to the left and decrease in size towards the bottom. (2) The net flow in the Ekman layer (ET) - the Ekman transport - is to the left of the interior flow (Northern Hemisphere). (3) Downslope Ekman drainage in the lower part of a plume that is flowing geostrophically along the isobaths. ⊗ indicates flow into the paper.*

Friction then appears as a body force which causes the entire plume to deflect downslope (Fig. 3.4). Killworth (2001) hypothesized that the plume-path is independent of parameters such as bottom drag and entrainment/detrainment, and that the descent rate ought to be roughly 1:400 (if the plume is in turbulent equilibrium, i.e. if the local production of turbulent kinetic energy everywhere equals the dissipation), i.e. the plume water descends 1 m vertically while advancing 400 m horizontally.

2.3.3 Generation of Eddies and Waves

Observations of dense plumes in the ocean, laboratory and numerical models show features that are not accounted for by the geostrophic and frictional balance described above. Instabilities and interactions with the overlying layer may cause eddies and roll-waves to develop, altering the shape, velocity patterns and characteristics of the plume.

Eddies Eddies are often observed in connection with dense overflows, in the ocean (e.g. Käse et al. (2003) and Bruce (1995)), in laboratory experiments (e.g. Cenedese et al. (2004), Etling et al. (2000), Lane-Serff & Baines (1998, 2000), Smith (1977)) and in numerical models (e.g. Ezer (2006), Krauss & Käse (1998), Gawarkiewicz & Chapman (1995), Jiang & Gaarwood (1995)). The eddies can generally be divided into two categories: Potential Vorticity eddies (PV-eddies), which are generated as the overlying layer is "captured" by the lower layer, brought to greater depth and hence stretched and forced to rotate in order to conserve its potential vorticity (Lane-Serff & Baines 1998, Spall & Price 1998) and Baro-

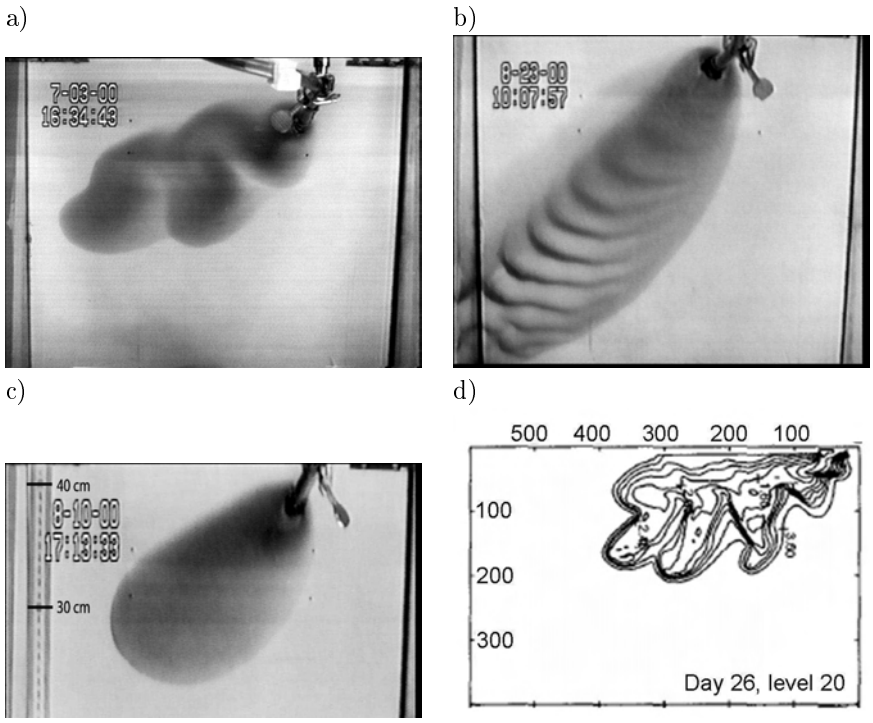

Figure 5: *Top views of laboratory experiments from Cenedese et al. (2004). a) Eddy regime (low Ek); b) wave regime (Fr > 1); c) laminar regime (Fr < 1, high Ek); and d) results from a numerical model showing development of subplumes, from Jiang and Garwood (1996).*

clinic Instability eddies (BI-eddies) generated from baroclinic instabilities (Swaters 1991).

PV-eddies tends to form close to the source, while BI-eddies form after the along-slope flow has been established (Lane-Serff 2001). Due to the different generation mechanisms, the eddies have different characteristics. PV-eddies are associated with a depression of the surface causing a strong cyclonic (and barotropic) motion in the whole water column. The dense water is concentrated in domes under the eddy, and there is a baroclinic, anticyclonic component in the lower layer, counteracting the barotropic forcing (Lane-Serff & Baines 1998). PV-eddies are therefore strongest in the upper layer. The eddies in Fig. 5a (Cenedese et al. 2004) and those observed by Lane-Serff & Baines (1998) are typical examples of PV-eddies. It is possible that anticyclonic PV-eddies may be generated if the "captured" upper layer is brought upslope (Krauss & Käse 1998). The eddies observed in the Denmark Strait outflow (Käse et al. 2003, Krauss & Käse 1998, Krauss 1996, Bruce 1995) are thought to be PV-eddies (Käse et al. 2003, Krauss & Käse 1998, Spall & Price 1998),

although there is evidence indicating that BI-eddies might also be generated (Jungclaus et al. 2001, Smith 1976).

BI-eddies are generated at the plume edges, with (weaker) anticyclonic eddies forming on the shallow side and (stronger) cyclonic eddies on the deeper side (Swaters 1991). Contrary to the PV-eddies, they are strongest in the bottom layer and there is a vertical phase-lag, i.e. a time-lag between motion at two levels. BI-eddies can be accompanied by sub-plumes, as in the laboratory experiments by Etling et al. (2000) and in the numerical model by Jiang & Garwood (1996) (Fig. 5d).

Whether PV- or BI-eddies form depends partly on the ratio between the thickness of the plume and the vertical scale of the motion which Swaters (1991) termed the interaction parameter, μ[4]. Eddies are generated through vortex stretching if μ is small, while large values of μ give baroclinic eddies (Etling et al. 2000).

Eddies increase downslope transport (Tanaka 2006, Tanaka & Akitomo 2001) and enhance mixing (Jungclaus et al. 2001, Jiang & Garwood 1996), since they induce both horizontal stirring and vertical motion (Krauss & Käse 1998).

Roll-waves The wave-like structures that appear on the pavement as rainwater flows downhill on a gray day in Bergen are a kind of roll-wave. Roll-waves are generated when a supercritical flow is destabilized by friction (Swaters 2003). The waves form periodic, large-amplitude wave fronts (Balmforth & Mandre 2004) that travel faster than the mean flow (Fer et al. 2001). Roll-waves are commonly observed in laboratory experiments with dense plumes (Fig. 5b) (e.g. Cenedese et al. (2004), Etling et al. (2000)), but there are no clear reports on observations of oceanic roll-waves, although Fer et al. (2002) observed roll-waves during winter cascading of cold water plumes in a lake. Theory suggests that roll-waves may be generated downslope of the sill/overflow and that the waves would have a frequency higher than the Coriolis frequency f (Swaters 2003). Breaking roll-waves have been shown to substantially increase mixing (more than eddies) (Adduce & Cendese 2007, Cenedese et al. 2004) and the fast moving wave fronts can be expected to enhance downslope transport (Fer et al. 2001).

The two flow regimes described above and a third, laminar regime (Fig. 5c) corresponding to the geostrophic/frictional flow described earlier were observed by Cenedese et al. (2004) in rotating laboratory experiments with dense plumes. The characteristics of the flow were determined by the (internal) Froude number, Fr, which compares the speed of the current with that of a (interfacial) gravity wave and by the Ekman number, Ek, which compares the frictional (viscous) forces with the Coriolis force. The Fr and Ek numbers are defined

[4] $\mu = h/\alpha Ro$, where h is the thickness of the dense layer, α is the slope and Ro the Rossby radius based on the total water depth, D, i.e. $Ro = g'D/f$.

as

$$Fr = U/\sqrt{g'hcos\theta} \tag{2}$$

$$Ek = (\delta/h)^2 \tag{3}$$

where U is the speed, g' the reduced gravity, h the thickness of the dense layer, θ the slope and δ the thickness of the Ekman layer. A combination of low Froude and high Ekman numbers generally gave laminar flow (Fig. 5c). For low Ekman numbers the plume tended to break up into periodic domes as PV-eddies were generated (Fig. 5a). This is in accordance with laboratory experiments by Lane-Serff & Baines (1998), who observed eddies in cases where the viscous drainage was not dominant, i.e. for small Ekman numbers. The generation of PV-eddies are however dependent on the depth of the overlying layer, in that a thick upper layer experiences a smaller relative stretching, which slows down or possibly inhibits eddy generation (Lane-Serff & Baines 1998). Stratification reduces the effective depth of the upper layer, enhancing stretching and eddy formation (Lane-Serff & Baines 2000). As mentioned earlier, roll-waves are observed in supercritical flows, i.e. flows with $Fr > 1$ (Cenedese et al. 2004, Fer et al. 2002).

2.3.4 Entrainment

As a dense plume flows down a slope it entrains and mixes with lighter ambient water. The plume gradually loses its density surplus, and g' is reduced. Entrainment represents a frictional force, since the entrained water has no momentum (or that of the ambient fluid if it is moving). There are different mechanisms causing entrainment, e.g. Kelvin Helmholtz instabilities (Özgökmen & Chassignet 2002), roll-waves (Adduce & Cendese 2007, Cenedese et al. 2004), eddies, shear induced turbulence and hydraulic jumps.

The entrainment rate, E, quantifies the amount of water entrained per meter traveled along the slope (Ellison & Turner 1959). E has been observed to increase with increasing Froude number, Fr (eq. 2) both in laboratory experiments (Adduce & Cendese 2007, Wells & Wettlaufer 2005, Cenedese et al. 2004, Ellison & Turner 1959) and in the ocean (Price & Baringer 1994), although Arneborg et al. (2007) observed a large increase in entrainment while the Froude number was decreasing. A Froude-number dependent parameterization of E based on non-rotating laboratory experiments (Turner 1986, Ellison & Turner 1959) is widely used. This parameterization does not allow for sub-critical mixing since it has a cut-off at $Fr^2 = 1.25$. Sub-critical mixing is observed however (Adduce & Cendese 2007, Cenedese et al. 2004), and even if it is small it may be important if it occurs over a long distance (Hughes & Griffiths 2006, Wåhlin & Cenedese 2006). A new parameterization, allowing for sub-critical mixing, was proposed by Adduce & Cendese (2007).

In a stratified environment the plume will eventually reach its density level and leave the slope. Water from the outer, more diluted part of the plume may "shave off" and leave the plume (i.e. detrain or interleave) when this water reaches its density level (Baines 2001,

2005).

2.3.5 Thermobaricity

The compressibility of sea-water, i.e. the dependency of its density on pressure, $\frac{\partial \rho}{\partial p}$, increases with decreasing temperature. Hence, two water masses, one cold and fresh and the other warm and saline, having the same density at the surface will not be equally compressed and thus no longer equally dense if moved vertically to a greater depth. The cold parcel will experience a greater compression and be denser.

2.3.6 Topographic Steering

The term topographic steering is generally used in relation to large-scale barotropic flows. In order to conserve their potential vorticity these currents are forced to follow contours of constant f/D, where D is the water depth. In this work the term is used to describe the steering of dense water downslope by small-scale topography.

2.4 Dense Plumes in Numerical Models

Dense plumes can be represented numerically in a number of ways; the choice depending on the aim of the study. The following sections first describe different models of dense plumes and then the treatment of plumes in large-scale ocean and climate models.

2.4.1 From Streamtubes to 3-D Non-Hydrostatic Models

The "streamtube model" was first proposed by Smith (1975) and describes the steady state bulk behavior of a dense plume. The flow is assumed to be confined to a streamtube and at each position along the path the plume properties are given as vertically and horizontally averaged values. The streamtube model has been further developed to include e.g. thermobaric effects, more elaborate entrainment parameterizations, realistic bottom topography, background stratification and plume widening (Alendal et al. 1994, Price & Baringer 1994, Killworth 1977). Due to the model formulation, Ekman drainage and detrainment are neglected, as is any form of instability or interaction with the upper layer. This type of model is not able to capture the time-dependent phenomena described in the preceding sections. Streamtube models may nevertheless be appropriate to estimate mixing, pathway and end-products of strong, turbulent overflows in which properties are well-mixed and bottom friction is distributed throughout the plume (Lane-Serff 2001).

Jungclaus & Backhaus (1994) presented a more general, 2-dimensional plume model. The plume is allowed to vary laterally, while the equations are vertically integrated. (A

problem with vertically integrated models will be discussed in Appendix B.) Using this model, Jungclaus et al. (1995) observed the plume to divide when encountering topographic features such as ridges on the slope. Three-dimensional, finite difference numerical models have allowed for more realistic plume modeling, where the dense layer can interact with the upper layer and where eddies and instabilities may develop (e.g. Riemenschneider & Legg (2007), Ezer (2006), Tanaka & Akitomo (2001), Spall & Price (1998) and Jiang & Garwood (1995, 1996, 1998)).

The latest generation of plume models are non-hydrostatic, i.e. vertical acceleration is included, and this improvement (along with better resolution) allows for Kelvin Helmholz instabilities to develop on the plume interface (Özgökmen & Chassignet 2002) and for a better representation of the plume head (Heggelund et al. 2004), for example. In addition, a new type of model, the finite element model is under development (e.g. Ford et al. (2004)). This model employs an unstructured mesh that automatically adapts to optimize the resolution so that it is high where it needs to be high, i.e. where fine-scale features are developing, and low elsewhere.

2.4.2 Representation of Overflows in Ocean and Global Climate Models

A good representation of overflows in Global Climate Models (GCM) is important in order for them to produce realistic scenarios. Nevertheless, dense overflows continue to be a weak point in large-scale models (Griffies et al. 2000). One problem is the coarse resolution, which for a GCM is typically in the order of $2^\circ \times 2^\circ$ or 100×100 km. The overflows, and processes occurring within them, thus represent subgridscale processes that need to be parameterized. In addition, the horizontal resolution is typically larger than the channels or deep connections through which the overflows emerge. These passages might need to be unrealistically widened and deepened to assure connection between ocean basins. The use of partially open faces or grid-boxes may allow coarse resolution models to capture the geometric effects of straits, i.e. that the right flux passes through the right area with the right speed (Hallberg, pers. comm.).

The representation of overflows in numerical models is strongly dependent on the choice of vertical coordinates (Legg et al. 2006, Griffies et al. 2000). The alternative vertical coordinates are shown in Fig. 6a. In *z-coordinate models* (geopotential), a sloping bottom topography is represented as a series of steps, or a staircase (Fig. 6b), although some models operate with so called "shaved cells", in which the bottom-cell is a piece-wise linear fit to topography (Adcroft et al. 1997). Leaving one step, the descending dense water causes static instability and convective homogenization (Winton et al. 1998). Hence, the dense water is involved in strong vertical mixing and rapidly looses its density surplus rather than descending the slope. In *terrain-following models*, overflow processes can be well resolved, since it is possible to concentrate the resolution near the bottom boundary. Problems arise when calculating pressure gradients above steep topography (Haidvogel & Beckmann 1999). As in z-coordinate models, mixing in terrain-following models is often excessive, partly

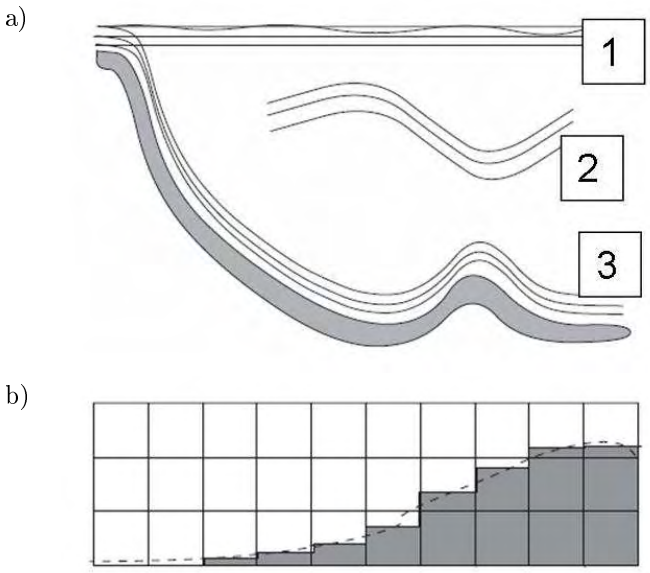

Figure 6: *a) Vertical coordinates in (1) z-coordinate, (2) isopycnal and (3) terrain following models. b) Staircase representation of topography in a z-coordinate model (using partial cells) from Griffies et al. (2000).*

due to overly large horizontal turbulent diffusion. The *isopycnal models* uses density as its vertical coordinate and gravity plumes are naturally represented. There are no steps creating artificial mixing as in z-coordinate models, and no pressure gradient problem as in the terrain-following models. Isopycnal models are generally good at preserving water mass properties (Griffies et al. 2000). The diapycnal mixing, i.e. entrainment, has to be parameterized (e.g. Hallberg (2000)) or else the plume water retains its initial properties while descending the slope.

To correctly model plumes and plume entrainment one needs to (a) limit the artificial, numerical mixing (in terrain-following and z-coordinate models) and (b) parameterize the real, small-scale process-dependent entrainment. Many methods have been suggested, e.g. "plumbing" where grid cells above and below a topographic step are connected (e.g. Campin & Goosse (1999)) or the addition of separate bottom boundary layer models (e.g. Killworth & Edwards (1999)). Price & Yang (1998) avoid the problem by modeling only the effect of the plume, and not the plume itself. The dense water is removed from its source and injected as a mixed water mass further downstream. This is referred to as the Marginal Sea Boundary Condition.

2.5 The Filchner Overflow

This study, to some extent, focuses on the Filchner Overflow, which is located in the southwestern Weddell Sea, Antarctica. The following sections will give a brief introduction to the geographic and oceanographic setting, and explain how the dense Ice Shelf Water forming the plume is generated.

2.5.1 Geography and Oceanography of the Weddell Sea

The Weddell Sea is the southernmost extension of the South Atlantic, extending eastward from the Atlantic Peninsula to Kapp Norvegia and the South Sandwich Islands. Fig. 7 shows the southwestern Weddell Sea where the large Filchner-Ronne Ice Shelf (FRIS) is located. The ice shelf has an area of 450,000 km^2 and is the largest (by ice volume) of the Antarctic ice shelves. The average ice thickness is 350 m, but the ice can be as thick as 2000 m at the grounding line[5] (Hellmer 2006). The continental shelf in front of FRIS is about 500 km wide (north-south) and 300-500 m deep. It is crosscut by two relatively deep troughs, the Ronne Depression in the west and the Filchner Depression in the east. The continental shelves to the east and north are much narrower (0-100 km). The Weddell Abyssal Plain is the deepest portion of the Weddell Sea, with depths reaching over 5000 m. The deep Weddell Sea is connected to the Scotia Sea and the global oceans by gaps in the South Scotia Ridge, which are as deep as 3000-3500 m.

The oceanography of the Weddell Sea is dominated by the cyclonic Weddell Gyre. The southern limb of the gyre is difficult to distinguish from the Antarctic Coastal Current which is found above the continental shelf break (Sverdrup 1953) and has mean velocities of around 10-20 cm/s (Fahrbach et al. 1992). The coastal current divides in two just east of the Filchner Depression (at 27° West), with one core following the coast and the other flowing along the shelf break (Gill 1973). The currents are sketched in Fig. 7. Both semi-diurnal and diurnal tides travel westward around Antarctica as Kelvin waves (Robertson 1998, 2005). The semi-diurnal tide excites continental shelf waves in the continental slope region, causing anomalously large diurnal currents at the shelf break (Middleton et al. 1987).

The sea-ice cover in the Weddell Sea is predominantly seasonal, and like the rest of Antarctica the ice cover is dominated by first-year ice. Katabatic winds[6] and tidal actions (Padman & Kottmeier 2000) help to maintain and open up coastal polynyas, where ice-production and atmosphere-ocean heat exchange are large. The intensive sea-ice growth (up to 0.1 m/day) results in brine rejection and the formation of dense saline shelf water. The general east-west circulation on the shelf makes the western shelf water more saline than the water found on the eastern shelf.

[5] The grounding line is the point where the ice-sheet leaves the bed rock and becomes a floating ice shelf
[6] Cold fall winds from the ice-sheet

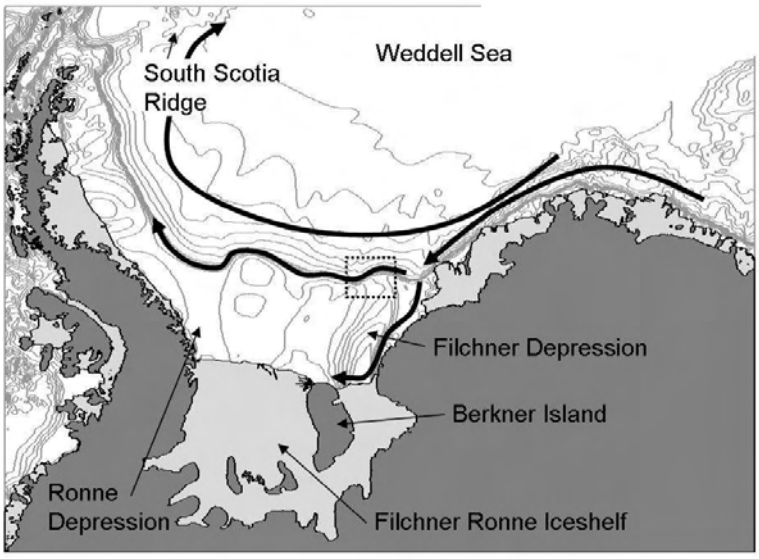

Figure 7: *Bathymetry of the southwestern Weddell Sea. The thick arrows indicate the Antarctic Coastal Current, the Antarctic Slope Current and the Weddell Gyre.*

The water masses found in the Weddell Sea are listed in Table 1. Eastern Shelf Water (ESW) is less saline than the Western Shelf Water (WSW) which is often referred to as High Salinity Shelf Water (HSSW). HSSW enters the ice shelf cavity, interacts with the glacial ice as described in the following section and exits the cavity as Ice Shelf Water (ISW). The Antarctic Circumpolar Current (ACC) consists to a large extent of Circumpolar Deep Water (CDW), flowing at depth around the continent and entering the Weddell Sea where it is modified by shelf water and surface Winter Water (WW) to form Weddell Deep Water (WDW) and Modified Warm Deep Water (MWDW). The deep Weddell Sea is filled with Weddell Sea Bottom Water (WSBW), formed as dense ISW and HSSW descends the continental slope while mixing and entraining WDW. Deep water is also formed through open ocean convection (Gordon 1978). Modified WSBW escapes the Weddell Sea as Antarctic Bottom Water (AABW).

2.5.2 Generation of Ice Shelf Water

Ice Shelf Water (ISW) is defined as water with a temperature lower than its surface freezing point and it is formed as sea water interacts with glacial ice at great depths.
The ISW formation process is described in e.g. Nøst & Foldvik (1994) and it is depicted in Fig. 8. HSSW formed on the continental shelves during winter enters the ice shelf cavity and sinks to the grounding line, which can be located as deep as 1800 m below the sea level. At this depth the freezing point, T_f, is lower than at the surface since the freez-

Water Mass		Definition	Explanation
Antarctic Bottom Water	AABW	-0.7< θ <0.0°C 34.64<S<34.68	Bottom water formed in Antarctica
Circumpolar Deep Water	CDW	θ >-0.5°C	Deep water found all around Antarctica
Eastern Shelf Water	ESW	θ ∼-0.5°C 34.28<S<34.44	Shelf water in the eastern Weddell Sea
Ice Shelf Water	ISW	θ <-1.9°C	Formed under the floating ice-shelves
Modified Warm Deep Water	MWDW	θ ∼-1.2°C S∼34.5	Mixture of WDW and WW
Warm Deep Water	WDW	0< θ <0.8°C 34.64<S<34.72	CDW modified by shelf water
Weddell Sea Bottom Water	WSBW	θ <0.7°C S∼34.65	Bottom water formed in the Weddell Sea
Western Shelf Water/ High Salinity Shelf Water	WSW HSSW	θ ∼-1.9°C S>34.70	Shelf water in the western Weddell Sea
Winter Water	WW	θ ∼-1.9°C 34.28<S<34.52	Cooled surface water

Table 1: *Definitions of water masses in the Weddell Sea. Compiled by T. Gammelsrød from Foldvik et al. (1985*a*) and Foster & Carmack (1976*a*)*

ing point decreases with increasing pressure. The HSSW, which is at its surface freezing point ($T_{f,surface} = -1.9°\mathrm{C}$), is therefore warmer than the *in situ* freezing point (e.g. $T_{f,1000m} = -2.7°\mathrm{C}$), and heat is available to melt glacial ice. The water mass is cooled down to the local freezing point as the glacial ice is melted. Meanwhile, it mixes with the fresh melt-water and its salinity decreases sufficiently for the water to become buoyant and start rising along the ice surface. The pressure then decreases, and so the local freezing point increases and the rising water will eventually become supercooled. Ice crystals or frazil ice form within the rising water, and aggregate as thick layers of green marine ice (Warren et al. 1993) under the glacial ice. The temperature and the salinity of the water then rises again. When the water leaves the ice shelf cavity as ISW, it is colder and slightly fresher than the water entering the cavity. During the formation of ISW there is a net flux of mass from the grounding line, where glacial ice is melted, to the thinner part of the ice shelf, where marine ice is deposited. This process is often referred to as the "ice pump" (Foldvik & Kvinge 1974).

The "ice pump" and the associated ISW and marine ice formation (Grosfeld & Hellmer 1998) is known to occur under the Filchner Ronne Ice Shelf. HSSW enters the cavity through the Ronne depression (Nicholls et al. 2003) and west of Berkner Island (Nicholls et al. 2001).

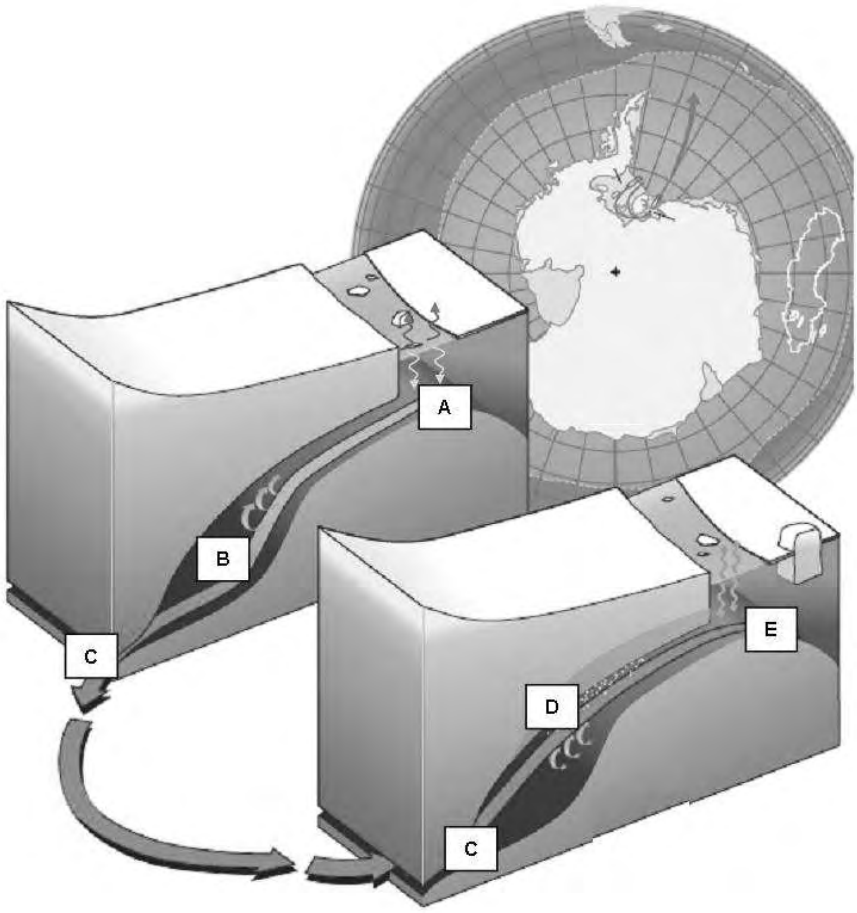

Figure 8: *ISW formation: (a) Ice production and brine rejection during winter form HSSW on the continental shelf; (b) HSSW at surface freezing point (T=-1.9° C) fills the ice shelf cavity; (c) Rapid melting at the grounding line where the freezing point is lower than at the surface; (d) Layers of marine ice forms under the glacial ice as the rising water gets supercooled; (e) ISW exits the ice shelf cavity. (Courtesy to B. Samuelsson, Svenska Dagbladet)*

After transformation it exits as ISW through the Filchner Depression, and spills over the sill to form the Filchner Overflow plume (Foldvik et al. 2004). The flux of ISW through the Filchner Depression has been estimated to be 1.6±0.5 Sv (Foldvik et al. 2004).

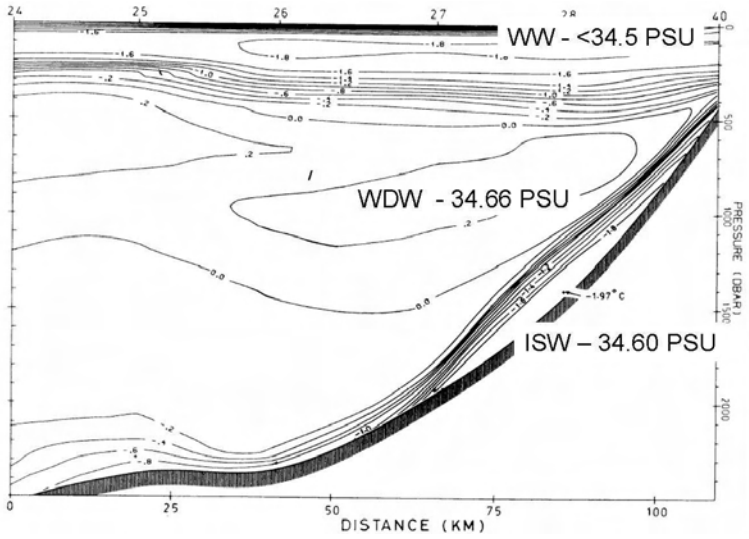

Figure 9: *CTD section from the continental shelf slope west of the Filchner Depression showing the dense plume of Ice Shelf Water (ISW), the overlying Weddell Deep Water (WDW) and the Winter Water (WW) at the surface. (Modified from Foldvik et al (1985*b*))*

2.5.3 The Filchner Overflow plume

ISW leaving the Filchner Depression forms a dense, cold plume that turns westward (left) on the continental shelf slope (Foldvik et al. 2004). Fig. 9 shows the cold plume water as an approximately 200 m thick and roughly 50 km wide layer, underlying the warmer WDW. During its descent the ISW mixes with WDW and forms WSBW. Foldvik et al. (2004) estimated that ISW from the Filchner Overflow contributes with 4.3±1.4 Sv to the WSBW formation.

Since the discovery of the plume in hydrographic sections 1977 (Foldvik et al., 1985*b*,*c*), a number of current meter moorings have been placed in the area (for a full list, see Foldvik et al. (2004)). The position of the moorings are marked in Fig. 10, which also shows the mean current from the bottom-most instruments. Based on CTD data (from Foster et al. (1987) and Foster & Carmack (1976*b*)) and mooring data, Foldvik et al. (2004) suggested three plume pathways: one following the shelf break and upper slope (FO1), one following the slope at greater depth (FO2) and the final one following the first prominent ridge (FO3). The suggested pathways are shown in Fig. 10, where the plume path derived from the constant decent rate of 1:400 proposed by Killworth (2001) is inserted. The results from Killworth's model do not match the observations well.

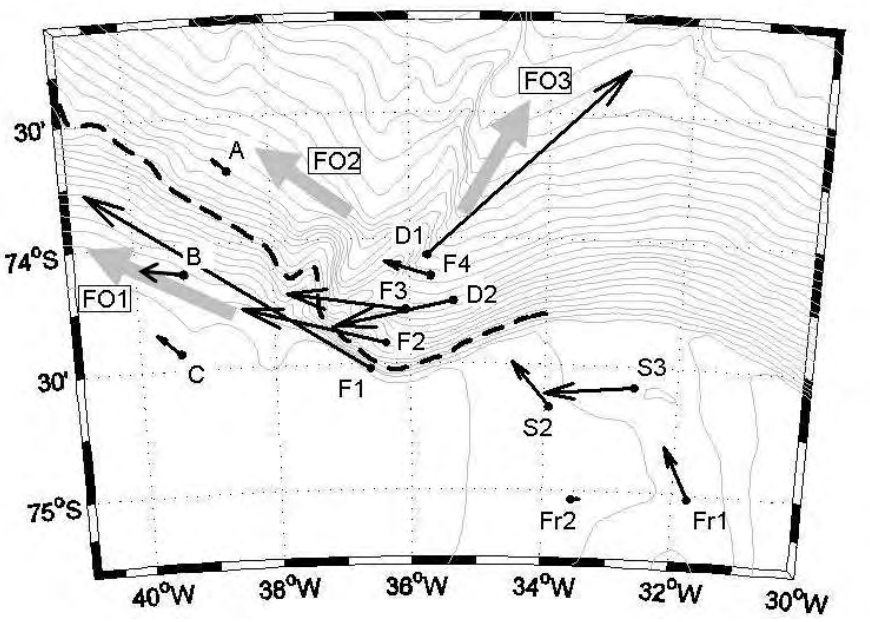

Figure 10: *Locations of moorings placed in the Filchner Overflow area and mean current at the instrument closest to the bottom (10-56 mab). For detailed information on instrumentation and deployment see Foldvik et al (2004). The dashed line shows the calculated plume path based on the 1:400 descent rate proposed by Killworth (2001) and the gray arrows indicate the three paths suggested by Foldvik et al. (2004)*

3 This study

3.1 Objectives and Methods

The aim of this study was to investigate dynamical processes of importance to dense overflow plumes, focussing on the Filchner Overflow, Antarctica. As described in previous sections, overflow plumes and processes occurring within them are important factors in the global oceanic circulation and thus in our climate. Yet, the physics determining their pathways, characteristics and mixing are, to a large degree, unknown.

This work attempts to elucidate the following questions:

a) What is the effect on the Filchner Overflow plume of the two ridges crosscutting the shelf? Can such ridges, like canyons, steer dense water down the continental slope, and, if so, to what extent? What are the governing parameters and dynamics?

b) What mesoscale variability is observed within the Filchner Plume, and what is causing it? How are the observed phenomena generated?

c) What is the effect of the ridges and the phenomena causing the variability on plume mixing and entrainment?

In short, there are three foci: topographic steering, variability and mixing.

All current meter data from the Filchner region have been analyzed using ordinary and rotary Fourier analysis and wavelet analysis to describe mesoscale variability. The data have been collected using bottom moorings, deployed mainly by researchers from University of Bergen (UiB), Alfred Wegner Institute (AWI) and British Antarctic Survey (BAS) and used, almost exclusively, RCM current meters from Aanderaa. CTD data collected during the cruises have also been studied.

The data-analysis motivated a theoretical study of the potential for submarine ridges, such as those found in the Filchner region, to steer dense water downslope. A two-dimensional 1.5-layer analytical plume model, previously applied to canyons (Wåhlin 2002), was employed to explore and quantify the possibility of such ridges to channel dense water downslope. Despite the simplifications involved the model proved useful, providing an explanation for the observations and a first order estimate of the downslope fluxes. The model results were compared with the data and showed reasonable agreement. The data set is, however, sparse, and the agreement should be considered a support for the theory, rather than a proof. The validity of the analytical model was tested more thoroughly in the Geophysical Fluid Dynamic Laboratory at University of Washington, Seattle, during February-June 2006. Under the supervision of Prof. P. Rhines and with technical assistance from E. Lindahl, a set of laboratory experiments was performed, in which the behavior of dense plumes "leaning" on topography was studied. Vertical transects of flow in the vicinity of a V-shaped sloping ridge and in a canyon for a set of parameters were obtained using fluorescent dye and a vertical light sheet. The results were compared with output from the analytical model. The flow pattern was visualized using dye, and vertical velocity profiles were collected using a Laser Doppler Velocimeter.

Another set of experiments was performed at the rotating Coriolis platform, Laboratoire Des Ecoulements Geophysiques et Industriels (LEGI) in Grenoble, France, to explore the effects of topography and flow regime on mixing. The focus was on the total mixing and not the local entrainment rate, since a high entrainment rate, which one would expect in the vicinity of a ridge, can be balanced by a high descent rate (i.e. a shorter plume path). We therefore studied the "end product" or the combined effect of entrainment rate and descent rate. Dense water from a continuous source at the top of a sloping bottom was allowed to descend into a collecting basin. The amount of mixing occurring during its descent - i.e. the

combined effect of entrainment rate and descent rate - was inferred from the stratification in the basin, which was monitored using profiling conductivity and temperature probes. The same experiment was performed with and without topography (ridge/canyon) and with parameter combinations giving eddies, waves and laminar flow. The experiments were part of the project *"Modelling Antarctic Flows"*, coordinated by G. Lane-Serff and realized in November-December 2006. The experiments were conducted by the project participants with technical assistance from S. Viboud, H. Didelle and J. Sommeria. The project also included experiments on eddy-ice shelf interaction by G. Lane-Serff and J. Buck and ice shelf cavity circulation by D. Holland, A. Jenkins and P. Holland.

This work is presented in Papers I-IV, which are summarized below.

The analytical model used in the study neglects advection and assumes geostrophy. To investigate the advection terms, a one-dimensional, one-layered vertically integrated model was employed (L. Umlauf, pers. comm.). However, vertical integration of the momentum equations requires a simplification of the advection terms. In short, the integration of a product is replaced with the product of the two terms integrated separately (Simons (1980), see Appendix B for details). When the volume flux is zero, which in our case it is in the across canyon/ridge direction, the advection terms in models of this type are also zero. Accordingly, the effect of advection is *not* included in the calculations.

The results from the numerical model are presented and compared with the analytical results in Appendix A, while the simplification of the advection terms is discussed further in Appendix B, where the validity of the approximation is tested for two special cases.

3.2 Summary of papers

3.2.1 Paper I.

Downward flow of dense water leaning on a submarine ridge

Data from current meter moorings in the Filchner region suggest that a portion of the Filchner Overflow plume is steered downslope by a submarine ridge crosscutting the continental slope (Foldvik et al. 2004). We used a simplified analytical model, previously applied to submarine canyons (Davies et al. 2006, Wåhlin 2002), to show that ridges, like canyons, can promote geostrophically balanced downslope flow. For the dense water to flow down the ridge, it is required that the Ekman transport induced by the downslope flow (directed away from the ridge) balances the geostrophic flow (directed towards the ridge) caused by the background slope. We find analytical expressions for the transport capacity, i.e. the maximum amount of dense water that a ridge of given dimensions can steer downslope and show that the non-dimensionalized transport capacity depends solely on the geometrical parameter $\gamma = sW/\delta$, where s is the background slope, W the width of the canyon and δ the thickness of the Ekman layer. For small values of γ, ridges are shown to be more

effective than canyons in steering water downslope. We compare the theoretical results with data from the Filchner Overflow and find them to agree qualitatively well. The transport capacity of the Filchner ridge is estimated to be 0.3 Sv, and the ridge could thus steer a substantial part of the total outflow, 1.6 SV (Foldvik et al. 2004), downslope.

Although neglecting important processes such as entrainment and mixing, the model gives a first order estimate of the transport capacity of ridges, showing that they, along with canyons, may be of importance to dense plumes and overflows.

3.2.2 Paper II.

Topographic steering of dense overflows: laboratory experiments with V-shaped ridges and canyons

This paper describes two sets of laboratory experiments that were performed in the Geophysical Fluid Dynamics Laboratory, University of Washington, Seattle, in order to test the theoretical model presented in **Paper I**. In the first set of experiments, I show that dense plumes on a sloping bottom can indeed be steered by submarine ridges and canyons cross-cutting the slope, and I proceeded with a second set of experiments to study flow in/along sloping canyons and ridges. I released dense water dyed with fluorescein in the upper part of a sloping V-shaped ridge/canyon and photographed transects of the flow using a vertical light sheet and a camera. I varied the parameters thought to govern the flow: the slope, s, the Coriolis parameter, f, the reduced gravity, g', and the flux, Q, and obtained information on how the variations affected interface shape and position. I show that there is good qualitative agreement between the theoretical solutions and the laboratory results, although the height of the interface is slightly underestimated.

By introducing dye into the bottom Ekman layer I visualized the transverse, secondary circulation proposed by the theoretical model. While moving down the canyon or along the ridge, a particle traces out a helix: moving towards the ridge in the interior and away from it in the bottom Ekman layer. The secondary circulation was further confirmed and quantified using a Laser Doppler Velocimeter. The vertical velocity profiles resolved the Ekman layer and showed the transverse flow superimposed on the primary, downslope flow.

During experiment performed at the rotating Coriolis platform a dense plume on a slope was observed to divide in two when the transport capacity of an intersecting ridge was exceeded; one part continued along the slope and the other flowed downslope along the ridge.

3.2.3 Paper III.

Mixing in density currents induced by submarine canyons and ridges

In this paper we describe a set of large-scale laboratory experiments performed as a part of the project *"Modelling Antarctic flows"* on the rotating Coriolis platform at LEGI (Laboratoire Des Ecoulements Geophysiques et Industriels) in Grenoble, France. The experiments aimed to quantify mixing for different flow regimes (Section 2.3.3) and different topographies. Dense water was injected to a 8×2.5 m large sloping bottom and a gravity plume formed. By changing the governing parameters (ambient water depth and density difference), we produced the three flow regimes described by Cenedese et al. (2004): laminar flow and roll-wave respective eddy generating flows. The sloping bottom had an exchangeable section, where a V-shaped ridge or canyon could be inserted. The three flow regimes were combined with the three topographies, to give 9 experiments. In three experiments, the dense water was allowed to descend a smooth, sloping bottom, and in six experiments the dense water was steered downslope by topography, hence filling up the closed basin with a mixture of dense source water and entrained, ambient water. We monitored the evolution of stratification in the basin using profiling conductivity sondes. The profiles allowed us to quantify the total amount of mixing occurring during the descent of the dense water.

On a smooth slope with no ridge or canyon present, mixing was largest under the wave regime, and smallest under the laminar regime. When a ridge or a canyon was present on the slope the dense flow was steered downslope as expected. The flow accelerated and waves developed, regardless of the flow characteristics on the smooth slope. The total mixing increased, and the increase in entrainment rate was hence more important than the shortened path. The difference between the regimes was smaller and the mixing larger overall when topography was present, indicating that it was the small-scale topography and not the large-scale characteristics of the flow that determined the properties of the end product.

The eddies were degenerated and the dense fluid "released" and steered downslope when they encountered topography.

3.2.4 Paper IV.

On the structure and variability of the Filchner Overflow plume

This paper aims to describe the Filchner Overflow plume, based on all available observations (CTD and current meter mooring data). While Foldvik et al. (2004) used the same data to quantify the transport, we focus on the surprisingly large short-term variability and try to produce a "mean" picture of the plume from the CTD data. Fourier analysis of current meter records revealed energetic oscillations with periods of about 35 hours, 3 days and 6 days, while wavelet analysis revealed an episodic nature of the phenomena. The oscillations are barotropic (depth-independent) and present in both velocity and temperature records. The velocity amplitudes are, in some cases, as high as 35 cm/s, while the temperature records indicate that the instruments are alternately submerged in cold plume water and ambient Weddell Deep Water. The energy levels west of the ridges and in the Filchner Depression are much lower. We discuss the observations with regard to existing theories

on eddies, which are known to be generated within dense plumes, and on continental shelf waves, which have been shown to enhance the tides in the area. None of the theories can satisfactorily explain the observations and we are unable to draw a conclusion regarding the origin of the oscillations.

In addition, we describe the general plume structure, water properties, and pathways. We apply the theory from **Paper I** to the second ridge in the region, and are thus able to estimate the transport along the three pathways suggested by Foldvik et al. (2004). The "mean" picture from the CTD data does not, however, support the suggested pathways.

4 Conclusions and outlook

4.1 Main results

Topographic Steering This study has shown - both theoretically and experimentally - that submarine ridges, like canyons, can effectively steer dense plume water downslope. An analytical model was proposed, predicting the dense layer shape and thickness and the transport capacity of a number of idealized ridge geometries. The analytical model was shown to agree with laboratory experiments, and with measurements in the vicinity of the eastern-most ridge in the Filchner area. The transport capacity of a ridge or canyon (i.e. the maximum amount of water that it can steer downslope) can be estimated as the product of $g'H^2/f$, where g' is the reduced gravity, f the Coriolis factor and H the height (depth) of the ridge (canyon), and a geometry dependent function $\hat{T}(\gamma)$, where $\gamma = sW/\delta$ and s is the slope, W the width of the ridge/canyon and δ the thickness of the Ekman layer. The transport capacity of the eastern ridge in the Filchner area was estimated to be 0.3 Sv and that of the western to be 0.6 Sv. A plume impinging on a ridge or a canyon is thought to split in two, with one part of the plume being steered downslope along the topography and the other continuing along the slope. This was observed in the laboratory. The analytical model can explain and quantify the suggested partition of the Filchner Overflow plume. Not all of the suggested pathways were supported by the "mean" picture of the plume, created from an assembly of all CTD stations in the area. Dense water was observed in a thick layer immediately behind the western ridge, indicating that it had been flowing over the ridge, rather than being steered downslope.

Eddies were observed to degenerate and release the underlying dome of dense water when encountering topography.

The secondary circulation associated with the topographically steered flow; a frictional flow in the bottom boundary layer and a return flow in the interior, was visualized and measured in the laboratory.

Variability The analysis of current meter records from the Filchner area revealed a surprisingly high variability at short timescales. Intermittent oscillations with periods of approximately 35 hours, 3 and 6 days were observed in the plume, both in velocity and temperature records. The observed oscillations were seemingly barotropic, showing neither attenuation nor phase shift in the vertical, despite a shear in the mean current. The generation of eddies in plumes has been reported before, e.g. from the Denmark Strait Overflow, but the theories suggested to explain this phenomena - vortex stretching and baroclinic instability - disagree with the Filchner observations. Continental shelf waves, which have been suggested to enhance the tidal motions in the area, cannot satisfactorily explain the observed variability. The generation mechanism and the more precise nature of the phenomena remain open questions, but the study has resulted in a detailed description and discussion of the observations.

Mixing It is known that entrainment depends strongly on the Froude number, Fr, and that high values of Fr give high entrainment rates. When dense fluid is steered downslope by topography it accelerates and the Froude number and consequently the entrainment rate can be expected to increase. Meanwhile, the plume path, or the distance over which mixing occurs, is shortened since the plume descends the slope at a greater angle. Our laboratory experiments have shown that the presence of small-scale topography steering the plume downslope increased the total mixing. The increase in the entrainment parameter is thus more important than the shortening of the plume path. Mixing was observed to be greater in plume experiments with eddies and roll-waves than in laminar experiments, but the effect of small-scale topography on mixing was shown to be greater than the large-scale characteristics of the flow.

Somewhat contradictory, almost undiluted ISW (T $\simeq$ -1.9°C) is occasionally flowing past mooring D1[7] with relatively high speed (up to 1 m/s).

4.2 Future work

The work presented in this thesis is a step towards a better understanding of plume dynamics and of the Filchner Overflow, but the number of questions it raises are probably greater than the answers given. What happens in the area where the plume impinges on topography? What dynamics make the flow turn downslope? What is generating the oscillations that were observed, and what are their effect on the plume water and its destiny? To what extent can the laboratory results be up-scaled to the ocean? Does the Filchner Overflow Plume split in three?

The dense water produced under the large ice shelves is a precursor to the Antarctic Bottom Water and of global importance. Unfortunately, the Filchner Overflow region is not

[7] D1 was placed at 2100 m depth in the vicinity of a ridge cross-cutting the path of the Filchner Overflow plume.

only interesting, but also remote and difficult to access. Conditions are harsh, with sea-ice, storms and icebergs making activity in the area expensive and risky. Yet, more fieldwork - in combination with modeling and theoretical efforts - are needed. Long term mooring arrays, designed to capture and describe the horizontal and vertical variability and structure of the plume, along with more intensive and focussed field campaigns on mixing would help shed light on the questions.

The sill region and the Filchner Depression proper are regions of interest that have not at all been touched upon here. How is the overflow controlled at the sill? Is the observed variability generated here or on the open slope?

Another interesting question is the development of the wedge shaped interface in the canyon and along the ridge. This feature has been observed in previous studies, but its origin is not fully understood. The secondary circulation is probably a factor, and a set of a laboratory experiments focused on this circulation, e.g. on the exchange between the Ekman layer and the interior at the dense layer edges, would likely shed light on the origins of the wedge.

As of today, no realistic numerical model of the Filchner area exists. The development of such a model has started (D. Feltham, personal communication) and it will be a good - or even indispensable - complement to fieldwork and other activities. In addition, idealized two- or three-dimensional model studies of flow along a sloping ridge (or canyon) would be a natural step up from the one-dimensional analytical and numerical models presented here. Such a model could encompass interactions with the upper layer as well as the "turning region" where the plume impinges on the ridge and is steered downslope, a region much too complicated for an analytical model to grasp. It would be interesting pursuing the work on the advection term, using a higher resolution two- or three-dimensional model to estimate the effect of the neglectance/mal-representation of this term. The possibility of including the results of topographic steering by small-scale topography in large-scale ocean model parameterizations should also be explored.

References

Abramowitz, M. & Stegun, I. (1970), *Handbook of Mathematical Functions*, Dover Publications, New York.

Adcroft, A., Hill, C. & Marshall, J. (1997), 'Representation of topography by shaved cells in a height coordinate ocean model', *Monthly Weather Review* **125**(9), 2293–2315.

Adduce, C. & Cendese, C. (2007), 'Mixing in a density driven current down a slope in a rotating fluid', *Journal of Fluid Mechanics* (submitted).

Alendal, G., Drange, H. & Haugan, P. M. (1994), Modelling of deep-sea gravity currents using an integrated plume model, *in* O. M. Johannessen, R. D. Muench & J. E. Overland, eds, 'The Polar Oceans and Their Role in Shaping the Global Environment, Geophysical Monograph Series', Vol. 85, AGU, Washington D.C.

Arneborg, L., Fiekas, V., Umlauf, L. & Burchard, H. (2007), 'Gravity current dynamics and entrainment - a process study based on observations in the arkona Basin', *Journal of Physical Oceanography* (submitted).

Baines, P. G. (2001), 'Mixing in flows down gentle slopes into stratified environments', *Journal of Fluid Mechanics* **443**, 237–270.

Baines, P. G. (2005), 'Mixing regimes for the flow of dense fluid down slopes into stratified environments', *Journal of Fluid Mechanics* **538**, 245–267.

Baines, P. G. & Condie, S. (1998), Observations and modelling of antarctic downslope flows: a review, *in* S. S. Jacobs & R. F. Weiss, eds, 'Ocean, Ice, and Atmosphere - Interaction at the Antarctic Continental Margin', Vol. 75, AGU, Washington D.C.

Balmforth, N. J. & Mandre, S. (2004), 'Dynamics of roll waves', *Journal of Fluid Mechanics* **514**, 1–33.

Borenäs, K. M. & Lundberg, P. A. (1988), 'On the deep-water flow through the Faroe Bank Channel', *Journal of Geophysical Research-Oceans* **93**(C2), 1281–1292.

Broecker, W. S. (1997), 'Thermohaline circulation, the achilles heel of our climate system: Will man-made CO2 upset the current balance?', *Science* **278**(5343), 1582–1588.

Broecker, W. S., Peacock, S. L., Walker, S., Weiss, R., Fahrbach, E., Schroeder, M., Mikolajewicz, U., Heinze, C., Key, R., Peng, T. H. & Rubin, S. (1998), 'How much deep water is formed in the Southern Ocean?', *Journal of Geophysical Research-Oceans* **103**(C8), 15833–15843.

Bruce, J. G. (1995), 'Eddies southwest of the Denmark Strait', *Deep-Sea Research Part I-Oceanographic Research Papers* **42**(1), 13–29.

Campin, J. M. & Goosse, H. (1999), 'Parameterization of density-driven downsloping flow for a coarse-resolution ocean model in z-coordinate', *Tellus Series A - Dynamic Meteorology and Oceanography* **51**(3), 412–430.

Carmack, E. C. & Foster, T. D. (1975), 'Flow of water out of Weddell Sea', *Deep-Sea Research* **22**(11), 711–724.

Cenedese, C., Whitehead, J. A., Ascarelli, T. A. & Ohiwa, M. (2004), 'A dense current flowing down a sloping bottom in a rotating fluid', *Journal of Physical Oceanography* **34**(1), 188–203.

Cushman-Roisin, B. (1994), *Introduction to Geophyscial Fluid Dynamics*, Prentics-Hall Inc., Upper Saddle River, New Jersey.

Davies, P., Wåhlin, A. & Guo, Y. (2006), 'Laboratory and analytical model studies of the FBC deep water outflow', *Journal of Physical Oceanography* **36**(7), 1348–1364.

Deacon, G. (1937), 'The hydrology of the Southern Ocean', *Discovery Report* **15**, 1–24.

Ekman, V. (1905), 'On the influence of the Earth's rotation on ocean-currents', *Arkiv for Matematik, Astronomi och Fysik* **2**(11), 1–52.

Ellison, T. H. & Turner, J. S. (1959), 'Turbulent entrainment in stratified flows', *Journal of Fluid Mechanics* **6**(3), 423–448.

Etling, D., Gelhardt, F., Schrader, U., Brennecke, F., Kuhn, G., d'Hieres, G. C. & Didelle, H. (2000), 'Experiments with density currents on a sloping bottom in a rotating fluid', *Dynamics of Atmospheres and Oceans* **31**(1-4), 139–164. Sp. Iss. SI.

Ezer, T. (2006), 'Topographic influence on overflow dynamics: Idealized numerical simulations and the Faroe Bank Channel overflow', *Journal of Geophysical Research* **111**(C02002).

Fahrbach, E., Rohardt, G. & Krause, G. (1992), 'The Antarctic coastal current in the Southeastern Weddell Sea', *Polar Biology* **12**(2), 171–182.

Fahrbach, E., Harms, S., Rohardt, G., Schroder, M. & Woodgate, R. A. (2001), 'Flow of bottom water in the northwestern Weddell Sea', *Journal of Geophysical Research-Oceans* **106**(C2), 2761–2778.

Fer, I., Lemmin, U. & Thorpe, S. A. (2001), 'Cascading of water down the sloping sides of a deep lake in winter', *Geophysical Research Letters* **28**(10), 2093–2096.

Fer, I., Lemmin, U. & Thorpe, S. A. (2002), 'Winter cascading of cold water in Lake Geneva', *Journal of Geophysical Research-Oceans* **107**(C6).

Foldvik, A. & Kvinge, T. (1974), 'Conditional instability of sea-water at freezing-point', *Deep-Sea Research* **21**(3), 169–174.

Foldvik, A. & Gammelsrød, T. (1988), 'Notes on Southern-Ocean Hydrography, Sea-Ice and Bottom Water Formation', *Palaeogeography Palaeoclimatology Palaeo-ecology* **67**(1-2), 3–17.

Foldvik, A., Gammelsrød, T. & Tørresen, T. (1985*a*), Circultion and water masses on the southern Weddell Sea shelf, *in* S. S. Jacobs, ed., 'Oceanology of the Antarctic Continental Shelf', Vol. 43, AGU, Washington D.C.

Foldvik, A., Gammelsrød, T. & Tørresen, T. (1985*b*), 'Hydrographic Observations from the Weddell Sea during the Norwegian antarctic Research Expedition 1976/1977', *Polar Research* **3**, 177–193.

Foldvik, A., Gammelsrød, T. & Tørresen, T. (1985*c*), 'Physical oceanography studies in the Weddell Sea during the Norwegian antarctic Research Expedition 1978/79', *Polar Research* **3**, 195–207.

Foldvik, A., Gammelsrød, T., Østerhus, S., Fahrbach, E., Rohardt, G., Schrøder, M., Nicholls, K. W., Padman, L. & Woodgate, R. A. (2004), 'Ice shelf water overflow and bottom water formation in the southern Weddell Sea', *Journal of Geophysical Research-Oceans* **109**(C2).

Ford, R., Pain, C. C., Piggott, M. D., Goddard, A. J. H., de Oliveira, C. R. E. & Umpleby, A. P. (2004), 'A nonhydrostatic finite-element model for three-dimensional stratified oceanic flows. Part I: Model formulation', *Monthly Weather Review* **132**(12), 2816–2831.

Foster, T. D. & Carmack, E. C. (1976*a*), 'Temperature and salinity structure in the Weddell Sea', *Journal of Physical Oceanography* **6**(1), 36–44.

Foster, T. D. & Carmack, E. D. (1976*b*), 'Frontal zone mixing and Antarctic Bottom Water formation in the Southern Weddell Sea', *Deep Sea Research* **230**, 301–317.

Foster, T. D., Foldvik, A. & Middleton, J. H. (1987), 'Mixing and bottom water formation in the shelf break region of the southern Weddell Sea', *Deep-Sea Research Part A-Oceanographic Research Papers* **34**(11), 1771–1794.

Gawarkiewicz, G. & Chapman, D. C. (1995), 'A numerical study of dense water formation and transport on a shallow, sloping continental-shelf', *Journal of Geophysical Research-Oceans* **100**(C3), 4489–4507.

Geyer, F., Østerhus, S., Hansen, B. & Quadfasel, D. (2006), 'Observations of highly regular oscillations in the overflow plume downstream of the Faroe Bank Channel', *Journal of Geophysical Research* **111**(C12020).

Gill, A. (1973), 'Circulation and bottom water production in the Weddell Sea', *Deep Sea Research* **20**, 111–140.

Gill, A. (1982), *Atmosphere-Ocean Dynamics*, Academic Press, San Dieago.

Girton, J. B. & Sanford, T. B. (2003), 'Descent and modification of the overflow plume in the Denmark Strait', *Journal of Physical Oceanography* **33**(7), 1351–1364.

Gordon, A. (1978), 'Deep antarctic convection west of Maud Rise', *Journal of Physical Oceanography* **8**(4), 600–612.

Gordon, A., Zambianchi, E., Orsi, A., Visbeck, M., Giulivi, C., Whitworth, T. & Spezie, G. (2004), 'Energetic plumes over the western Ross Sea continental slope', *Geophysical Research Letters* **31**(21).

Gordon, A., Price, J., Peters, H. & Girton, J. (2007), 'Observationalists' Table of Plumes', *http://cpt-gce.org/Table_of_observations.htm* (20070625).

Griffies, S. M., Böning, C., Bryan, F. O., Chassingnet, E. P., Gerdes, R., Hasumi, H., Hirst, A., Treguier, A. & Webb, D. (2000), 'Developments in ocean climate modelling', *Ocean Modelling* **2**, 123–192.

Grosfeld, K. & Hellmer, H. (1998), Marine ice beneath Filchner Ice Shelf: Evidence from a multi-disciplinary approach, *in* S. S. Jacobs & R. F. Weiss, eds, 'Ocean, Ice, and Atmosphere - Interaction at the Antarctic Continental Margin', Vol. 75, AGU, Washington D.C.

Haidvogel, D. & Beckmann, A. (1999), *Numerical Ocean Circulation Modelling*, Vol. 2 of *Series on Environmental Science and Management*, Imperial College Press, London.

Hallberg, R. (2000), 'Time integration of diapycnal diffusion and Richardson number-dependent mixing in isopycnal coordinate ocean models', *Monthly Weather Review* **128**(5), 1402–1419.

Hansen, B. & Østerhus, S. (2000), 'North Atlantic-Nordic Seas exchanges', *Progress in Oceanography* **45**(2).

Heggelund, Y., Vikebo, F., Berntsen, J. & Furnes, G. (2004), 'Hydrostatic and non-hydrostatic studies of gravitational adjustment over a slope', *Continental Shelf Research* **24**(18), 2133–2148.

Hellmer, H. (2006), Weddell, Sea, Oceanography of, *in* 'Encyclopedia of the Antarctic', Vol. 2, Riffenburgh.

Hughes, G. O. & Griffiths, R. W. (2006), 'A simple convective model of the global overturning circulation, including effects of entrainment into sinking regions', *Ocean Modelling* **12**, 46–97.

Ivanov, V., Shapiro, G., Huthnance, J., Aleynik, D. & Golovin, P. (2004), 'Cascades of dense water around the world ocean', *Progress in Oceanography* **60**(1), 47–98.

Jacobs, S. (2004), 'Bottom water production and its links with the thermohaline circulation', *Antarctic Science* **16**(4), 427–437.

Jiang, L. & Garwood, R. W. (1995), 'a numerical study of 3-dimensional dense bottom plumes on a Southern-Ocean continental-slope', *Journal of Geophysical Research-Oceans* **100**(C9), 18471–18488.

Jiang, L. & Garwood, R. W. (1996), 'Three-dimensional simulations of overflows on continental slopes', *Journal of Physical Oceanography* **26**(7), 1214–1233.

Jiang, L. & Garwood, R. W. (1998), 'Effects of topographic steering and ambient stratification on overflows on continental slopes: a model study', *Journal of Geophysical Research-Oceans* **103**(C3), 5459–5476.

Jungclaus, J. H. & Backhaus, J. O. (1994), 'application of a transient reduced gravity plume model to the Denmark Strait Overflow', *Journal of Geophysical Research-Oceans* **99**(C6), 12375–12396.

Jungclaus, J. H., Backhaus, J. O. & Fohrmann, H. (1995), 'Outflow of dense water from the Storfjord in Svalbard: a numerical model study', *Journal of Geophysical Research-Oceans* **100**(C12), 24719–24728.

Jungclaus, J. H., Hauser, J. & Käse, R. H. (2001), 'Cyclogenesis in the Denmark Strait overflow plume', *Journal of Physical Oceanography* **31**(11), 3214–3229.

Käse, R. H., Girton, J. B. & Sanford, T. B. (2003), 'Structure and variability of the Denmark Strait Overflow: Model and observations', *Journal of Geophysical Research-Oceans* **108**(C6).

Killworth, P. D. (1977), 'Mixing on the Weddell Sea continental slope', *Deep-Sea Research* **24**, 427–448.

Killworth, P. D. (2001), 'O the rate of descent of overflows', *Journal of Geophysical Research-Oceans* **106**(C10), 22267–22275.

Killworth, P. D. & Edwards, N. R. (1999), 'A turbulent bottom boundary layer code for use in numerical ocean models', *Journal of Physical Oceanography* **29**(6), 1221–1238.

Krauss, W. (1996), 'A note on overflow eddies', *Deep-Sea Research Part I-Oceanographic Research Papers* **43**(10), 1661–1667.

Krauss, W. & Käse, R. H. (1998), 'Eddy formation in the Denmark Strait Overflow', *Journal of Geophysical Research-Oceans* **103**(C8), 15525–15538.

Lane-Serff, G. (2001), Overflows and cascades, *in* J. Steele, S. Thorpe & K. Turekian, eds, 'Encyclopedia of Ocean Sciences', Elsevier, Amsterdam.

Lane-Serff, G. F. & Baines, P. G. (1998), 'Eddy formation by dense flows on slopes in a rotating fluid', *Journal of Fluid Mechanics* **363**, 229–252.

Lane-Serff, G. F. & Baines, P. G. (2000), 'Eddy formation by overflows in stratified water', *Journal of Physical Oceanography* **30**(2), 327–337.

Legg, S., Hallberg, R. W. & Girton, J. B. (2006), 'Comparison of entrainment in overflows simulated by z-coordinate, isopycnal and non-hydrostatic models', *Ocean Modelling* **11**(1-2), 69–97.

MacDonald, A. M. & Wunsch, C. (1996), 'An estimate of global ocean circulation and heat fluxes', *Nature* **382**(6590), 436–439.

Mauritzen, C. (1996), 'Production of dense overflow waters feeding the North atlantic across the Greenland-Scotland Ridge.1. Evidence for a revised circulation scheme', *Deep-Sea Research Part I-Oceanographic Research Papers* **43**(6), 769–806.

Mauritzen, C., Price, J., Sanford, T. & Torres, D. (2005), 'Circulation and mixing in the Faroese Channels', *Deep-Sea Research Part I-Oceanographic Research Papers* **52**(6), 883–913.

Middleton, J. H., Foster, T. D. & Foldvik, A. (1987), 'Diurnal shelf waves in the southern Weddell Sea', *Journal of Physical Oceanography* **17**(6), 784–791.

Nicholls, K. W., Østerhus, S., Makinson, K. & Johnson, M. R. (2001), 'Oceanographic conditions south of Berkner Island, beneath Filchner-Ronne Ice Shelf, antarctica', *Journal of Geophysical Research-Oceans* **106**(C6), 11481–11492.

Nicholls, K. W., Padman, L., Schröder, M., Woodgate, R., Jenkins, A. & Østerhus, S. (2003), 'Watermass modification over the continental shelf north of Ronne Ice Shelf, antarctica', *Journal of Geopysical Research* **108**(C8).

Nof, D. (1983), 'The translation of isolated cold eddies on a sloping bottom', *Deep-Sea Research Part A-Oceanographic Research Papers* **30**(2), 171–182.

Nøst, O. A. & Foldvik, A. (1994), 'a model of ice-shelf ocean interaction with application to the Filcher-Ronne and Ross Ice Shelves', *Journal of Geophysical Research-Oceans* **99**(C7), 14243–14254.

Orsi, A. & Whitworth, I. (2004), *Hydrographic atlas of the World Ocean Circulation Experiment (WOCE). Volume 1: Southern Ocean*, International WOCE Project Office, Southampthon (http://woceatlas.tamu.edu/).

Orsi, A. H., Johnson, G. C. & Bullister, J. L. (1999), 'Circulation, mixing, and production of antarctic Bottom Water', *Progress in Oceanography* **43**(1), 55–109.

Özgökmen, T. M. & Chassignet, E. P. (2002), 'Dynamics of two-dimensional turbulent bottom gravity currents', *Journal of Physical Oceanography* **32**(5), 1460–1478.

Padman, L. & Kottmeier, C. (2000), 'High-frequency ice motion and divergence in the Weddell Sea', *Journal of Geophysical Research-Oceans* **105**(C2), 3379–3400.

Price, J. & Baringer, M. (1994), 'Outflows and deep-water production by marginal seas', *Progress in Oceanography* **33**(3), 161–200.

Price, J. & Yang, J. (1998), Marginal sea overflows for climate simulations, *in* E. Chassignet & J. Verron, eds, 'Ocean Modeling and Parameterisation', Kluwer Academic Publishers, pp. 155–170.

Quadfasel, D., Rudels, B. & Kurz, K. (1988), 'Outflow of dense water from a Svalbard fjord into the Fram Strait', *Deep-Sea Research Part A-Oceanographic Research Papers* **A35**, 1143–1150.

Rahmstorf, S. (2006), Thermohaline ocean circulation, *in* S. Elias, ed., 'Encyclopedia of Quaternary Sciences', Elsevier, Amsterdam.

Riemenschneider, U. & Legg, S. (2007), 'Regional simulations of the Faroe Bank Channel overflow in a level model', *Ocean Modelling* **17**(2), 93–122.

Robertson, R. (2005), 'Baroclinic and barotropic tides in the Weddell Sea', *Antarctic Science* **17**(3), 461–474.

Robertson, R., Padman, L. & Egbert, G. D. (1998), Tides in the Weddell Sea, *in* 'Ocean, Ice and Atmosphere: interactions at the Antarctic Continental Margin', Vol. 75 of *Antarctic Research Series*, AGU, pp. 341–369.

Rumford, B. (1800), The propagation of heat in fluids, *in* T. Cadell & W. Davies, eds, 'Essays, Political, Economical, and Philosophical, A New Edition', Vol. 2, London.

Saunders, P. (2001), The dense northern overflows, *in* G. Siedler, J. Church & J. Gould, eds, 'Ocean Circulation and Climate', Vol. 77 of *International Geophysics Series*, Academic Press, pp. 401–418.

Schlitzer, R. (2007), 'Assimilation of radiocarbon and chlorofluorocarbon data to constrain deep and bottom water transports in the world ocean', *Journal of Physical Oceanography* **37**(2), 259–276.

Simons, T. (1980), 'Circulation models of lakes and inland seas', *Canadian Bullentin of Fisheries and Aquatic Sciences* **203**.

Smith, P. C. (1975), 'A streamtube model for bottom boundary currents in the ocean', *Deep Sea Research* **22**.

Smith, P. C. (1976), 'Baroclinic instability in Denmark Strait Overflow', *Journal of Physical Oceanography* **6**(3), 355.

Smith, P. C. (1977), 'Experiments with viscous source flows in rotating systems', *Dynamics of Atmospheres and Oceans* **1**(3), 241–272.

Spall, M. A. (2004), 'Boundary currents and watermass transformation in marginal seas', *Journal of physical oceanography* **34**(5), 1197.

Spall, M. A. & Price, J. F. (1998), 'Mesoscale variability in Denmark Strait: The PV outflow hypothesis', *Journal of Physical Oceanography* **28**(8), 1598–1623.

Stelling, G. & Duinmeijer, S. (2003), 'A staggered conservative scheme for every Froude number in rapidly varied shallow water flows', *International Journal for Numerical Methods in Fluids* **43**, 1329–1354.

Sverdrup, H. (1953), 'The currents off the coast of Queen Mauds Land', *Norsk Geografisk Tidskrift* **XIV**.

Swaters, G. E. (1991), 'O the baroclinic instability of cold-core coupled density fronts on a sloping continental-shelf', *Journal of Fluid Mechanics* **224**, 361–382.

Swaters, G. E. (2003), 'Baroclinic characteristics of frictionally destabilized abyssal overflows', *Journal of Fluid Mechanics* **489**, 349–379.

Tanaka, K. (2006), 'Effects of the Earth's rotation and bottom slope on a density current descending a sloping bottom', *Journal of Geophysical Research-Oceans* **111**(C11).

Tanaka, K. & Akitomo, K. (2001), 'Baroclinic instability of density current along a sloping bottom and the associated transport process', *Journal of Geophysical Research-Oceans* **106**(C2), 2621–2638.

Turner, J. S. (1986), 'Turbulent entrainment - the development of the entrainment assumption, and its application to geophysical flows', *Journal of Fluid Mechanics* **173**, 431–471.

Warren, B. (1981), Deep circulation of the World Ocean, *in* B. Warren & C. Wunsch, eds, 'Evolution of physical Ocenography', MIT Press, Cambridge, Massachusetts and London, England.

Warren, S. G., Roesler, C. S., Morgan, V. I., Brandt, R. E., Goodwin, I. D. & Allison, I. (1993), 'Green icebergs formed by freezing of organic-rich sea water to the base of Antarctic ice shelves', *Journal of Geophysical Research-Oceans* **98**(C4), 6921–6928.

Wells, M. G. & Wettlaufer, J. S. (2005), 'Two-dimensional density currents in a confined basin', *Geophysical And Astrophysical Fluid Dynamics* **99**(3), 199–218.

Willebrand, J., Barnier, B., Boning, C., Dieterich, C., Killworth, P. D., Le Provost, C., Jia, Y. L., Molines, J. M. & New, A. L. (2001), 'Circulation characteristics in three eddy-permitting models of the North atlantic', *Progress in Oceanography* **48**(2-3), 123–161.

Winton, M., Hallberg, R. & Gnanadesikan, A. (1998), 'Simulation of density-driven frictional downslope flow in Z-coordinate ocean models', *Journal of Physical Oceanography* **28**(11), 2163–2174.

Wunsch, C. (2002), 'What is the thermohaline circulation?', *Science* **298**(5596).

Wåhlin, A. K. (2002), 'Topographic steering of dense currents with application to submarine canyons', *Deep-Sea Research Part I-Oceanographic Research Papers* **49**(2), 305–320.

Wåhlin, A. K. & Walin, G. (2001), 'Downward migration of dense bottom currents', *Environmental Fluid Mechanics* **1**, 257 – 259.

Wåhlin, A. K. & Cenedese, C. (2006), 'How entraining density currents influence the stratification in a one-dimensional ocean basin', *Deep-Sea Research Part II-Topical Studies In Oceanography* **53**(1-2), 172–193.

APPENDIX: Complementary Work

A A one-dimensional plume model: results from a sloping canyon

A one-dimensional, 1.5-layer numerical model written by L. Umlauf was applied to a sloping cosine shaped canyon. The model solves a depth integrated version of the momentum equation using a conservative algorithm described by Stelling & Duinmeijer (2003)[8]. The model uses a staggered grid, where grid-box properties such as the layer thickness, h, are calculated in the center of the box, while velocities, u, v and w, are given at the box borders. For a one-dimensional model (in the y-z plane) this means that u and h are given at $y_i, y_{i+1}, ..., y_n$ while v is given at $0.5(y_i + y_{i+1}), 0.5(y_{i+1} + y_{i+2}), ..., 0.5(y_{n-1} + y_n)$.

The interface of the dense, lower layer was initially horizontal and had a maximum thickness, H_0, in the center of the canyon, which had a slope s, a width W_c and a height H_c. The model was initialized and allowed to run until a steady state was achieved, normally 288 h (12 days). More than 70 runs were performed and the physical parameters (H_0, f, C_d and $\Delta\rho$) were varied along with the geometrical (s, W_c and H_c) taking on values according to Table 2. f is the Coriolis factor and C_d is the bottom drag coefficient.

Fig. 11 presents the results for three runs with H_0=100 m, f=10^{-4} s^{-1}, C_d=4×10^{-3}, $\Delta\rho$=0.1 kg/m^3, W=2.5 km and D=300 m and where the bottom slope s was varied according to the legend. Analytical solutions, calculated using the same parameters and required to intersect the right canyon wall at the same point as the numerical solution, are plotted in

[8] Equation 1b in Stelling & Duinmeijer (2003) is slightly modified: velocity is replaced by transport and the Coriolis term is added

the same figure. It should be noted that the models use different friction parameterizations, and that the solutions are expected to differ.

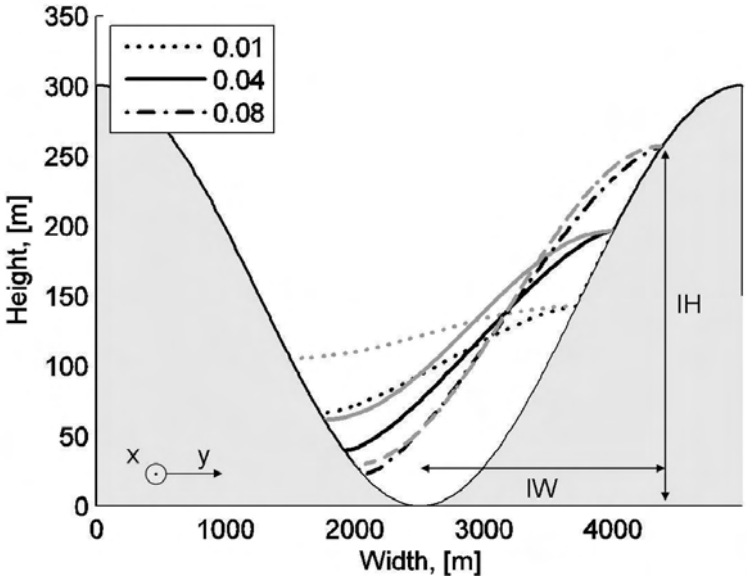

Figure 11: *Numerical (black) and analytical (gray) solutions for experiments with varied bottom slope, s.*

Parameter		Values	Unit
Initial water depth	H_0	25-150	m
Coriolis factor	f	$0.5 \times 10^{-4} - 2 \times 10^{-4}$	s^{-1}
Drag coefficient	C_d	$2 \times 10^{-3} - 4 \times 10^{-3}$	
Density difference	$\Delta\rho$	0.1	kg/m^3
Bottom slope	s	0.001-0.075	
Canyon width	W_c	1-5.5	km
Canyon depth	H_c	300	m
Ekman l. t.	δ	11-61	m

Table 2: *Physical, geometrical and derived parameter interval used in model runs (l. t. = layer thickness)*

The numerical and analytical solutions have the same general form, but the characteristic flattening of the interface close to the canyon walls observed in the analytical solutions (**Paper I**) and in the laboratory experiments (**Paper II**) is less pronounced in the numerical solutions. The numerical solutions are more similar to the analytical for large bottom slopes, s. For low values of s, the "effective" slope seems to be higher for the numerical solutions, i.e. the numerical solution for $s = s_1$, resembles the analytical solution for $s = s_2$, where $s_2 > s_1$. The difference between s_1 and s_2 is larger for smaller s.

The down-canyon transport, Q, was calculated from the model results according to

$$Q = \sum_{i=1}^{i=n} h_i u_i dy \tag{4}$$

where h_i and u_i is the layer thickness and downslope velocity at grid point i and dy the distance between two grid points in the y-direction. The transport for the three runs presented in Fig. 11 are 0.05/0.11/0.14 Sv for s equal to 0.01/0.04/0.08 respectively, while the corresponding analytical solutions have transports of similar magnitude $Q = 0.04/0.13/0.16$ Sv. It should be noted that the numerical transport is the actual transport, while the analytical solutions give the geostrophic transport only.

The transports were non-dimensionalized using the scaling presented in **Paper I**, i.e.

$$\hat{Q} = \frac{f}{g' IH^2} Q \tag{5}$$

where f and g' is the Coriolis factor and the reduced gravity as before, and IH the interface height as indicated in Fig. 11. It was shown in **Paper I** that the non-dimensionalized transport, $\hat{Q}$, for the analytical solutions is a function only of γ, where $\gamma = sW_c/\delta$ and δ is the thickness of the Ekman layer. For the numerical solutions, γ was defined as

$$\gamma = \frac{sIW}{\delta} \tag{6}$$

where IW is the width of the flow as defined in Fig. 11. Since the dense layer does not fill the canyon, i.e. since the interface does not reach the height of the canyon, $IH < H_c$ and thus $IW < W_c$. The model uses a quadratic friction formulation and the thickness of the Ekman layer, δ was therefore calculated according to

$$\delta = \frac{C_d g' \alpha}{f^2} \tag{7}$$

where $\alpha \approx tan(H_c/W_c)$.

Fig. 12 shows the non-dimensionalized transport, $\hat{Q}$, as a function of the calculated value for γ together with the corresponding analytical curve. For a given value of H_0, the points

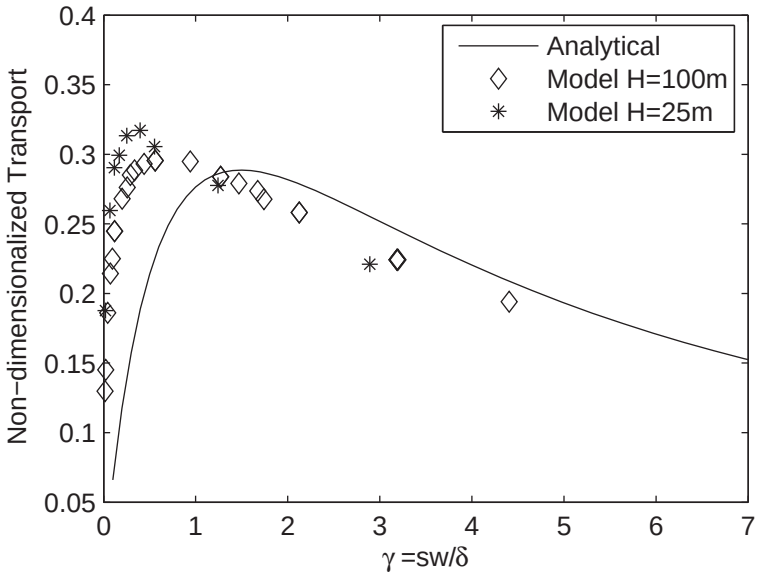

Figure 12: *Non-dimensionalized downslope transport as a function of γ for the numerical and theoretical model.*

seem to collapse onto a curve with a shape similar to the analytical curve. The "numerical curve" is, however, compressed compared with the analytical, and more so for a small value of H_0.

The comparison and the definition of the parameters are not straightforward. The thickness of the Ekman layer, δ, for example, does not appear explicitly in the numerical model while it does so in the analytical model, and due to different friction parameterizations it must be differently defined. It is likely that the apparent compression of the numerical curve is due to different expressions of δ. The differences regarding slope in Fig. 11 could probably also be explained by differences in friction parameterization, i.e. in the "effective" thickness of the Ekman layer. The dependence of the compression on H_0 is somewhat puzzling.

The analytical curve in Fig. 12 is based on "full canyons", i.e. canyons where $IW = W_c$ and $IH = H_c$, while for the numerical solutions $IW < W_c$ and $IH < H_c$. With the changes made in the definitions of $\hat{Q}$ and γ (equations 5-6) the error so introduced ought to be relative small. For a linear canyon the error would be zero.

The numerical model was initially applied in order to clarify the effect of the advection

terms on the solutions. The advection term of interest, vu_y, is in this model set-up equal to zero in steady state. This is due to an simplification made when deriving the depth integrated versions of the momentum equation. The advection term and the simplification are further discussed in the following section.

B A note on the advection term in a vertically integrated model

It will be shown that a simplification made during the derivation of the equation of motion for vertically integrated models leads to a mal-representation of a term that may be relatively large.

The advection terms are products of two terms, e.g. uu_x and vu_y, and it is not possible to integrate them vertically for a general case. The integration of the product is therefore often replaced with the product of the two terms integrated separately (Simons 1980). This approximation is strictly valid only when either the property being advected (e.g. heat or momentum) or the velocity is constant over the layer. The error can be expected to be small when the resolution is high enough (i.e. the layers thin enough) to satisfactorily resolve vertical shear. The use of the approximation means that the advection terms in models of this type are zero whenever the volume flux is so. This is not always true. As a simple illustration "volume" and "momentum" can be replaced with "people" and "groceries". Through the doors of a supermarket there may be a zero net flux of people (there are just as many people going in as out) but a non-zero "advection" of groceries (since they all enter empty handed and leave with their bags full).

Applying the approximation, the vertically integrated form of the equations of motions can be written (e.g. Jungclaus & Backhaus (1994)[9])

$$\frac{\partial U}{\partial t} + \nabla \cdot \mathbf{V}\frac{U}{H} - fV = -g'H\frac{\partial \zeta}{\partial x} - \frac{gH^2}{2\rho_0}\frac{\partial \rho}{\partial x} - \frac{\tau_{b,x}}{\rho_0} \tag{8}$$

where we have defined $\mathbf{V} = (U, V)$ and

$$U = \int_D^{D+H} u dz \tag{9}$$

$$V = \int_D^{D+H} v dz \tag{10}$$

and where g' is the reduced gravity, ρ_0 a reference density, H the thickness of the layer, ζ the interface level and $\tau_{b,x}$ the bottom stress in the x-direction.

[9] The horizontal advection term appearing in their form of the equations has been neglected

To derive (8) we start with the equations of motion, expressed on flux form (Gill 1982)

$$\frac{\partial(\rho u)}{\partial t} + \nabla \cdot (\rho u \mathbf{u}) + 2\Omega_y \rho w - 2\Omega_z \rho v = -\frac{\partial p}{\partial x} \tag{11}$$

and integrate vertically over a layer, which is assumed to be homogenous, $\rho = \rho_0$, and has thickness H. We focus on the advection term (term 2 in (11)), which we hereafter call M. For simplicity we assume that the flow is non-changing in the x-direction ($u_x = 0$, $h_x = 0$) and get (after division by ρ_0)

$$M = \int_D^{D+H} \frac{\partial(uv)}{\partial y} dz + \int_D^{D+H} \frac{\partial(uw)}{\partial z} dz \tag{12}$$

or

$$M = \int_D^{D+H} \frac{\partial(uv)}{\partial y} dz + uw|_{z=D+H} - uw|_{z=D}. \tag{13}$$

A particle on the surface/bottom must remain on the surface/bottom and so for $h_x = 0$

$$w(D(x,y) + h(y)) = v\frac{\partial(D+H)}{\partial y} \tag{14}$$

and

$$w(D(x,y)) = v\frac{\partial D}{\partial y}, \tag{15}$$

which means that M can be written

$$M = \int_D^{D+H} \frac{\partial(uv)}{\partial y} dz + (uv)|_{z=D+H} \frac{\partial(D+H)}{\partial y} - (uv)|_{z=D} \frac{\partial D}{\partial y}. \tag{16}$$

Using Leibniz's theorem for differentiation of an integral (e.g. Abramowitz & Stegun (1970), p11) M can again be rewritten

$$M = \frac{\partial}{\partial y} \int_{D(x,y)}^{D(x,y)+h(y)} uv dz. \tag{17}$$

To proceed one must assume that the vertical average of the product of two variables may be approximated by the product of the variables' vertical average, i.e. that

$$\int_D^{D+H} uv dz \approx \frac{1}{H} \int_D^{D+H} u dz \cdot \int_D^{D+H} v dz, \tag{18}$$

which gives

$$M = \frac{\partial}{\partial y} \frac{UV}{H} \tag{19}$$

or the advection term (term 2) in (8)[10].

Using (8) on the canyon/ridge flows, where we have V=0 gives that the advection term, $\nabla \cdot (\vec{v}\frac{U}{H})$ is identical to zero in the x-direction momentum equation[11]. It will be shown

[10] The expressions are identical if (8) is reformulated to include the assumption of negligible x-derivates

[11] The horizontal diffusion term is neglected as before

below that the advection term may be relatively large. The discrepancy arises from the approximation (18), which is used in all vertically integrated models. The simplification is problematic whenever the resolution is not high enough to satisfactorily resolve vertical shear, e.g. if the Ekman dynamics, as in our case, are not explicitly resolved. Returning to the example with people and groceries, we have that the approximation is valid if the "resolution" is high enough for the entrance and exit doors to be treated separately.

To compare the integrated advection term (17) with the other terms in the equation of motion (8) one needs expressions for $u(y,z)$ and $v(y,z)$. The vertical structure within the topographically steered plume is assumed to be given by Ekman theory

$$\begin{aligned} u(z) &= U_0[1 - e^{-z/\delta}cos(z/\delta)] - V_0 e^{-z/\delta}sin(z/\delta) \\ v(z) &= U_0 e^{-z/\delta}sin(z/\delta) + V_0[1 - e^{-z/\delta}cos(z/\delta)] \end{aligned} \tag{20}$$

where U_0 and V_0 are the velocities in the interior, z height over bottom and δ the thickness of the Ekman layer (Cushman-Roisin 1994). To encompass (20) the equations presented in **Paper I** must be slightly modified. Equation (12) in **Paper I** is replaced by

$$h + \frac{\partial h}{\partial y}\left(\frac{\delta}{2s}\right) = \frac{d}{2}\left(1 - \frac{\partial D}{\partial y}\right) \tag{21}$$

where h is the layer thickness, D the bottom elevation, δ the thickness of the Ekman layer and s the background slope (the equation is not non-dimensionalized and the y-axis is, like in **Paper I**, directed perpendicular to the topography crosscutting the slope). Here two cosine-shaped ridges with oceanic (W=3000 m, H=300 m) and laboratory (W=0.03 m, H=0.03 m) dimensions are considered. The solution to (21) giving the maximum transport (see **Paper I** for a discussion on transport capacity and different solutions) is then

$$h(y) = \left(-\frac{HK^2}{2(1+K^2)} - \frac{\delta}{2}\right)e^{2(sy/\delta - \pi/K)} + \frac{HK}{2(1+K^2)}\left[-\frac{H}{2}Kcos\left(\frac{\pi y}{W}\right) + sin\left(\frac{\pi y}{W}\right)\right] + \frac{\delta}{2} \tag{22}$$

where $K = \pi\delta/2Ws$, s=0.01, $f = 10^{-4}(0.8)$ s^{-1} and δ = 35 m (2 mm) for the oceanic (laboratory) case. This solution, which is plotted in Fig. 13a for the laboratory case, is valid only when $h >> \delta$, and thus not near the edges of the layer where other solutions must be sought. This will not be done here, and the edges must consequently be disregarded. When deriving the solution (22) the advection term has been neglected, either in accordance with the criteria $V = 0$ or on scaling premises. The velocity in the interior is thus assumed to be geostrophic, and we have

$$U_0 = \frac{g'}{f}h_y \tag{23}$$

$$V_0 = \frac{g'}{f}s \tag{24}$$

where $g' = 10^{-3}$ (10^{-2}) in the ocean (laboratory). Equations (23-24) can be combined with (20) to give $u(y,z)$ and $v(y,z)$. Given these expressions we can numerically calculate

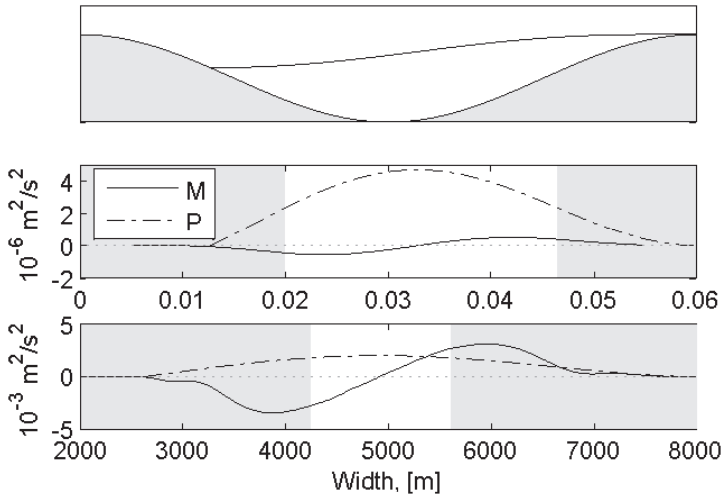

Figure 13: *a) Laboratory solution for canyon flow. The integrated momentum term and the integrated pressure term for canyon flow in b) laboratory and c) the ocean. In (b) and (c) the areas where solution 22 are not valid is shaded in gray.*

the advection term M from (17). The results using oceanic and laboratory parameters are presented in Fig. 13b-c, where the integrated pressure term

$$P = g'H\frac{\partial \zeta}{\partial x} = g'Hs \tag{25}$$

is included for comparison. The areas where solution 22 are not valid is shaded in gray. As seen, the momentum term, M, is not zero, as it would be using the approximation (18). In the oceanic case the advection term, M, and the pressure term, P, is of roughly equal magnitude, while P is much larger than M in the laboratory setting. Near the center of the canyon the term is small for both cases. Consequently, the geostrophic approximation, or the omission of the advection term caused by the simplification (18), is justified in the laboratory setting but questionable in the oceanic case.

Downward flow of dense water leaning on a submarine ridge

E. Darelius[1,2] **&** ***A. Wåhlin***[3,4]

(1) Geophysical Institute, University of Bergen, Norway
(2) Bjerknes Centre for Climate Research, Bergen, Norway
(3) MISU, Stockholm University, Stockholm, Sweden

Abstract

Large-scale dense bottom currents are geostrophic to leading order, with the main flow direction along the continental slope. Bottom friction makes the water descend to greater depths, but only at a small angle to the horizontal. Here the effect of a submarine ridge that intersects the slope is considered. It is shown that the presence of a submarine ridge greatly enhances the downslope transport. By leaning against the ridge it is possible for the dense water to flow downhill, perpendicular to the depth contours, even though the first-order dynamics are geostrophic. The requirement for downslope flow next to the ridge is that the frictional transport that it induces is sufficiently large to counteract geostrophic advection along the isobaths and out of the ridge region. The dynamics are similar to those of downslope flow in submarine canyons, but ridges appear to be more effective in channeling the dense water downhill, in particular for narrow ridges/canyons with small seaward slope of the ridge/canyon axis. The downslope flow is analyzed using a simplified analytical model and the results are compared to data from the Filchner Overflow, which agree qualitatively with the model.

1 Introduction

The formation of dense water in marginal seas and over the continental shelves in high latitudes is an important part of the thermohaline circulation, and presumably of relevance for our climate. However important, the path that this dense water follows to the deep ocean and the dynamics governing it are not fully understood. A better understanding is needed to, for example, more correctly represent overflows in global-scale ocean models (Legg et al. 2006, Campin & Goosse 1999).

Dense water entering an ocean basin through a gap or a strait will flow out along the continental slope as a plume of dense water. Such overflows are found for example in the Denmark Strait (Girton & Sanford 2003), the Mediterranean Outflow (Ambar & Howe 1979), the

Faroe Bank Channel (Mauritzen et al. 2005) and the Filchner Overflow (Foldvik et al. 2004). The dense water flows geostrophically along the isobaths, descending to greater depths only gradually because of friction (Wåhlin & Walin 2001, Killworth 2001, MacCready 1994). Killworth (2001) predicted the descent rate of dense plumes on a smooth bottom slope to be 1:400, i.e. the plume water descends 1 m vertically while advancing 400 m horizontally. The downslope transport of dense water may, however, be increased by eddies (Tanaka & Akitomo 2001, Chapman & Gawarkiewicz 1995) or by topographic steering. The latter will be the focus of this paper.

The continental slopes of the ocean basins are in general not smooth but interrupted by canyons, ridges and topographic corrugations. Submarine canyons have been observed to steer dense water downslope, for example in the Wyville Thompson Ridge Overflow, which descends inside a canyon intersecting the ridge (Sherwin et al. 2007, Sherwin & Turrell 2005), and in the Adriatic Sea where a canyon steers a portion of the cold water down into the deep Jabuka Pit (Vilibic et al. 2004). Topographic steering, or channeling, of dense water in canyons has also been observed in models (Kämpf 2000, Jiang & Garwood 1998) and laboratory experiments (Kämpf 2005, Baines & Condie 1998).

The dynamics of a frictionally modified geostrophic flow down a canyon was analyzed by Wåhlin (2002). A purely geostrophic current can not have a net transport down along the canyon axis, since it is forced to translate parallel to the depth contours (Wåhlin 2004, Nof 1983), i.e. flow along the slope and out of the canyon region. In reality, bottom and interfacial friction will, however, always be present, inducing an Ekman transport to the left (right in the southern hemisphere) of the main current. With the aid of friction it is possible to sustain a steady downslope flow inside the canyon, provided that the induced Ekman transport is sufficiently strong to balance the geostrophic slope advection out of the canyon. The dense water may thus remain in and flow down the canyon, while maintaining a transverse, secondary circulation much like the one observed within the canyon in the model study by Chapman & Gawarkiewicz (1995). A similar secondary circulation was also described and observed by Johnson & Ohlsen (1994) in their laboratory simulations of exchange flows through tubes and troughs.

Observations from the Filchner Overflow in the Weddell Sea, Antarctica, indicate that topographic steering also can take place in the vicinity of a submarine ridge (Foldvik et al. 2004). The Filchner Overflow consists of Ice Shelf Water (ISW), which is formed as water from the continental shelf in the southwestern Weddell Sea enters the cavity under the Filchner-Ronne Ice Shelf and interacts with the glacial ice (Nicholls & Østerhus 2004). Ice Shelf Water has a temperature below its surface freezing point (i.e. T<-1.9°C), a salinity of 34.6 (Foldvik et al. 1985*a*), and the potential to sink to the bottom of the Weddell Sea and participate in the formation of Antarctic Bottom Water. It exits the ice shelf cavity through the Filchner Depression (Foldvik et al. 1985*b*) and then flows west along the continental slope. Data from a mooring placed in the vicinity of a submarine ridge crosscutting the

continental slope west of the Filchner Depression show cold overflow water flowing downslope with great speed, and a nearby CTD section shows a layer of cold water leaning on the ridge. Downhill flow of dense water in the vicinity of a submarine ridge was also observed in the idealized model study by Jiang & Garwood (1998).

Here, downslope channeling of dense water leaning on a submarine ridge is explored. It is shown that a dynamical regime similar to the one described for canyon-flow can be established also along a ridge. Analytical solutions are obtained for five idealized submarine ridge geometries, and expressions for their capacity to transport water downhill are derived. The obtained transport capacities are remarkably insensitive to the shape of the ridge and depend most strongly on the ridge height and width and the seaward slope of the ridge axis. The transport capacity is larger for gentle shelf slopes and steep ridge walls and for flows where the bottom boundary layer is thick compared to the ridge height. For such geometries, ridges are in fact more effective than canyons in channeling water downslope. The reason is that the downslope ridge-flow then becomes rather wide and occupies a large area on the slope, while the canyon-flow is restricted laterally by the canyon walls. Data from the mooring and the CTD section mentioned earlier are compared to the theoretical results and are shown to agree qualitatively.

2 Theory

Fig. 1a shows a sketch of a (Northern-hemisphere) dense plume flowing over a topography with bottom elevation $D(x, y)$. The coordinate system is chosen so that the x-axis is pointing upslope. The thickness of the dense layer is $h(x, y)$ and it underlies an upper (lighter) layer that is infinitely deep and at rest. The two layers thus form a 1.5-layer system. Assuming that the Rossby numbers are small and that bottom friction can be described by a linear bulk friction parameterization, the vertically integrated Navier-Stokes equations in the x- and y-directions can be written

$$-fv = -g'(h_x + D_x) - \frac{K}{h}u \tag{1}$$

and

$$fu = -g'(h_y + D_y) - \frac{K}{h}v \tag{2}$$

where f is the Coriolis parameter, g' is the reduced gravity and K is a linear bulk friction coefficient. The vertically integrated horizontal velocities (u, v) in the (x, y) directions are hence defined as

$$u(x, y) = \frac{1}{h}\int_{D}^{D+h} U(x, y, z)dz \tag{3}$$

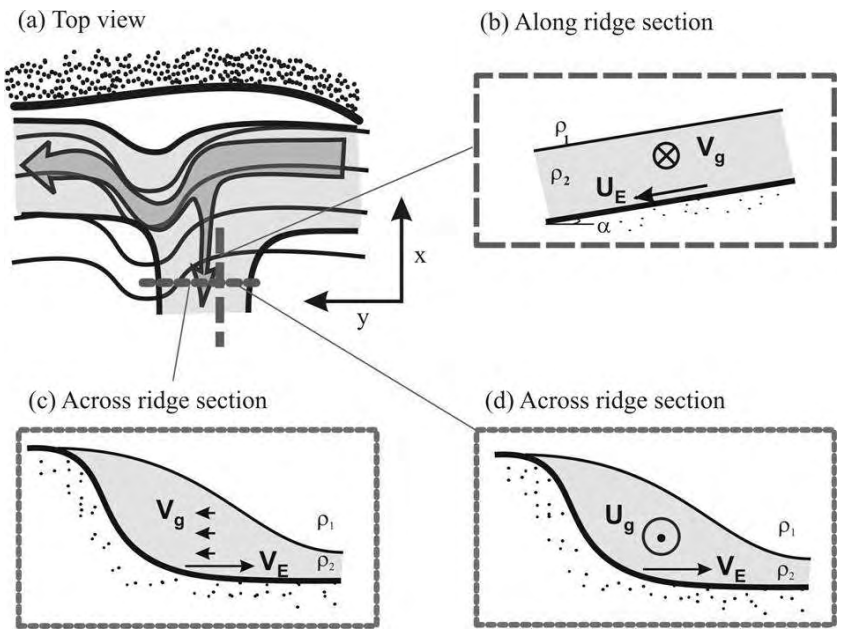

Figure 1: *a) Sketch of a dense water mass flowing downslope leaning against a submarine ridge in the northern hemisphere. Notations used in the text have been included. b) Transect parallel to the ridge showing the sloping interface supporting a geostrophic flow towards the ridge. The induced Ekman flow is directed downslope. c) Transect across the ridge, showing the sloping interface supporting a downslope geostrophic flow. The induced Ekman flow is directed away from the ridge. d) Transect across the ridge with the flows in this direction: the geostrophic flow from (b) and the Ekman flow from (c). For (9) to be fulfilled, these flows must balance*

and

$$v(x,y) = \frac{1}{h} \int_{D}^{D+h} V(x,y,z)dz \tag{4}$$

where (U, V) are the horizontal velocities at each point.

Combining (1) and (2) gives

$$hu = \theta(h) \cdot (hu_g - \delta v_g) \tag{5}$$

and

$$hv = \theta(h) \cdot (hv_g + \delta u_g) \tag{6}$$

where $\theta(h) = h^2/(h^2 + \delta^2)$, $u_g = -g'/f \cdot (h_y + D_y)$, $v_g = g'/f \cdot (h_x + D_x)$ and $\delta = K/f$.

Now let the topography be given by

$$D(x,y) = sx + d(y) \tag{7}$$

where $d(y)$ is a topographical feature, e.g. a ridge or canyon, intersecting an otherwise constantly sloping shelf. The constant slope parameter is $s = sin\alpha$, where α is the shelf slope angle (see Fig. 1b).

Assume now that

$$\frac{\partial h}{\partial x} = 0 \tag{8}$$

i.e. $v_g = \frac{g's}{f}$ and transports and velocities do not vary along the ridge. It is not expected that (8) holds in the transition region where the down-ridge flow branches off from the main current. By making assumption (8) the analysis is restricted to the region downstream of the transition region. In the transition region (8) is approached asymptotically with x as excess fluid is sliced off and advected away along the depth contours, as sketched in Fig. 1a. Below the transition zone the along-ridge transport does not vary with x, and continuity hence requires that there is no net transport into or out of the ridge region, i.e.

$$hv = 0 \tag{9}$$

or

$$\theta(h) \cdot (hv_g + \delta u_g) = 0. \tag{10}$$

Although the total cross-ridge transport hv, where v is given by the integral (4), vanishes, there is a transverse secondary circulation present in the current, i.e. $V(x,y,z)$ is non-zero and varies with z. The secondary circulation is shown and explained in Fig 1b-d and consists of a frictionally induced flow towards the right (looking upstream) close to the bottom, and a return flow towards the left in the interior. Fluid hence moves between the layers through Ekman pumping. Equations (9) and (10) require that these flows are in balance.

For $h \gg \delta$ (10) describes a leftward Ekman transport confined to a relatively thin layer δ next to the bottom and a comparatively slow return flow in the interior. The function $\theta(h)$ takes into account the regions where $h \approx \delta$ or $h < \delta$, in which case $\theta(h)$ is smaller than one and the frictional transport as well as the return flow are smaller than that given by ordinary Ekman theory.

Equation (10) has one trivial solution ($h = 0$) and one non-trivial solution, for which

$$hv_g + \delta u_g = 0. \tag{11}$$

The solution to 11 is valid wherever $0 < h < \infty$. If the layer thickness decreases to zero the trivial solution to (10) is satisfied and the thickness does not decrease further, i.e. h never becomes negative although the solution to (11) may be negative locally. Equation (11) can, after division by g'/f, be written as

$$h_y = \frac{hs}{\delta} - D_y, \tag{12}$$

which has solutions

$$h = Ce^{\frac{s}{\delta}y} + h_P \tag{13}$$

where h_P is a function of D_y. If $D_y = 0$ everywhere then $h_P = 0$ and the solutions to (12) increase exponentially with y. The only solution that does not approach infinity as $y \to \infty$ is the trivial solution $C = h = 0$. However, if $D_y \neq 0$, there are non-trivial solutions to (12) associated with a flow down the slope. Equation (12) requires one boundary condition, for example, that the layer thickness is known at one location, or that the downslope transport is quantified - which is more realizable in reality.

The geostrophic part of the downslope transport T_{down} can be found by horizontal integration along the slope,

$$T_{down} = -\int_{-\infty}^{\infty} hu_g dy. \tag{14}$$

We now introduce the dimensionless quantities $\hat{y}$, $\hat{h}$, $\hat{D}$, $\hat{u}$, $\hat{T}$, and γ, defined as

$$\begin{aligned} y &= \hat{y} \cdot W \\ h &= \hat{h} \cdot H \\ D &= \hat{D} \cdot H \\ u_g &= \hat{u} \cdot \tfrac{g'H}{fW} \\ T_{down} &= \hat{T}\tfrac{g'}{f}H^2 \\ \gamma &= \tfrac{sW}{\delta} \end{aligned} \tag{15}$$

where W is the width of the ridge, H its height, g' the reduced gravity and f the Coriolis parameter. The slope parameter s and the Ekman layer thickness δ are given as before. Introducing the non-dimensional parameters in (12) and dividing by H/W gives

$$\hat{h}_{\hat{y}} = \gamma\hat{h} - \hat{D}_{\hat{y}} \tag{16}$$

and so $\hat{h} = \hat{h}(\gamma, \hat{y})$, i.e. only a function of $\hat{y}$ and γ. The dimensionless transport $\hat{T}$ is given by

$$\hat{T}_{down} = -\int_{-\infty}^{\infty} \hat{h}\hat{u}d\hat{y} \tag{17}$$

and hence $\hat{T}_{down} = \hat{T}(\gamma)$, i.e. only a function of γ .

As seen from (16) and (17), γ is a key parameter, and the solutions are even self-similar for a given value of γ. The number expresses the ratio of the scales for the two parts of the secondary circulation: the Ekman transport δu_g and the return flow hv_g. By scaling $u_g \sim \frac{g'H}{fW}$,$v_g \sim \frac{g's}{f}$, and $h \sim H$ it is seen that

$$\frac{hv_g}{\delta u_g} \sim \gamma \tag{18}$$

Hence γ may be interpreted as the ratio of the transverse circulations if the interface slope is replaced with the slope of the ridge wall. The actual slope of the dense interface thus scales as $\gamma \times$ 'slope of the ridge wall', since the actual transports must be equal as stated in (10).

Equation (16) will now be solved for five different ridge geometries. Firstly, a step-shaped ridge is considered, followed by a discussion of the appropriate boundary condition. Secondly, four additional idealized topographies are considered, namely (ii) cosine-shaped ridge (iii) parabolic ridge (iv) linear ridge, and finally (v) a smooth ridge. As will be seen, the obtained solutions are rather similar.

(i) Step-shaped Ridge

Assume that the topography is given by

$$\hat{D}(x,y) = \begin{cases} sx & \hat{y} < 0 \\ sx+1 & \hat{y} \geq 0 \end{cases} . \tag{19}$$

Equation (16) then has non-trivial solutions

$$\hat{h}(\hat{y}) = C \cdot e^{\gamma\hat{y}}. \tag{20}$$

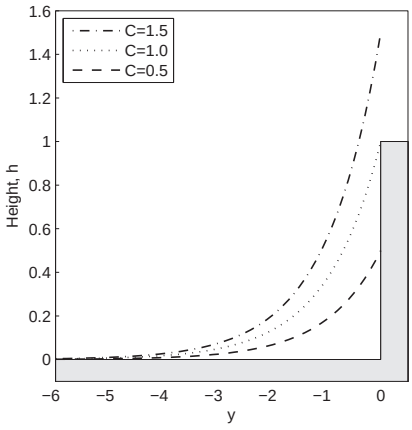

Figure 2: *Dimensionless interface $\hat{h} + \hat{D}$ as a function of $\hat{y}$ for different values of the constant C, and $\gamma = 1$. Shaded area indicates the step shaped bottom topography (looking seaward down along the ridge).*

Fig. 2 shows the layer thickness as a function of $\hat{y}$ for different values of the constant C. In order for (20) to be a physical solution it is required that

$$0 \leq C \leq 1, \tag{21}$$

since $C < 0$ gives negative solutions and $C > 1$ gives unbounded solutions, as the ridge is not intersected. For C fulfilling (21) the ridge is intersected at $\hat{y} = 0$, and (10) is trivially satisfied ($\hat{h} = 0$) for $\hat{y} \geq 0$. The solution is thus

$$\hat{h}(\gamma, \hat{y}) = \begin{cases} Ce^{\gamma \hat{y}} & \hat{y} < 0 \\ 0 & \hat{y} \geq 0 \end{cases} . \tag{22}$$

The downslope transport of the flow leaning against the ridge is, using (17), given by

$$\hat{T}_{Step} = \frac{C^2}{2}, \tag{23}$$

and hence the maximum transport for the step ridge is achieved for $C = 1$. Inserting $C = 1$ in (23) gives $\hat{T}_{Step} = \frac{1}{2}$, regardless of the values of the parameters s, W and δ. Maximal transport is consequently obtained for

$$C = \max \{C_{physical}\} \tag{24}$$

for which $\hat{h}(0) = 0$ and $\hat{h} > 0$ for $\hat{y} < 0$.

From now on, and for the other ridge geometries, the boundary condition giving the maximal geostrophic downslope transport will be used, and the obtained (maximal) transport will be referred to as the transport capacity of the ridge.

(ii) Cosine-shaped Ridge

Assume that the topography is given by

$$\hat{D}(x,y) = \begin{cases} sx & \hat{y} \le -1 \\ sx + \frac{1}{2}\left[\cos\left(\pi\hat{y}\right) + 1\right] & \hat{y} > -1 \end{cases} . \tag{25}$$

Using the requirement of maximal downslope transport, i.e. $\hat{h}(0) = 0$ and $\hat{h} > 0$ for $\hat{y} < 0$, the solution to (16) using (25) is given by

$$\hat{h}(\gamma,\hat{y}) = \begin{cases} \frac{\pi^2}{2(\pi^2+\gamma^2)}\left(1+e^{\gamma}\right)e^{\gamma\hat{y}} & \hat{y} \le -1 \\ \frac{\pi^2}{2(\pi^2+\gamma^2)}\left[e^{\gamma\hat{y}} - \cos(\pi\hat{y}) - \frac{\gamma}{\pi}\sin(\pi\hat{y})\right] & -1 < \hat{y} < 0 \\ 0 & \hat{y} \ge 0 \end{cases} . \tag{26}$$

Using (17), the downslope transport is given by

$$\hat{T}_{COS}(\gamma) = \frac{\pi^2}{4}\left[\frac{\pi^2(1+e^{-\gamma})}{(\pi^2+\gamma^2)^2} + \frac{\gamma}{2(\pi^2+\gamma^2)}\right]. \tag{27}$$

As $\gamma \to 0$ the transport approaches 0.5,

$$\lim_{\gamma\to 0}\ \hat{T}_{COS} = \frac{1}{2}. \tag{28}$$

Hence for small γ the cosine ridge transport approaches the step ridge transport.

(iii) Parabolic ridge

Assume that the topography is given by

$$\hat{D}(x,\hat{y}) = \begin{cases} sx & \hat{y} \le -1 \\ sx + 1 - \hat{y}^2 & \hat{y} > -1 \end{cases} . \tag{29}$$

Using the requirement of maximal downslope transport, i.e. $\hat{h}(0) = 0$ and $\hat{h} > 0$ for $\hat{y} < 0$, the solution to (16) using (29) is given by

$$\hat{h}(\gamma,\hat{y}) = \begin{cases} \left(\frac{2}{\gamma^2}\left[\gamma e^{\gamma} - e^{\gamma} + 1\right]\right) e^{\gamma\hat{y}} & \hat{y} \le -1 \\ \frac{2}{\gamma^2}\left(e^{\gamma\hat{y}} - \gamma\hat{y} - 1\right) & -1 < \hat{y} < 0 \\ 0 & \hat{y} \ge 0 \end{cases} . \tag{30}$$

Using (17), the downslope transport is given by

$$\hat{T}_{PB}(\gamma) = \frac{2}{\gamma^4}\left[2 - \gamma^2 + \frac{2\gamma^3}{3} - 2e^{-\gamma}(\gamma+1)\right]. \tag{31}$$

Using l'Hôpital's rule repeatedly it is seen that the transport approaches the value 0.5 for small γ,

$$\lim_{\gamma\to 0} \hat{T}_{PB} = \frac{1}{2}. \tag{32}$$

Hence, also the parabolic ridge transport approaches the step function transport for small γ.

(iv) Linear Ridge

Assume that the topography is given by

$$\hat{D}(x,\hat{y}) = \begin{cases} sx & \hat{y} \le -1 \\ sx + \hat{y} + 1 & -1 < \hat{y} < 0 \\ sx + 1 & \hat{y} \ge 0 \end{cases} . \tag{33}$$

Using the requirement of maximal downslope transport, i.e. $\hat{h}(0) = 0$ and $\hat{h} > 0$ for $\hat{y} < 0$, the solution to (16) using (33) is given by

$$\hat{h}(\gamma,\hat{y}) = \begin{cases} \left(\frac{1}{\gamma}\left[e^{-\gamma} - 1\right]\right) e^{\gamma\hat{y}} & \hat{y} \le -1 \\ \frac{1}{\gamma}\left(1 - e^{\gamma\hat{y}}\right) & -1 < \hat{y} < 0 \\ 0 & \hat{y} \ge 0 \end{cases} . \tag{34}$$

Using (17), the downslope transport is given by

$$\hat{T}_{LIN}(\gamma) = \frac{1}{\gamma^2}\left[\gamma - 1 + e^{-\gamma}\right]. \tag{35}$$

By serial expansion of (35) around $\gamma = 0$ it can be seen that

$$\lim_{\gamma\to 0} \hat{T}_{LIN} = \frac{1}{2}. \tag{36}$$

Hence, also the linear ridge transport approaches the step function transport for small γ.

(v) Smooth ridge

Assume that the topography is given by

$$\hat{D}(x,\hat{y}) = sx + \frac{1}{1+\hat{y}^2}. \tag{37}$$

Using the requirement of maximal downslope transport, i.e. $\hat{h}(0) = 0$ and $\hat{h} > 0$ for $\hat{y} < 0$, the solution to (16) using (37) is given by (See Appendix A for derivation)

$$\hat{h}(\hat{y},\gamma) = \begin{cases} \frac{-1}{1+\hat{y}^2} + \frac{i\gamma}{2}e^{\gamma(\hat{y}+i)}Ei(\gamma(\hat{y}+i)) - \frac{i\gamma}{2}e^{\gamma(\hat{y}-i)}Ei(\gamma(\hat{y}-i)) + \\ +e^{\gamma\hat{y}}\left[1 - \frac{i\gamma}{2}e^{i\gamma}Ei(\gamma i) + \frac{i\gamma}{2}e^{-i\gamma}Ei(-\gamma i)\right] & \hat{y} \geq 0 \\ 0 & \hat{y} < 0 \end{cases} \tag{38}$$

where $Ei(x) = \int_0^\infty \frac{e^{-xt}}{t}dt$. The downslope transport is calculated numerically from the integral

$$\hat{T}(\gamma) = -\int_{-\infty}^{0} h\frac{\partial D}{\partial y}dy \tag{39}$$

where $h(0^+) = h(-\infty) = 0$ has been used.

The present theory requires that the inertial terms are small compared with the Coriolis term, i.e. that the Rossby number $\varepsilon = \frac{U}{fW}$ is small. By using the geostrophic velocity scaling $U = \frac{g'H}{fW}$ and inserting into the Rossby number it is seen that provided the Burger number $B = g'H/(f^2W^2)$ is small, it also follows that $\varepsilon \ll 1$. Thus it is expected that for currents that are wide compared to the Rossby radius, i. e. currents for which $B \ll 1$, the inertial terms should be negligible compared to the Coriolis term, or $\partial u/\partial y \ll f$. For large γ, the solutions are thin layers with comparatively large curvature of the upper surface, and hence $\partial u/\partial y$ may become comparable to f even though $B \ll 1$. This happens when the dimensionless derivative $\partial\hat{u}/\partial\hat{y}$ becomes large compared to one. The step-shaped ridge has a maximum value, $\partial\hat{u}/\partial\hat{y}|_{MAX} = \gamma^2$, at $\hat{y} = 0$. Hence for $\gamma \gg 1$ we have that $\partial u/\partial y \ll f$ provided $B\gamma^2 << 1$, or

$$\frac{s^2 g'H}{f^2\delta^2} << 1. \tag{40}$$

3 Results

Fig. 3 shows the non-dimensional interface height for the five ridges considered in the previous section. The solutions are shown for three values of the parameter $\gamma = \frac{sW}{\delta}$ (0.1, 1, and 10), and as can be seen all ridge geometries give similar solutions, with large (small) γ

giving thin (thick) layers. All solutions decrease exponentially with $\gamma\hat{y}$.

Fig. 4 shows the dimensionless velocity $\hat{u}$ as a function of γ. The velocity profiles have a local maximum in the ridge break area (at $\hat{y} = 0$ for the step ridge and around $\hat{y} \sim -1$ for the other ridges) where the ridge rises up from the slope. The magnitude of the velocity depends on γ , with large values of γ giving large velocities.

From Fig. 3 it is seen that the dense core is wide compared to the ridge for small γ and more narrow for large γ. Hence, a ridge on a steep shelf slope, which has comparatively large s and γ, is expected to have a relatively fast downslope flow that is localized in the vicinity of the ridge and decays rapidly away from it. In cases with small γ, e.g. on a shallow slope or in regions of enhanced bottom friction, the dense water that leans against the ridge will flow more slowly and occupy a larger area upstream of the ridge.

It was shown in the previous section that for a given ridge shape, the dimensionless transport capacity, $\hat{T}$, depends only on γ. Fig. 5 shows $\hat{T}$ as a function of γ for the five topographies. As expected from the similar velocity- and thickness distributions among the other ridges these also have comparable transport capacities. For the step ridge, the dependencies of velocity and thickness on γ cancel out, and the downslope transport capacity is independent of γ. In the limit of zero width, i.e. as γ approaches zero, the transport capacity for all the considered ridges approaches the value 0.5 pertaining to the step-shaped ridge. For larger γ the transport capacity decreases. This means that the downslope steering is most effective for gentle bottom slopes that are intersected by sharp ridges, and/or in regions of enhanced bottom friction. However, the downslope transport can never exceed the theoretical maximum value $1/2$, obtained for the step-shaped ridge or in the limit $\gamma \to 0$. According to (15), the dimensional transport capacity is obtained by multiplying $\hat{T}$ by $g'H^2/f$, and so the maximal capacity is $g'H^2/(2f)$.

For comparison, the downslope transport obtained for a cosine-shaped canyon (Wåhlin 2002) and that for a linear canyon (Davies et al. 2006) have been inserted in Fig. 5 (see Appendix B for derivation). The transport capacity for the canyon geometries approaches zero for small γ, while all ridge geometries approach 0.5 as discussed above. It is hence expected that for abrupt topography and/or small seaward slopes of the bottom, ridges steer dense water downhill more effectively than canyons. For $\gamma < 0.1$, the transport capacity of a ridge is more than an order of magnitude larger than that of a canyon. The reason for this difference is that for small γ, the downslope ridge flow is comparatively slow but occupies a wide section next to the ridge. The canyons have a similar behavior for small γ, with comparatively slow and thick canyon-flows. However, since the flow is laterally confined by the canyon walls, the flow cannot become as wide as that associated with the ridge, and the downslope transport is limited.

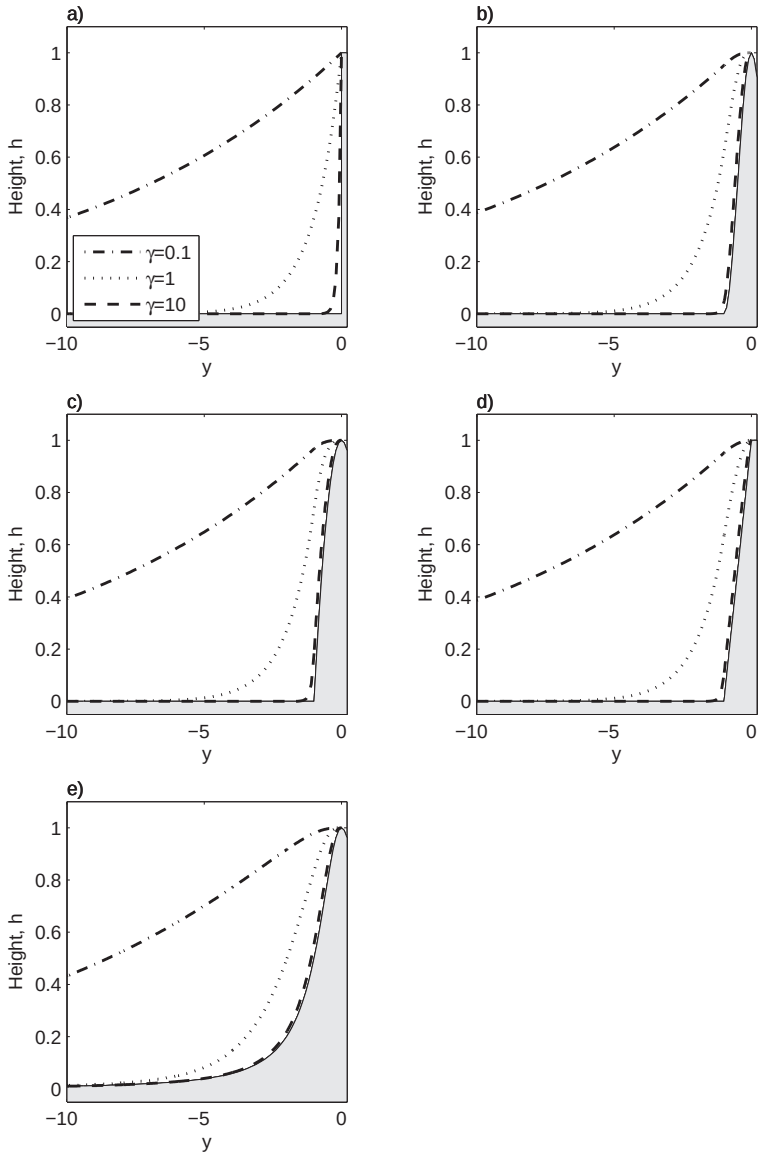

Figure 3: *Dimensionless interface $\hat{h}+\hat{D}$ as a function of $\hat{y}$ for different topographies. Shaded area indicates bottom topography (looking seaward down along the ridge) while the lines are $\hat{h}+\hat{D}$ for different values of γ according to legend. a) Step-shaped ridge, b) cosine-shaped ridge, c) parabolic ridge, d) linear ridge, and e) smooth ridge.*

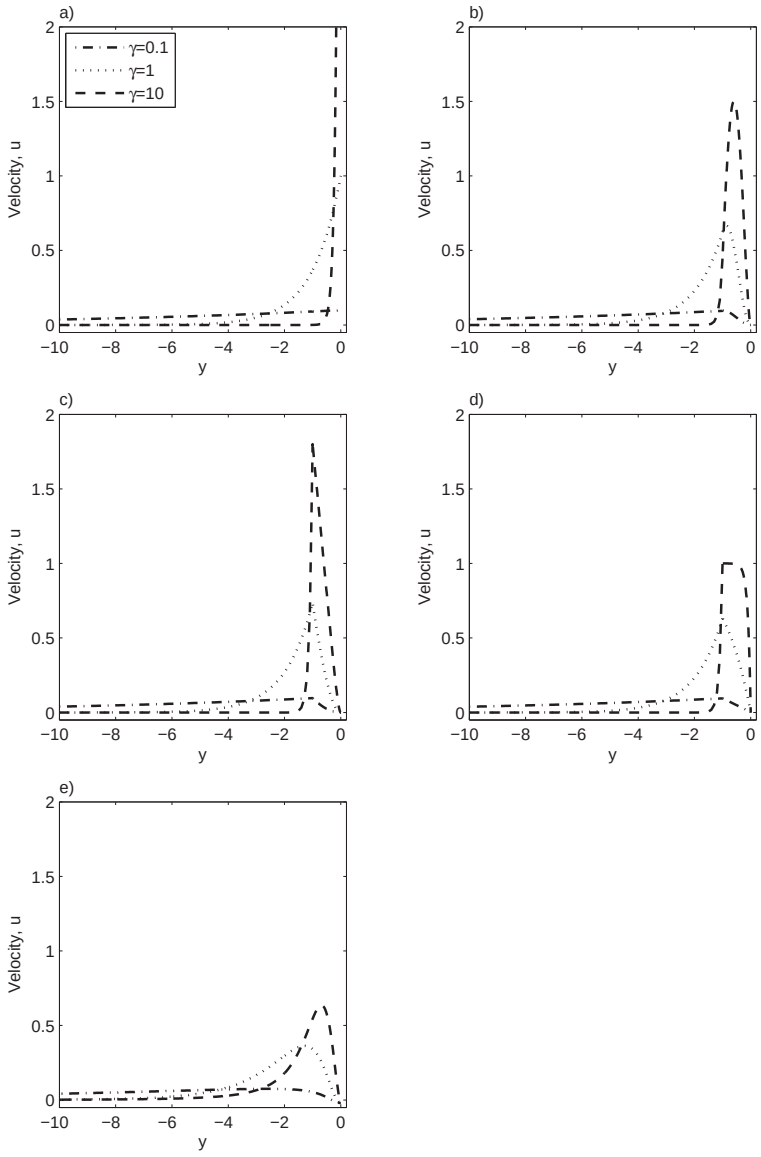

Figure 4: *Dimensionless velocity* $\hat{u} = u\frac{fW}{g'H}$ *as a function of* $\hat{y}$ *for different topographies. The lines show for different values of* γ *according to legend. a) Step-shaped ridge, b) cosine-shaped ridge, c) parabolic ridge, d) linear ridge, and e) smooth ridge.*

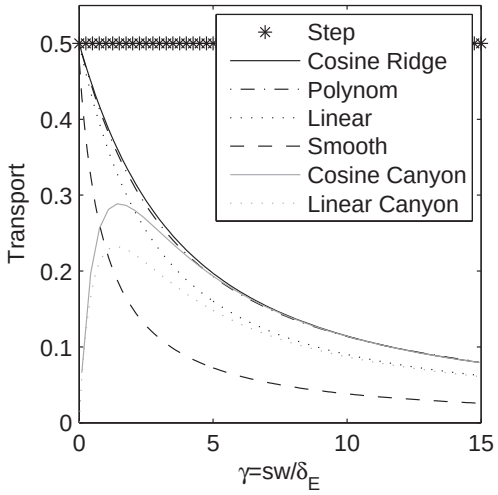

Figure 5: *Geostrophic downslope transport as a function of the topographic parameter* $\gamma = sW/\delta$ *for flow leaning against a ridge. The black lines correspond to the different ridge-shapes according to legend. The grey lines indicate the transport in a cosine-shaped and a linear canyon and have been inserted for comparison.*

4 Topographic steering of the Filchner Overflow

Cold Ice Shelf Water (ISW) is formed under the Filchner-Ronne Ice Shelf as sea water interacts with the floating glacial ice (Nøst & Foldvik 1994). Fig. 6a shows how ISW ($T < -1.9°$C, $S \simeq 34.60$) exits the ice shelf cavity through the Filchner Depression, passing over the sill onto the continental slope. There it flows left along the topography as a plume of dense water (Foldvik et al. 2004) submerging the warmer (T $\simeq 0°$ C) and slightly more saline (S $\simeq$ 34.66) Weddel Deep Water (WDW). Foldvik et al. (2004) estimated the flux of ISW to be 1.6 ± 0.5 Sv.

The continental slope in the area has slopes ranging from 0.03 at the upper part of the slope to 0.015 further down. Fig. 6b shows the topography and the mean current measured by five moorings (located 10-56 m above the bottom). Moorings F1-F4 revealed a mean flow of dense, cold water roughly aligned with the isobaths. Such a flow field is typical for the region as is evident from the present data as well as several other current meter moorings, all of which were presented in detail in Foldvik et al. (2004). Some 80 km west of the Filchner Depression the slope is crosscut by a system of submarine canyons and ridges. Mooring D1 (see Fig. 6b) was placed in the vicinity of the eastern-most of these ridges, and contrary to the other moorings in the plume, it indicates a flow aligned with the ridge, i.e. across the isobaths and down the slope. Fig. 7 shows a CTD section across the ridge and the D1

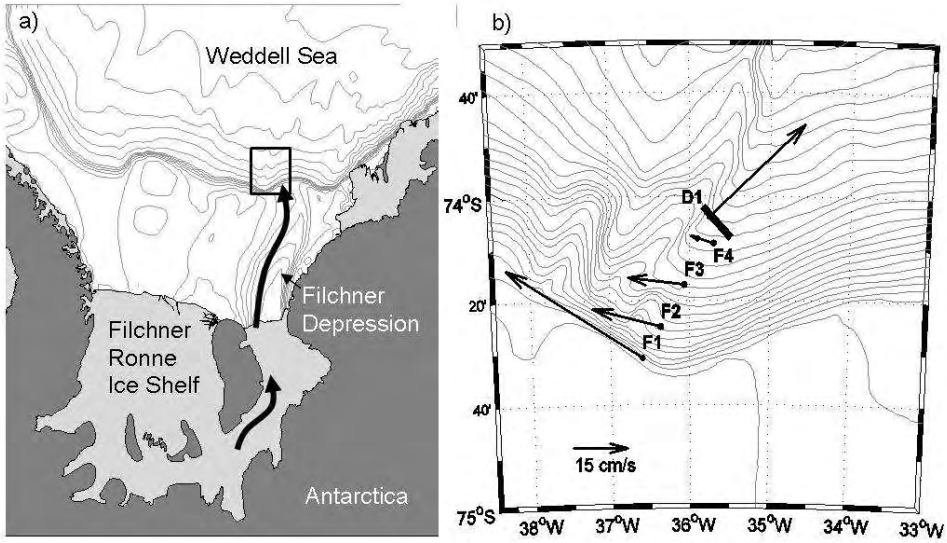

Figure 6: *The study area. a) The western Weddell Sea with floating ice shelves in light grey and the Antarctic continent in dark grey. The thick arrows indicate the approximate pathway of cold Ice Shelf Water (ISW) exiting the Filchner-Ronne Ice Shelf cavity. The black box marks the close-up shown in (b). The map was created using data from the Antarctic Digital Database (SCAAR 2006). b) Position and mean current (instrument closest to the bottom, i.e. 10/10/56 and 10 m above bottom respectively) of moorings in the Filchner Overflow area. The black line marks the position of the CTD section showed in Fig. 7.*

mooring. Plume water, here indicated by the $-0.6°$C isotherm, is seen as an approximately 170 m thick layer leaning against the ridge. A thin layer of plume water can also be observed on the ridge.

The D1 mooring was deployed on the slope at a depth of 2100 m in January 1985 and was recovered a year later, in January 1986. The mooring was equipped with two current meters, Anderaa RCM, that were placed 25 and 100 m above the bottom and registered hourly values of velocity and temperature. The data records show a mean northeasterly current and a strong six-day oscillation that is aligned with the mean flow and has an amplitude roughly equal to the mean speed (Darelius et al. 2006). The same oscillation is seen in the temperature record, swinging between $0°$C and $-1.9°$C. Thus, throughout the oscillation period the mooring is surrounded by Weddell Deep Water (WDW), ISW and mixtures thereof. Fig. 8 shows the along-ridge velocity plotted against the temperature, and

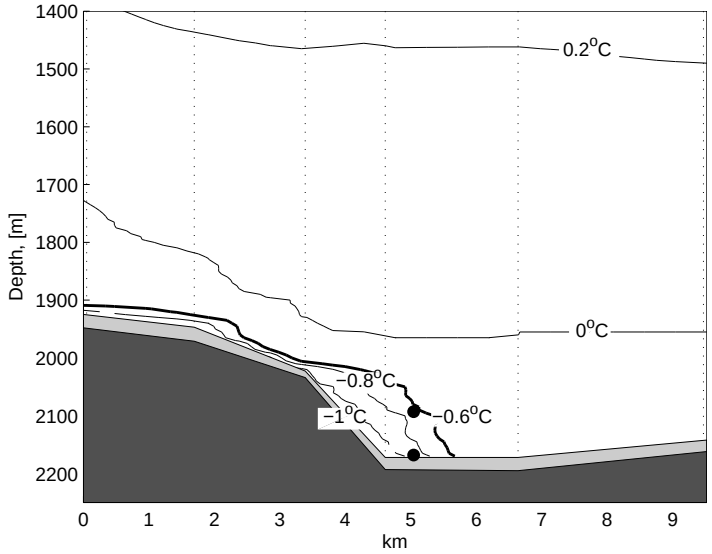

Figure 7: *CTD section across the ridge along the line indicated in Fig. 6. Dotted lines indicate the CTD stations while solid lines are isotherms. Light grey indicates area below CTD casts, i.e. with no data. The D1 moorings are indicated with black circles.*

a strong negative correlation (r = -0.75) is apparent. The correlation indicates a pulsating flow, where quiescent periods, during which the mooring is submerged in warm WDW, are interrupted by dynamic episodes or pulses of cold ISW or ISW/WDW mixtures flowing by the mooring at high speeds (up to 1 m/s). Despite the fluctuating nature of the flow, the temporal Rossby number is small (using the maximal velocity 1 m/s and a period of six days gives a Rossby number of 0.02), and the flow is expected to be quasi-geostrophic.

The CTD-section in Fig. 7 shows an approximately 170 m thick dense layer. The two temperature sensors at mooring D1 do not provide information about the dense layer thickness and its fluctuations. However, since the uppermost record is co-oscillating with the lower one and the temperature difference between them is only a few tenths of a degree, it is hypothesized that the two sensors were both within the dense layer and hence that this was at least 100 m thick at the site of the mooring.

The theory presented in the preceding sections predicts layer thickness, velocities and transports given the background slope, the Ekman layer thickness and the properties of the ridge and the two water masses. We can estimate the geometrical constants from the map in Fig. 6b and have $H \simeq 300$ m, $W \simeq 7$ km, and $s \simeq 0.02$. The mooring is located roughly 6

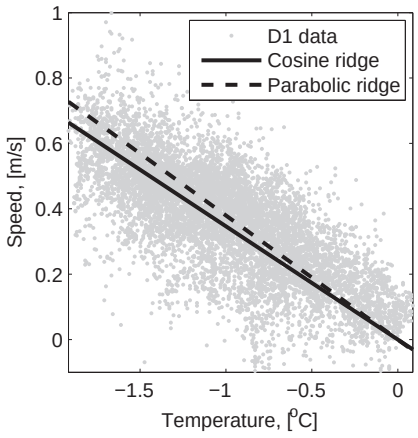

Figure 8: *: Along-ridge velocity versus temperature from mooring D1, 25 m above bottom. The lines show the relation between velocity and temperature according to (44), for a cosine and parabolic ridge shape.*

km east of the top of the ridge, and so $y \simeq 6$ km. Using a quadratic friction law the Ekman layer thickness, δ, can be estimated by (see e.g. Wåhlin & Walin (2001) for a comparison of linear and quadratic parameterizations of bottom friction)

$$\delta = (C_D + E)\frac{g' \sin\phi}{f^2} \tag{41}$$

where C_D is the drag coefficient, E the entrainment coefficient and ϕ the slope of the ridge side. Measurements from the Faroe Bank Overflow made by Mauritzen et al. (2005) gave a C_D of 4×10^{-3} and showed that the interfacial stress was relatively small. Assuming that the conditions in the Filchner Overflow are somewhat similar (i.e. $C_D = 4 \times 10^{-3}$, $E = 0$) and that $tan\phi \simeq H/W$ gives $\delta = 35$ m. Combining the values from above gives $\gamma = 4$ which corresponds to a non-dimensional transport capacity of around 0.25 (see Fig. 5). Returning to the dimensional expressions (using (10)) and assuming that the layer consists of undiluted ISW, we get a transport capacity of roughly 0.3 Sv. The total flow of ISW was estimated to be 1.6 Sv by (Foldvik et al. 2004), and hence, according to the present calculations, the ridge could support a downslope transport equivalent to one fifth, a substantial part, of the total outflow.

Fig. 9 shows the analytical solutions when the parameter values specified above are applied to a cosine-shaped and a parabolic ridge. The instruments on mooring D1 are marked with asterisks. According to the theory the dense layer should be roughly 100 m thick at the site of the mooring, somewhat thinner than what is obtained from the CTD

data. The thickness decreases relatively fast, and 5 km west of the ridge break the thickness is less than 10 m. The easternmost stations in the CTD section (Fig. 7) are located roughly 3 and 6 km east of the ridge. At those stations the CTD, which was lowered to 15-20 m above the bottom, did not detect a dense layer, and so the lateral extent of the dense layer seems to agree well with the theoretical prediction.

One result of the present theory is that the shape and slope of the dense interface are independent of the density difference and the geostrophic velocity. Provided the along-slope transport exceeds the transport capacity of the ridge, the plume shape depends only on the topography (although the magnitude of the transport depends on the density difference and associated geostrophic velocity). The strong correlation between velocity and temperature that is evident in Fig. 8 supports this result. If the plume shape varied during the measurement period, the relation between velocity and density difference would not be linear, as it appears to be.

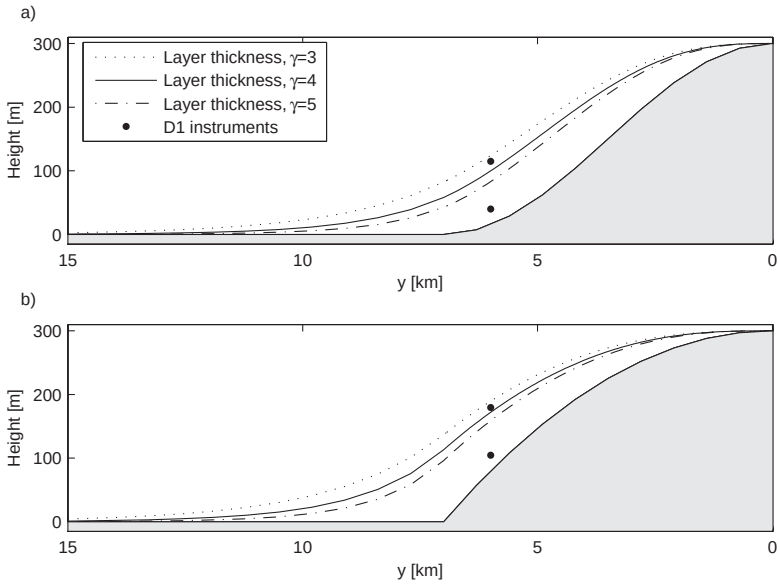

Figure 9: *Theoretical layer thickness obtained using observed constants and idealized a) cosine-shaped and b) parabolic ridge topographies. Lines show theoretical interface level based on three different values of the topographic parameter* $\gamma = sW/\delta$ *, according to legend. The position of the D1 mooring and its instruments are indicated with asterisks.*

Ignoring the small changes in salinity we can express the density difference $\Delta\rho$ as

$$\Delta\rho = -\alpha\,\Delta T\,\rho_0 \tag{42}$$

where α is the thermal expansion coefficient, $\Delta T = T - T_0$, and T_0 (ρ_0) is a reference temperature (density). The geostrophic velocity at the site of the mooring ($y = y^*$) can hence be expressed as

$$u_g(y^*) = -\frac{g\alpha\Delta T}{f}\left.\frac{\partial(h+D)}{\partial y}\right|_{y=y^*} \tag{43}$$

where $\left.\frac{\partial(h+D)}{\partial y}\right|_{y=y^*}$ is the slope of the interface at $y = y^*$, which according to theory does not change in time even though ΔT may do so. Using the geometrical constants above gives $\left.\frac{\partial(h+D)}{\partial y}\right|_{y=y^*} = 0.05$ for a cosine-shaped ridge and $\left.\frac{\partial(h+D)}{\partial y}\right|_{y=y^*} = 0.06$ for a parabolic ridge. The thermal expansion coefficient α is at 2000 m $(8.34/10.58) \times 10^{-5}$ K^{-1} for $T = -2/0^\circ$C respectively (Gill 1982). Using the mean value $\alpha = 9.5 \times 10^{-5}$K^{-1}, $f = 1.3 \times 10^{-4}$ s^{-1}, $g = 9.82$ m/s^2 and the interface slope (43) gives

$$u_g(y^*) = -k\Delta T(y^*) \tag{44}$$

where $k = 0.34$ for a cosine-shaped ridge and $k = 0.38$ for a parabolic ridge. The linear relations corresponding to these two values have been inserted in Fig. 8, and, as can be seen, the agreement is not unreasonable considering the simplifications involved.

5 Discussion

Dense plumes of sufficiently large scale are geostrophic to leading order, and they hence flow nearly parallel to the isobaths on a slope. The descent of dense water is due either to ageostrophic processes, such as friction or eddies, or to topographical steering. Previous studies on topographic steering have focused on the downslope flow that takes place in submarine canyons or depressions (Sherwin et al. 2007, Sherwin & Turrell 2005, Vilibic et al. 2004, Wåhlin 2002). It was, however, shown in the numerical experiments by Jiang & Garwood (1998) that elevations as well as depressions intersecting the slope can be associated with downslope flow of the dense water. In the present study it is shown that the dynamical regime allowing frictionally modified geostrophic flow down a canyon can be established also along a ridge. For abrupt topography, and/or comparatively small background slopes, ridges are in fact more effective than canyons in channeling dense water down the slope, since the width of the flow in the canyon is limited by the canyon walls. Consider, for example, a continental slope where the bottom slopes seaward with the ratio 1/100, and where the thickness of the Ekman layer (δ) is 50 m. If this slope is intersected by a topographic irregularity - ridge or canyon - which is 5 km wide, then the topographic parameter $\gamma = sW/\delta$ is equal to one. From Fig. 5 we have that a ridge should channel nearly twice as much water down the slope as a canyon. If the slope instead is 0.005, then $\gamma = 0.5$

and the ridge is three times as effective.

The non-dimensionalized transport capacity for a given ridge shape is a function only of $\gamma = sW/\delta$. The geometrical number γ can be interpreted as the ratio of the scaled transports if the interface slope is replaced with the slope of the ridge wall. As $\gamma \to 0$, i.e. for steep ridges and/or small background slope, the transport capacity for all ridge topographies approaches the maximum value 1/2. The actual magnitude of the downslope transport, T, depends also on the ridge height H, the reduced gravity g' and the Coriolis parameter f and is given by $T = \hat{T}(\gamma)\frac{g'}{f}H^2$, where $\hat{T}(\gamma)$ is found from the analytical expressions plotted in Fig. 5. The expressions all pertain to a linear bulk friction parameterization, but according to canyon calculations (Wåhlin 2002) the results are expected to be similar also for a quadratic friction parameterization provided the Ekman layer thickness is equal.

The obtained solutions are comparatively insensitive to the shape of the ridge, as indicated by the similarity in the results for the presented ridge topographies. This means that a first-order estimation of the transport capacity can be done without detailed information on the ridge topography.

As discussed, the transport capacity is the maximum downslope flux of dense water that a ridge/canyon can support. This suggests that if the flow approaching a ridge is smaller than its transport capacity, all of the water may be channeled downslope. If, however, the along-slope transport upstream of the ridge is increased and the transport capacity is exceeded, the flow will divide in two, with the excess fluid passing over the ridge and continuing along the slope. This process can explain the division of the Filchner Overflow plume that was observed by Foldvik et al. (2004): the estimated transport capacity of the examined ridge is 0.3 Sv while the total flux of ISW is 1.6 Sv (Foldvik et al. 2004). The numerical experiments conducted by Jiang & Garwood (1998) show a tendency to this mechanism. They used a large and a small ridge, both of which induced a division of the flow. Applying the present theory to their geometry gives a transport capacity that is comparable to, but smaller, than their initial outflow rate; but it seems likely that by the time the dense water reached the ridge, its transport had been increased by entrainment.

Entrainment and detrainment processes are clearly important to the ambient ocean stratification as they determine the final properties and penetration depth of the plume water (e.g. Legg et al. (2006)). Small-scale topographic features on the slope affect the mixing and entrainment/detrainment processes. It was noted in the model study by Jiang & Garwood (1998) that mixing in downslope flows was increased in the vicinity of a ridge and in a canyon, and Baines & Condie (1998) made the same observation in a laboratory experiment with a dense plume entering a canyon. However, when steered by a ridge or a canyon, the dense flow will follow a shorter path to the deep sea. The shorter path may outweigh the expected increase in entrainment ratio and so maintain or even increase the penetration depth. As pointed out by Hughes & Griffiths (2006), it is the rate of entrainment per unit

depth of fall that is important. Wells & Wettlaufer (2005) showed in the laboratory that for relatively steep slopes, this parameter is constant. If this holds also for gentle slopes, it would indicate that the total entrainment is constant, regardless of whether the plume descends leaning on a ridge or on the open slope.

The real bathymetry of the Weddell Sea slope is clearly more complex than the idealized ridge topographies used here, but in light of the other simplifications involved it appears pointless to go into greater bathymetric detail when comparing the data set with the theory. It has been assumed that the flow is geostrophic to leading order and that along-ridge variations of plume thickness are small compared with those across the ridge. Furthermore, the effects of mixing and thermobaricity have been neglected, and the upper layer has been assumed inactive. The dataset will here be discussed with regard to these assumptions.

It was shown in Section 4 that the velocities are quasi-steady despite the oscillating nature of the flow (Darelius et al. 2006). However, geostrophy can be modified also by the advective inertial terms, if the vorticity $\frac{\partial u}{\partial y} \approx f$. In order to have negligible inertial terms it is required that $\frac{g'H}{f^2W^2} = B \ll 1$ or, for large γ, relation (40) $B\gamma^2 \ll 1$. It is obvious that the data presented here do not satisfy either requirement. The parameters from section 4 give $B = 0.6$, $\gamma = 4$ and $B\gamma^2 = 10$, and hence advection may well play a role in the momentum balance, modifying the theory presented here. As was suggested also in Johnson & Ohlsen (1994), it is hypothesized that the secondary, transverse circulation involving the slower moving water in the Ekman Layer is likely to reduce the velocities. The transport capacity should then also be smaller than the theoretical values presented here.

The theory neglects the effect of mixing, entrainment and detrainment and is strictly valid only for flows where no such processes occur. All natural flows will, however, to some extent exchange mass and momentum with the surroundings. It is not possible from the current data set to quantify the importance of these exchanges. The high velocities suggest that the flow occasionally is supercritical, which according to lab experiments (Ellison & Turner 1959) is indicative of high mixing rates. On the other hand, the presence of almost undiluted ISW ($T \simeq -1.9^\circ$C) at the mooring shows that little entrainment has taken place.

It was suggested by Killworth (1977) that thermobaricity, or the dependence on temperature of the compressibility of seawater, has an important effect on the descent of the cold ISW [although there are also studies showing that the thermobaric effect may be counteracted by the increased mixing induced by the higher velocities (Jungclaus et al. 1995)]. The present results indicate that the corrugated topography may play an equal (and hitherto overlooked) role in the descent.

An interesting extension of the present work would be to include the effects of an active upper layer. Laboratory experiments and modeling by Kämpf (2005) show that a dense flow down a canyon may induce a barotropic counter flow in the overlying water mass. It

has also been suggested that the stretching of an active upper layer may contribute to eddy generation, a mechanism that presumably will be of increased importance in the presence of topographic corrugations. Such eddies have been observed in the laboratory (Cenedese et al. 2004, Etling et al. 2000, Lane-Serff & Baines 1998) and above the Denmark Strait Overflow (Lea et al. 2006, Høyer & Quadfasel 2001, Bruce 1995), and there are indications that similar phenomena occurs also in the Filchner region (Darelius et al. 2006).

Despite the discrepancies between the theoretical assumptions and the state in the real ocean, the presented hydrographic data from the Filchner Overflow seem to agree qualitatively with theory. It should be pointed out, however, that the data set is sparse and not very detailed and that it provides support rather than proof for the theory. A higher accuracy of transport estimates can surely be obtained by inclusion of omitted terms and more complex models.

The continental slope around Antarctica is full of ridges and corrugations, and the present findings support a large-scale conceptual model in which dense water circles around the continent, fed from above by a number of buoyancy sinks and drained by a downhill transport caused by various ageostrophic and/or topographically induced processes. The relative importance of topographic corrugations among these processes needs to be assessed, but the present findings and data indicate that they may be a responsible for a substantial part of the downslope transport.

Acknowledgements We are grateful for the careful reading of and ideas for improvements of the manuscript by P. Haugan, P. Rhines, and three anonymous reviewers and to S. Østerhus and T. Gammelsrød for providing data and enthusiastically commenting on the manuscript. AW was funded by the Swedish Research Council, which is appreciated. This is publication A158 in the Bjerknes Publication Series.

References

Ambar, I. & Howe, M. R. (1979), 'Observations of the Mediterranean Outflow.2. Deep circulation in the vicinity of the Gulf of Cadiz', *Deep-Sea Research Part A-Oceanographic Research Papers* **26**(5), 555–568.

Baines, P. G. & Condie, S. (1998), Observations and modelling of antarctic downslope flows: a review, *in* S. S. Jacobs & R. F. Weiss, eds, 'Ocean, Ice, and Atmosphere - Interaction at the Antarctic Continental Margin', Vol. 75, AGU, Washington D.C.

Bruce, J. G. (1995), 'Eddies southwest of the Denmark Strait', *Deep-Sea Research Part I-Oceanographic Research Papers* **42**(1), 13–29.

Campin, J. M. & Goosse, H. (1999), 'Parameterization of density-driven downsloping flow for a coarse-resolution ocean model in z-coordinate', *Tellus Series A - Dynamic Meteorology and Oceanography* **51**(3), 412–430.

Cenedese, C., Whitehead, J. A., Ascarelli, T. A. & Ohiwa, M. (2004), 'A dense current flowing down a sloping bottom in a rotating fluid', *Journal of Physical Oceanography* **34**(1), 188–203.

Chapman, D. C. & Gawarkiewicz, G. (1995), 'Offshore transport of dense shelf water in the presence of a submarine-canyon', *Journal of Geophysical Research-Oceans* **100**(C7), 13373–13387.

Darelius, E., Østerhus, S. & Gammelsrød, T. (2006), 'Variability of the Filchner Overflow plume', *FRISP report* (17).

Davies, P., Wåhlin, A. & Guo, Y. (2006), 'Laboratory and analytical model studies of the FBC deep water outflow', *Journal of Physical Oceanography* **36**(7), 1348–1364.

Ellison, T. H. & Turner, J. S. (1959), 'Turbulent entrainment in stratified flows', *Journal of Fluid Mechanics* **6**(3), 423–448.

Etling, D., Gelhardt, F., Schrader, U., Brennecke, F., Kuhn, G., d'Hieres, G. C. & Didelle, H. (2000), 'Experiments with density currents on a sloping bottom in a rotating fluid', *Dynamics of Atmospheres and Oceans* **31**(1-4), 139–164. Sp. Iss. SI.

Foldvik, A., Gammelsrød, T. & Tørresen, T. (1985*a*), 'Hydrographic Observations from the Weddell Sea during the Norwegian antarctic Research Expedition 1976/1977', *Polar Research* **3**, 177–193.

Foldvik, A., Gammelsrød, T. & Tørresen, T. (1985*b*), 'Physical oceanography studies in the Weddell Sea during the Norwegian antarctic Research Expedition 1978/79', *Polar Research* **3**, 195–207.

Foldvik, A., Gammelsrød, T., Østerhus, S., Fahrbach, E., Rohardt, G., Schrøder, M., Nicholls, K. W., Padman, L. & Woodgate, R. A. (2004), 'Ice shelf water overflow and bottom water formation in the southern Weddell Sea', *Journal of Geophysical Research-Oceans* **109**(C2).

Gill, A. E. (1982), *Atmosphere-Ocean Dynamics*, Academic Press, San Dieago.

Girton, J. B. & Sanford, T. B. (2003), 'Descent and modification of the overflow plume in the Denmark Strait', *Journal of Physical Oceanography* **33**(7), 1351–1364.

Hughes, G. O. & Griffiths, R. W. (2006), 'A simple convective model of the global overturning circulation, including effects of entrainment into sinking regions', *Ocean Modelling* **12**, 46–97.

Høyer, J. L. & Quadfasel, D. (2001), 'Detection of deep overflows with satellite altimetry', *Geophysical Research Letters* **28**(8), 1611–1614.

Jiang, L. & Garwood, R. W. (1998), 'Effects of topographic steering and ambient stratification on overflows on continental slopes: a model study', *Journal of Geophysical Research-Oceans* **103**(C3), 5459–5476.

Johnson, G. C. & Ohlsen, D. R. (1994), 'Frictionally modified rotating hydraulic channel exchange and ocean outflows', *Journal of Physical Oceanography* **24**(1), 66–78.

Jungclaus, J. H., Backhaus, J. O. & Fohrmann, H. (1995), 'Outflow of dense water from the Storfjord in Svalbard: a numerical model study', *Journal of Geophysical Research-Oceans* **100**(C12), 24719–24728.

Kämpf, J. (2000), 'Impact of multiple submarine channels on the descent of dense water at high latitudes', *Journal of Geophysical Research-Oceans* **105**(C4), 8753–8773.

Kämpf, J. (2005), 'Cascading-driven upwelling in submarine canyons at high latitudes', *Journal of Geophysical Research-Oceans* **110**(C2).

Killworth, P. (1977), 'Mixing on the Weddell Sea continental slope', *Deep-Sea Research* **24**, 427–448.

Killworth, P. (2001), 'O the rate of descent of overflows', *Journal of Geophysical Research-Oceans* **106**(C10), 22267–22275.

Lane-Serff, G. & Baines, P. G. (1998), 'Eddy formation by dense flows on slopes in a rotating fluid', *Journal of Fluid Mechanics* **363**, 229–252.

Lea, D. J., Haine, T. W. N. & Gasparovic, R. F. (2006), 'Observability of the Irminger Sea Circulation using variational data assimilation', *Q. J. Roy. Met. Soc.* **132**(618), 1545–1576.

Legg, S., Hallberg, R. W. & Girton, J. B. (2006), 'Comparison of entrainment in overflows simulated by z-coordinate, isopycnal and non-hydrostatic models', *Ocean Modelling* **11**(1-2), 69–97.

MacCready, P. (1994), 'Frictional decay of abyssal boundary currents', *Journal of Marine Research* **52**(2), 197–217.

Mauritzen, C., Price, J., Sanford, T. & Torres, D. (2005), 'Circulation and mixing in the Faroese Channels', *Deep-Sea Research Part I-Oceanographic Research Papers* **52**(6), 883–913.

Nicholls, K. W. & Østerhus, S. (2004), 'Interannual variability and ventilation timescales in the ocean cavity beneath Filchner-Ronne Ice Shelf, antarctica', *Journal of Geophysical Research-Oceans* **109**(C4).

Nof, D. (1983), 'The translation of isolated cold eddies on a sloping bottom', *Deep-Sea Research Part A-Oceanographic Research Papers* **30**(2), 171–182.

Nøst, O. A. & Foldvik, A. (1994), 'a model of ice-shelf ocean interaction with application to the Filcher-Ronne and Ross Ice Shelves', *Journal of Geophysical Research-Oceans* **99**(C7), 14243–14254.

SCAAR (2006), 'Antarctic digital database', *www.add.scar.org* .

Sherwin, T. J. & Turrell, W. R. (2005), 'Mixing and advection of a cold water cascade over the Wyville Thomson Ridge', *Deep-Sea Research Part I-Oceanographic Research Papers* **52**(8), 1392–1413.

Sherwin, T., Griffiths, C., Inall, M. & Turrell, W. (2007), 'Quantifying the overflow across the Wyville Thomson Ridge into the Rockall Trough', *Deep Sea Research* (submitted).

Tanaka, K. & Akitomo, K. (2001), 'Baroclinic instability of density current along a sloping bottom and the associated transport process', *Journal of Geophysical Research-Oceans* **106**(C2), 2621–2638.

Vilibic, I., Grbec, B. & Supic, N. (2004), 'Dense water generation in the north adriatic in 1999 and its recirculation along the Jabuka Pit', *Deep-Sea Research Part I-Oceanographic Research Papers* **51**(11), 1457–1474.

Wåhlin, A. K. (2002), 'Topographic steering of dense currents with application to submarine canyons', *Deep-Sea Research Part I-Oceanographic Research Papers* **49**(2), 305–320.

Wåhlin, A. K. (2004), 'Downward channeling of dense water in topographic corrugations', *Deep-Sea Research Part I-Oceanographic Research Papers* **51**(4), 577–590.

Wåhlin, A. K. & Walin, G. (2001), 'Downward migration of dense bottom currents', *Environmental Fluid Mechanics* **1**, 257 – 259.

Wells, M. G. & Wettlaufer, J. S. (2005), 'Two-dimensional density currents in a confined basin', *Geophysical And Astrophysical Fluid Dynamics* **99**(3), 199–218.

APPENDIX

A Smooth ridge

The solution to the equation

$$\frac{\partial \hat{h}}{\partial \hat{y}} - \gamma \hat{h} = \frac{2\hat{y}}{(1+\hat{y}^2)^2} \tag{45}$$

i.e. (16) using (37), can be found by use of Fourier transformation. Defining the Fourier transform $F(k)$ of the function $f(\hat{y})$ as

$$F(k) = \int_{-\infty}^{\infty} f(\hat{y}) e^{-2\pi i k \hat{y}} d\hat{y} \tag{46}$$

and

$$f(\hat{y}) = \int_{-\infty}^{\infty} F(k) e^{2\pi i k \hat{y}} dk \tag{47}$$

and performing the transformation on equation (45) gives

$$2\pi i k F(k) - \gamma F(k) = \int_{-\infty}^{\infty} \frac{2\hat{y} e^{-2\pi i k \hat{y}}}{(1+\hat{y}^2)^2} d\hat{y}. \tag{48}$$

The integral on the right-hand side can be evaluated using calculus of residues, giving

$$\int_{-\infty}^{\infty} \frac{2\hat{y} e^{-2\pi i k \hat{y}}}{(1+\hat{y}^2)^2} d\hat{y} = -2ik\pi^2 e^{-2\pi k}. \tag{49}$$

Consequently we have

$$F(k) = \frac{-\pi e^{-2\pi k}}{(1 - \frac{\gamma}{2\pi i k})}, \tag{50}$$

which (using the inverse Fourier transform) gives the sought solution $\hat{h}(\hat{y})$,

$$\begin{array}{rl} \hat{h}(\hat{y}) = & \frac{-1}{1+\hat{y}^2} + \frac{i\gamma}{2} e^{\gamma(\hat{y}+i)} Ei(\gamma(\hat{y}+i)) - \frac{i\gamma}{2} e^{\gamma(\hat{y}-i)} Ei(\gamma(\hat{y}-i)) \\ & + e^{\gamma \hat{y}} \left[1 - \frac{i\gamma}{2} e^{i\gamma} Ei(\gamma i) + \frac{i\gamma}{2} e^{-i\gamma} Ei(-\gamma i) \right]. \end{array} \tag{51}$$

B Cosine-shaped and linear canyons

Cosine-shaped canyon Assume that the topography is given by

$$\hat{D}(x,\hat{y}) = sx + \tfrac{1}{2}\left[\cos(\pi\hat{y}) + 1\right] \quad -2 \le \hat{y} \le 0 \ . \tag{52}$$

Using the requirement of maximal downslope transport, i.e. $\hat{h}(0) = 0$ and requiring that $\hat{h} > 0$ for $Y_L < \hat{y} < 0$, the solution to (16) using (25) is given by

$$\hat{h}(\gamma,\hat{y}) = \begin{cases} \frac{\pi^2}{2(\pi^2+\gamma^2)}\left[e^{\gamma\hat{y}} - \cos(\pi\hat{y}) - \frac{\gamma}{\pi}\sin(\pi\hat{y})\right] & Y_L \le \hat{y} < 0 \\ 0 & \hat{y} < Y_L, \hat{y} > 0 \end{cases} \tag{53}$$

where $-2 \le Y_L \le -1$ and $\hat{h}(Y_L) = 0$. The downslope transport can not be found analytically but must be calculated numerically from (17).

Linear canyon Assume that the topography is given by

$$\hat{D}(x,y) = \begin{cases} sx - \hat{y} - 1 & -2 \le \hat{y} < -1 \\ sx + \hat{y} + 1 & -1 \le \hat{y} \le 0 \end{cases} \ . \tag{54}$$

Using the requirement of maximal downslope transport, i.e. $\hat{h} > 0$ and requiring that $\hat{h} > 0$ for $Y_L < \hat{y} < 0$, the solution to (16) using (25) is given by

$$\hat{h}(\hat{y}) = \begin{cases} \left(-\frac{1}{\gamma} + \frac{2}{\gamma}e^{\gamma}\right)e^{\gamma\hat{y}} - \frac{1}{\gamma} & -2 \le \hat{y} < -1 \\ -\frac{1}{\gamma}e^{\gamma\hat{y}} + \frac{1}{\gamma} & -1 \le \hat{y} \le 0 \end{cases} \tag{55}$$

where

$$Y_L = \frac{1}{\gamma}\ln\left(\frac{1}{2e^{\gamma} - 1}\right). \tag{56}$$

Using (17) the geostrophical downslope transport is given by

$$T_{Linear\ Canyon} = \frac{1}{\gamma^2}\left(2e^{-\gamma} - 2 + \ln(2e^{\gamma} - 1)\right). \tag{57}$$

Topographic steering of dense overflows: laboratory experiments with V-shaped ridges and canyons

E. Darelius [1,2]

(1) Geophysical Institute, University of Bergen, Norway
(2) Bjerknes Centre for Climate Research, Bergen, Norway

Abstract

Topographic corrugations such as canyons and ridges cross-cutting the path of a dense plume may effectively steer all or part of the plume downslope. A dynamical regime, in which the along-slope transport is balanced by a return flow in the Ekman layer to maintain a geostrophically balanced downslope flow along the corrugation, has been proposed. An analytical model (Darelius & Wåhlin 2007, Wåhlin 2002) incorporating these physics is compared with laboratory experiments of dense gravity currents flowing down sloping, V-shaped canyons and ridges in a rotating frame of reference. The response of the flow to variations in four governing parameters (slope, rotation, volume flux and reduced gravity) is generally described well by the model. Vertical velocity profiles resolving the Ekman spiral were obtained using a Laser Doppler Velocimeter and they showed the secondary, transverse circulation superimposed on the primary, downslope flow. A particle flowing down the canyon/along the ridge can be expected to follow a helix-like path, and dye released within the dense layer showed this. The experiments support the dynamical regime proposed for topographically steered flows, and verifies the analytical model. The gravity current was observed to divide in two when the transport capacity of the corrugation was exceeded; one part continued along the slope and the other flowed downslope along the corrugation.

1 Introduction

Dense water formed on shallow continental shelves and in marginal seas descends the continental slope as density driven plumes (Price & Baringer 1994) and replenishes the deep oceans. However important, the physics governing the pathway of these plumes is poorly understood. A better comprehension of dense plumes is needed to improve the understanding of the global thermohaline circulation, in which they play an important role, and its response and sensitivity to changes in climatic forcing.

Dense water on a slope adjusts geostropically and the main flow direction is along the isobaths. Ageostrophic processes, such as frictionally induced Ekman transport (e.g. Wåhlin &

Walin (2001)) and baroclinic eddies (e.g. Tanaka & Akitomo (2001)), will cause a downslope transport of dense water. Dense water may also be steered downslope by submarine canyons (Wåhlin 2002, Baines & Condie 1998) and ridges (Darelius & Wåhlin 2007) cross-cutting the continental shelf. The latter process, topographic steering of dense plumes, is the focus of this work. One example of a topographically steered plume is the Wyville Thompson Ridge Overflow, where dense water descends to great depths following a small canyon (Sherwin et al. 2007, Sherwin & Turrell 2005). Another example is the Filchner Overflow, part of which follows a submarine ridge downslope (Darelius et al. 2007, Darelius & Wåhlin 2007, Foldvik et al. 2004). Channeling of dense water by canyons and ridges has also been observed in laboratory experiments (Wåhlin et al. 2007, Davies et al. 2006, Kämpf 2005, Baines & Condie 1998) and in numerical models (Kämpf 2000, Jiang & Garwood 1998).

When considering topographic steering, two key questions emerge: how much water can a ridge or a canyon channel downslope, and what are the parameters and the dynamics controlling the flow? These questions were addressed by Wåhlin (2002), who focussed on canyons, and by Darelius & Wåhlin (2007), who considered submarine ridges. Hereafter canyons and ridges will be referred to jointly as "corrugations" while "wall" refers to the corrugation wall on which the flow is "leaning" (Marked with 'W' in Fig. 1). The downslope flow is assumed to be mainly geostrophic, and it induces an Ekman transport away from the wall in the bottom boundary layer. Due to the sloping bottom, the geostrophic flow has a component towards the wall. If the transverse flows are in balance, i.e. if the Ekman transport away from the wall equals the geostrophic transport towards it, then a geostrophically balanced downslope flow, leaning on the corrugation, can be maintained. The dense water is thus expected to follow a helix-like path down the slope: flowing towards the wall in the interior and away from it in the bottom boundary layer. Such a secondary circulation is present in many flow configurations, e.g. in rotating channel flows (Garrett 2004). Bottom friction will cause a Ekman transport in the bottom boundary layer to the left of the main flow direction that is balanced by a return flow in the interior. This has been observed within the Faroe Bank Channel (Johnson & Sanford 1992), in the Juan Fuca Strait (Ott et al. 2002) and in laboratory experiments (Johnson & Ohlsen 1994). The difference between the rotating channel flow and that along a sloping corrugation, is that in the former, the secondary circulation does not pose any restrictions on the main flow; any given flow has a certain secondary circulation associated with it. In the latter, the secondary circulation does pose restrictions on the primary, downslope flow. If the Ekman transport is too small, excess fluid will be transported over the corrugation wall. If the Ekman transport is too large, the layer will flatten out, reducing the velocity of the downslope flow, and hence the Ekman transport, until a state is reached in which the across corrugation flows exactly balance each other.

A 1.5-layer analytical model including the dynamics described above has been applied to sinusoidal (Wåhlin 2002) and V-shaped (Davies et al. 2006) canyons and to several ridge topographies (Darelius & Wåhlin 2007). The model predicts the thickness and shape of the dense layer and quantifies the transport capacity, i.e the maximum amount of water that

a corrugation can channel downslope. On shallow slopes and for narrow topographies the transport capacity of ridges are an order of magnitude larger than that of a canyon (Darelius & Wåhlin 2007). Davies et al. (2006) compared a similar analytical model with laboratory experiments representing the Faroe Bank Outflow, and found it to agree qualitatively well. The downslope velocities in the channel were geostrophic, and the observed interfaces agreed with model solutions. Baines & Condie (1998) have shown experimentally that canyons can steer dense plumes downslope. The authors suggested that enhanced mixing within the canyon may reduce the penetration depth of the plume water. This was confirmed by Wåhlin et al. (2007), who in a laboratory setting compared mixing within topographically steered plumes and plumes descending on an open slope. Kämpf (2005) studied a set of multiple canyons and showed, both numerically and experimentally, that a dense down-flow within a canyon induced a counter-flow in the upper layer. The upslope counter-flow could explain observed intrusions of deeper water masses on the Antarctic continental shelves, for example.

The purpose of this work is to investigate, over a range of parameters, the behavior of a dense current flowing downslope along a sloping corrugation and to experimentally test the theoretical model described above. One set of experiments was performed with the dense source placed on the slope at some distance from the corrugation. The dense plume initially flowed along the slope, until impinging on the corrugation. When the flux of dense water was smaller than the transport capacity of the corrugation the entire dense plume was steered downslope. If the transport capacity was exceeded, portions of the dense fluid flowed over the corrugation while the remaining plume was steered downslope as before. A second set of experiments was performed with the source placed in the canyon or in the vicinity of a ridge to focus on flow along the sloping corrugation. The dense fluid was dyed with fluorescence and the interface position could be found from vertical transects and compared with the theoretical solutions. The secondary circulation was visualized with dye and measured using a Laser Doppler Velocimeter. The wedge-shaped interface previously observed in canyon and channel flows (Davies et al. 2006, Mauritzen et al. 2005, Johnson & Ohlsen 1994, Saunders 1990, Borenäs & Lundberg 1988) was also observed in the vicinity of a ridge.

2 Theory

Consider a dense plume that flows along a continental slope and impinges on a corrugation, e.g. a canyon as in Fig. 1a (the same argument can be applied to a ridge), crosscutting the shelf. The plume splits, and part of the water is steered along the canyon, i.e. down the slope, while the rest flows out of the canyon and continues along the slope. The focus will be on the part of the plume that is steered down the canyon and downslope of the transition region where the splitting of the plume occurs. Theory describing such a flow is explained in Darelius & Wåhlin (2007), Davies et al. (2006) and Wåhlin (2002) but will be briefly summarized here. The flow is assumed to be geostrophic to the leading order and from now on rotation is positive (Northern hemisphere). Directions (right/left) refer to looking

upslope.

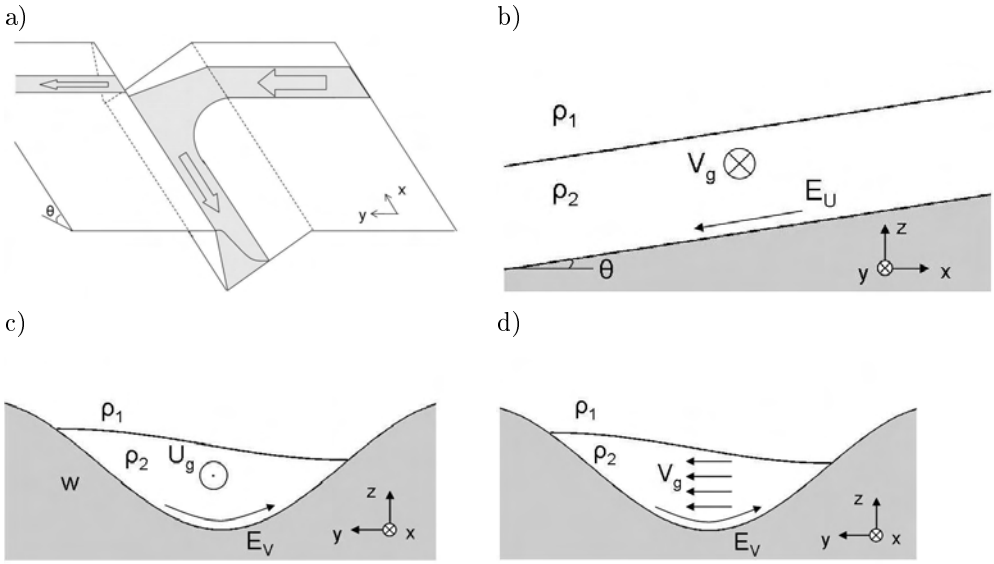

Figure 1: *a) Overview of a dense plume impinging on a submarine canyon with part of the dense water being steered downslope. b) Along canyon (x-direction) and c) across canyon (y-direction) transects showing the sloping interface, the geostrophic currents and the Ekman transport and d) total flow across the canyon. The wall on which the flow is "leaning" is marked with a W in (c).*

Fig. 1b-c show sketches of along- and across-canyon transects of the canyon flow. The interface is sloping both in the x- and y-direction, and the geostrophic current consequently has an across-canyon component, V_g, directed towards the wall, as well as a downslope component, U_g. The current induces a Ekman transport with a downslope component, E_U, associated with V_g, and an across-canyon component, E_V, which is associated with U_g and directed away from the wall. Considering the across canyon flow only (Fig. 1d), we have a geostrophic flow towards the wall in the interior and a Ekman transport away from it in the bottom Ekman layer. These two flows must balance, i.e. the net transport across the canyon must be zero, for the dense water to remain within the canyon and for the flow to be steady. Fluid moves between the Ekman layer and the interior through Ekman pumping. A particle flowing down the canyon can thus be expected to follow a helix-like path.

If the x-axis is directed up the slope and we assume that (1) the interior flow is geostrophic, (2) the upper layer is infinitely thick, homogenous and motionless, (3) the entrainment of

ambient water is negligible, and that (4) the flow is constant in the x-direction ($\partial/\partial x = 0$) and in time ($\partial/\partial t = 0$), then the requirement about zero net transport across the corrugation (Darelius & Wåhlin 2007, Davies et al. 2006, Wåhlin 2002) gives (using a linear bulk friction parameterization)

$$h\frac{g'}{f}\frac{\partial D}{\partial x} + \delta\frac{g'}{f}\left(\frac{\partial D}{\partial y} + \frac{dh}{dy}\right) = 0 \tag{1}$$

where g' is the reduced gravity, f the Coriolis parameter, D the bottom elevation, δ the Ekman layer thickness and h the layer thickness, which has been assumed constant in the along canyon direction ($h_x = 0$). The experiments described in the following sections were performed with V-shaped ridges and canyons with a width W, a height H (where $H = W$) and a slope $s = \sin\theta$, where θ is the angle between the corrugation and the horizontal (Fig. 1). The bottom elevation, D, can thus be written as

$$D_{ridge} = \begin{cases} sx & y < -W \\ sx + y\frac{H}{W} + H & -W \le y < 0 \\ sx - y\frac{H}{W} + H & 0 \le y < W \\ sx & W \le y \end{cases} \tag{2}$$

for the ridge and

$$D_{canyon} = \begin{cases} sx & y < -W \\ sx - y\frac{H}{W} - H & -W \le y < 0 \\ sx + y\frac{H}{W} - H & 0 \le y < W \\ sx & W \le y \end{cases} \tag{3}$$

for the canyon. Using (2) or (3) and dividing with g'/f (1) gives

$$\frac{dh}{dy} = \frac{hs}{\delta} - \frac{\partial D_{corrugation}}{\partial y}. \tag{4}$$

The solutions to (4) that give the maximum geostrophic downslope transport, i.e. the transport capacity, are

$$h_{ridge} = \begin{cases} H\frac{1}{\gamma}\left(e^{\gamma} - 1\right)e^{\gamma y/W} & y < -W \\ H\frac{1}{\gamma}\left(1 - e^{\gamma y/W}\right) & -W \le y < 0 \end{cases} \tag{5}$$

and

$$h_{canyon} = \begin{cases} 0 & -W \le y < Y_L \\ H\frac{1}{\gamma}\left[\left(2 - e^{-\gamma}\right)e^{y\gamma/W} - 1\right] & Y_L \le y < 0 \\ H\frac{1}{\gamma}\left(1 - e^{-\gamma}e^{y\gamma/W}\right) & 0 \le y \le W \end{cases} \tag{6}$$

where $Y_L = -\frac{W}{\gamma}ln(2 - e^{-\gamma})$ and

$$\gamma = \frac{sW}{\delta}. \tag{7}$$

The non-dimensional parameter γ is hence governing the flow. Small values of γ give wide and thick dense layers flowing relatively slowly downslope while large γ gives narrow and thin layers and higher velocities (Darelius & Wåhlin 2007).

The transport capacity can be found by horizontally integrating hU_g across the corrugation and it is given by

$$Q_{ridge} = \frac{g'H^2}{f}\frac{1}{\gamma^2}(\gamma - 1 + e^{-\gamma}) \tag{8}$$

and

$$Q_{canyon} = \frac{g'H^2}{f}\frac{1}{\gamma^2}[2e^{-\gamma} - 2 + ln(2e^{\gamma} - 1)]. \tag{9}$$

The transport capacity for a given g', H and f is larger for ridges than for canyons, since the lateral extent of the dense layer is limited in the canyon. The difference is largest for small values of γ (Darelius & Wåhlin 2007).

3 Experimental apparatus

Two kinds of experiments will be reported on in this paper: initial "overview experiments", in which a dense flow on a slope is observed to impinge on a corrugation, and more process oriented "corrugation experiments" where flow along a sloping corrugation is studied in detail. The main focus is on the corrugation experiments. Rotation is positive (northern hemisphere) in all experiments and directions (right/left) refer to looking upslope.

3.1 "Overview" experiments

Overview experiments were performed in the Geophysical Fluid Dynamics Laboratory in Seattle, USA (small-scale) and on the rotating Coriolis platform in Grenoble, France (large-scale).

The small-scale experiments were performed in a cone-shaped tank with a diameter of 1.22 m, whose sides had a slope $\theta = 18°$ and where one slope-section was exchangeable to allow the insertion of corrugations. The corrugations were shaped in oil-clay and had a height/depth of 2 cm and a width of 4 cm. The total water depth was 20 cm and the tank was rotating with $\omega = 0.38$ s^{-1}. Dense water with a salinity of 5 was colored blue and injected from a source at the top of the slope (roughly 30 cm from the corrugation) with a volume flux Q=1 cm^3/s using a diffuser. A digital camera was placed above the tank.

The large-scale experiments were similar, but performed in a tank measuring 13 m in diameter. A 10 cm high and 16 cm wide ridge was placed on a large (2.5 x 8 m) slope which was inclined to the bottom, $\theta = 6°$. The rotation period, T_{rot}, was 60 s. In the two experiments, the dense plume had a reduced gravity, g', of 0.1 and 0.02 m/s^2 and the

volume flux at the source, Q, was 10 and 20 l/min, respectively. The total water depth was 35 cm. Details on the experimental setup are given in Wåhlin et al. (2007).

3.2 "Corrugation Experiments"

The corrugation experiments were conducted in the Geophysical Fluid Dynamics Laboratory in Seattle, USA using a 122 x 122 x 25 cm square tank, placed concentrically on a rotating table (Fig. 2). A ridge and a canyon made of plexiglass and with dimensions and shapes as shown in Fig. 3 were alternately placed in the tank, with one end raised to make an angle θ with the bottom of the tank. Depending on the visualization technique to be used, the corrugations were lined with either black or white plastic. The tank was filled with freshwater

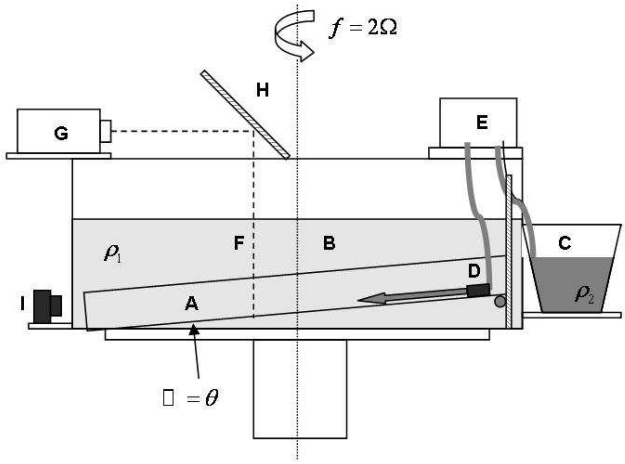

Figure 2: *Sketch of the experimental apparatus: (A) Sloping topography, (B) Fresh water tank, (C) Dense water container, (D) Point source, (E) Peristaltic pump, (F) Vertical light sheet, (G) Slide projector, (H) Mirror and (I) Camera.*

of density ρ_1, that was initially in solid body rotation. A container of dense water, $\rho_2 > \rho_1$, was placed on the rotating table and connected to a dense source made of plastic tubes and a peristaltic pump. A diffuser composed of sponge and cloth was used to reduce mixing at the source. In the case of a canyon, the source was placed in the center of the canyon and in the case of a ridge it was placed 2-3 cm to the right of the ridge break. In both cases the source was placed 10 cm from the top of the slope. The experiment was initialized as the peristaltic pump was switched on, releasing dense water at a rate Q. Measurements and

photo acquisition were started 15 minutes after the current was established.

Two visualization techniques were used:

(1) Vertical transects A vertical light sheet orthogonal to the corrugation axis was illuminated half way down the channel using a slide projector and a mirror. The dense source was dyed with fluorescein and photographs were taken using a digital camera placed at the bottom of the slope.

(2) Visualization of the secondary circulation (Ekman helix) A source of dye was added about 20 cm downslope of the dense source, 1 mm above the bottom and 1-1.5 cm left of the center of the corrugation. The dye was injected continuously through a thin (1 mm) glass tube. A second digital camera was mounted above the tank.

In a few canyon experiments a Laser Doppler Velocimeter (LDV) was installed to obtain vertical velocity profiles. Due to limited instrument availability, only two parameter combinations were explored, see Table 1. The LDV was moved vertically in discrete steps of 0.64 mm, waiting 15 seconds at each step, and it was placed roughly half way down the slope, either in the center of the canyon or 1 cm to the left. The vertical extension of the LDV sensing volume was set to 0.8 mm. Prior to the experiments the LDV was calibrated using an object moving with a known velocity. Fluorescent transects were obtained in combination with the velocity measurements.

When the LDV was not available, velocities were measured using intermittently released dye and a camera. Small portions of dyed dense water ($\rho = \rho_2$) were released every 3.4 s, at a point 1 cm above the bottom over the center of the corrugation. The experiments were photographed from above and the distance, l, between the dyed points was measured and the velocity estimated ($v = l/3.4$ s).

The temperature in the tank and in the beaker containing the inflowing saline water was measured prior to all experiments. Densities were calculated using the sea water package in Matlab and the observed temperatures (varying between 20-22°C) and salinities. The salinity was not measured directly. A standard saline solution was prepared by mixing a known mass of salt with a known volume of distilled water. The salinity of the standard solution was controlled using an Abbe refractometer and portions of it were diluted to obtain the right salinity and volume. The accuracy of the salinity is estimated to about 10%. Up to three experiments were usually performed in a row, i.e. without emptying the tank. In between experiments the dense water on the bottom of the tank was removed using a pipette. The remaining saline water was mixed with the ambient water, causing an increase in salinity on the order of 10^{-2}.

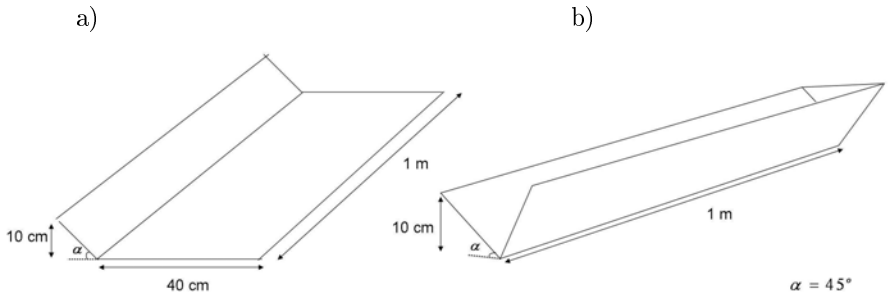

Figure 3: *Shape and dimensions of the inserted a) ridge and b) canyon topographies*

The effect of varying the Coriolis parameter f, background slope s, reduced gravity g' ($g' = g\frac{\Delta\rho}{\rho_2}$, where $g = 9.8$ m/s^2 and $\Delta\rho$ is the density difference between the layers) and flux Q on the shape and thickness of the layer was investigated using the fluorescein visualization technique described above. One parameter was varied, while the others were kept constant at reference values. The parameter range covered in the experiments is listed in Table 1, where the reference values are marked in bold and the values used for secondary flow visualization with asterisks. The parameters used during the LDV experiments are shown in the same table.

The distance over which the flow is expected to adjust geostrophically is in the order of the internal Rossby radius of deformation, $R = \sqrt{g'H}/f$. For the parameters used here the maximal value of R is about 0.1 m, while the vertical transects were obtained roughly 0.5 m from the source.

3.2.1 Data processing

The interface position from the fluorescein transects was extracted from the digital photos by means of the pixel value of the green channel. The dense layer was identified as the area where this value exceeded a chosen limiting value. The limiting value was adjusted manually from experiment to experiment to compensate for variations in light intensity and fluorescein concentration.

Parameter	Symbol	Values for Fluorescein	Values for LDV	Unit
Slope	s	0.01*, 0.02, **0.04**, 0.08, 0.16	0.04	
Rotation period	T	59.7, 29.4, **15.2***, 7.6	15.2	s
Coriolis factor	f	0.19, 0.38, **0.76***, 1.5	0.76	s^{-1}
Ekman l. t.	δ	1.6, 1.1, **0.8***, 0.6	0.8	mm
Flux	Q	0.75*, **1.5**, 3	3	cm^3/s
Salinity	S	0.63, **1.25***, 2.5	(i) 2.5	
			(ii) 5	
Reduced gravity	g'	0.005, **0.01***, 0.02	(i) 0.02	m/s^2
			(ii) 0.04	m/s^2
	γ	0.1-3.2		

Table 1: *Parameter-space covered during the experiments with fluorescein transects and LDV measurements. Bold values indicate the reference values and asterisks the parameter values used in the experiments where the secondary flow was visualized. (l. t. = layer thickness)*

4 Results

4.1 A dense plume impinging on a corrugation

In two sets of experiments a dense plume was observed impinging on corrugations cross-cutting a sloping bottom. Fig. 4 shows a small-scale ridge experiment. The results from the canyon experiments are similar. The dense plume initially adjusted to rotation, veered to the right and flowed along the slope with an angle of 10-20° to the isobaths. When the plume reached the corrugation, the flow direction changed and the dense water was steered downslope by the topography. The flux of dense water, Q, was smaller than the transport capacity of the corrugation, $Q_{corrugation}$ (eq. 8-9), and no water passed over the corrugation.

The results from the large-scale experiments are similar. When the flux of dense water was smaller than the transport capacity of the ridge, i.e. $Q < Q_{ridge}$, the geostrophic flow along the slope was interrupted and all the dense water was steered downslope (Fig. 5a). In a second experiment the flow parameters were changed so that $Q > Q_{ridge}$. A part of the dense water was then observed to pass over the ridge and to continue flowing along the slope on the other side (Fig. 5b). The picture is here somewhat complicated by the development of eddies within the dense plume, presumably caused by the increased flux (see e.g. Cenedese et al. (2004) for a discussion of eddies and flow regimes within dense plumes).

4.2 Fluorescent transects

Cross-section photographs from ridge experiments with varying slope are shown in Fig. 6 and from canyon experiments with varying rotation in Fig. 7. In Fig. 6b the detected interface position is included. The flow is directed towards the camera. In all experiments the dense water is leaning on the wall, generally reaching higher up the wall with increased rotation (f), increased flux (Q) and/or reduced density difference (g'). The character of the interface varies across the transect. To the left, in the vicinity of the wall, the interface is diffuse while it is sharper on the right side.

Fig. 8 to 15 show the interface from the experiments (extracted from photos) and the corresponding theoretical interfaces obtained using the laboratory parameters. The Ekman layer thickness is given by $\delta = (\nu/2f)^{1/2}$ where $\nu = 10^{-6}$ m^{2}s^{-1} is the molecular viscosity of water. To account for the interfacial Ekman layer (Section 4.4 and 5) an effective Ekman layer thickness of 1.5 x δ was used in the calculations. Two robust features of the experimental interfaces are captured by theory. Firstly, the interface is horizontal in the vicinity of the wall, and secondly, the dependence of the steepness of the middle region on rotation and slope agrees. The most noteworthy difference is that the interface height (see Fig. 6a for definition) is larger in the experiments than in theory. Fig. 16 shows the experimental values of interface height versus the theoretical values. The theory seems to underestimate the interface height by a factor of about 0.8.

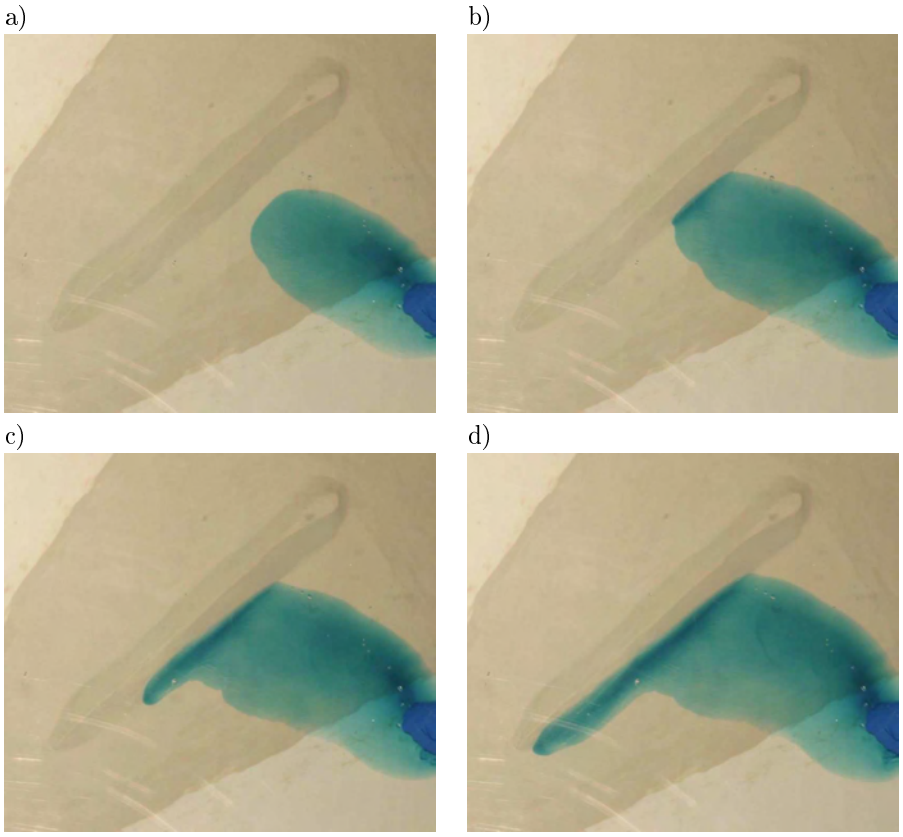

Figure 4: *A dense plume impinging on a ridge, $Q < Q_{ridge}$. a) t=0 s, b) t=16 s, c) t=32 s, and d) t=48 s in a small-scale "Overview Experiment"*

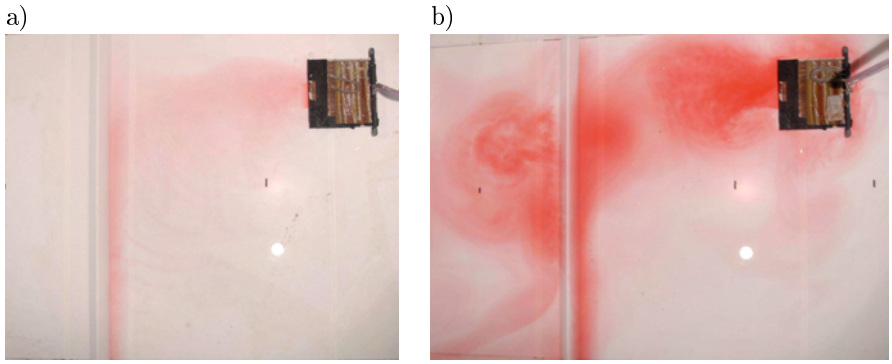

Figure 5: *A dense plume impinging on a ridge a) $Q < Q_{ridge}$ and b) $Q > Q_{ridge}$ in the large-scale "Overview Experiments".*

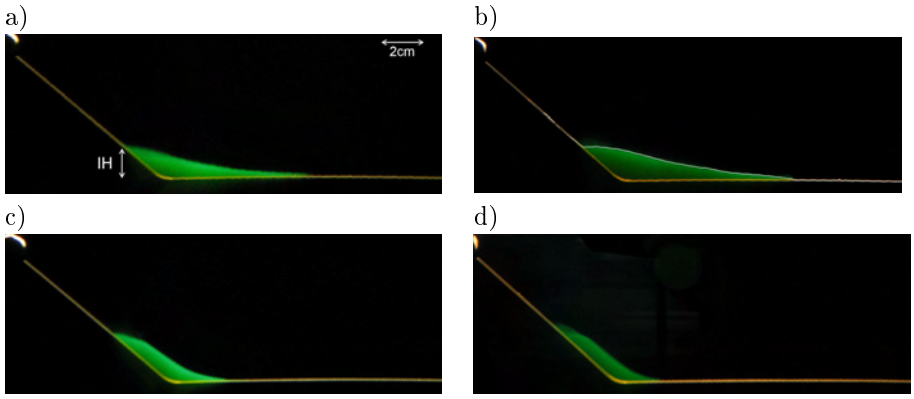

Figure 6: *Ridge transects obtained about 50 cm from the source using reference values for flux, rotation and salinity (Q, f and g') and different slopes (s): a) 0.02, b) 0.04, c) 0.08, and d) 0.16. The interface height, IH, and the scale is shown in (a) and in (b) the extracted interface (from data processing) is shown in white.*

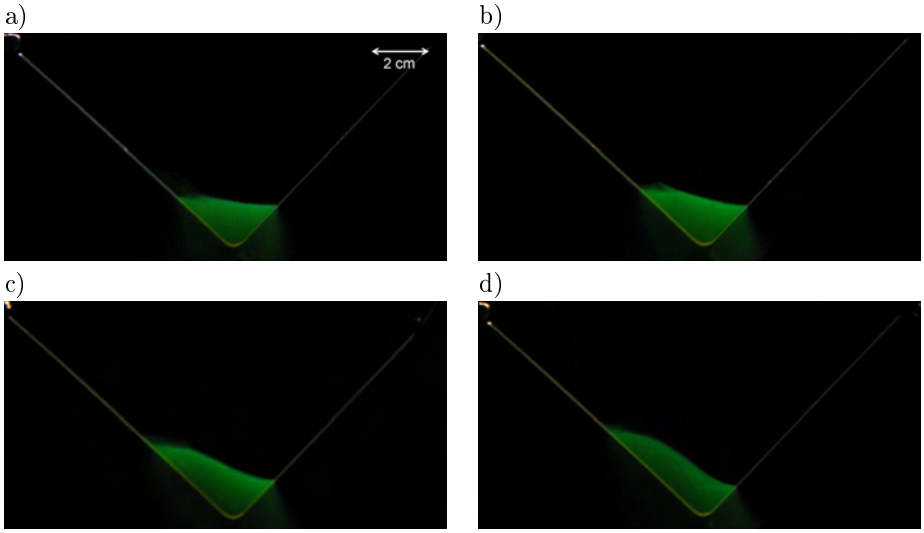

Figure 7: *Canyon transects obtained 50 cm from the source using reference values for flux, slope and reduced gravity (Q, s and g') and different rotation (f): a) f=0.2 s^{-1}, b) f=0.4 s^{-1}, c) f=0.8 s^{-1}, and d) f=1.6 s^{-1}. The scale is shown in (a).*

A certain time-variation in the position of the interface (up to 1 cm for extreme cases) was observed. The bars in Fig. 8-15a show the maximum excursion of the interface from its mean position at the center of the corrugation. Variability in the interface position was generally small in the canyon experiments (< 1 mm), and larger in the ridge experiments, especially for large values of Q, f and s. In the experiments with large variations the surface appeared wavelike, with crests propagating in the along ridge direction. Similar waves were observed along the ridge in the large-scale overview experiments (see Fig. 5 in Wåhlin et al. (2007)). In experiments without waves, the change in layer thickness along the corrugation was judged to be small.

4.3 The secondary circulation

The secondary circulation described in Section 2 and sketched in Fig. 1d was visualized with dye injected in the bottom boundary layer. Fig. 17 shows the injected dye following a helix-like path down the canyon. The dye flowed to the right across the canyon in the Ekman layer, and returned to the left in the oppositely directed interior flow. The flow in the interior makes an angle of 5° with the center line, i.e. $V_g \simeq 0.1U_g$ (Fig. 17b). The Ekman layer thickness is roughly 2 mm or about one tenth of the layer thickness, i.e. $\delta \simeq 0.1h$ and equation (1) is thus fulfilled. To be consistent the mean, vertically integrated flow in the Ekman layer ought to make an angle of 85° with the center line, i.e. $E_V = 10E_U$. The observed angle is much smaller; 20-45°. The velocity within the Ekman layer changes with depth, decreasing and veering to the left towards the bottom (the Ekman spiral) and it is uncertain at what depth above the bottom the dye is moving. The dye streak is relatively clear and not smeared out which indicates that it is concentrated vertically. The direction is different between the first and the second passage in the Ekman layer, suggesting that the dye is moving at different levels.

Similar experiments were made with ridge topographies, but the dye signal became diffuse and hard to observe when approaching the right, thin side of the layer, as the dye spread out and dispersed to a greater extent than in the canyon experiments. The overall picture, with dyed water moving right along the bottom and left in the interior was nevertheless observed.

4.4 Vertical velocity profiles

Vertical velocity profiles were obtained from two canyon experiments using a Laser Doppler Velocimeter (LDV). The two parameter combinations that were explored (Table 1) gave dense layers with a thickness of about (i) 1.5 cm and (ii) 1 cm in the center of the canyon. In both cases the interface slope was estimated to be 22°, giving along-canyon geostrophic velocities of (i) 1 cm/s and (ii) 2 cm/s. The across-canyon geostrophic velocity was calculated from s, giving (i) 0.1 cm/s and (ii) 0.2 cm/s.

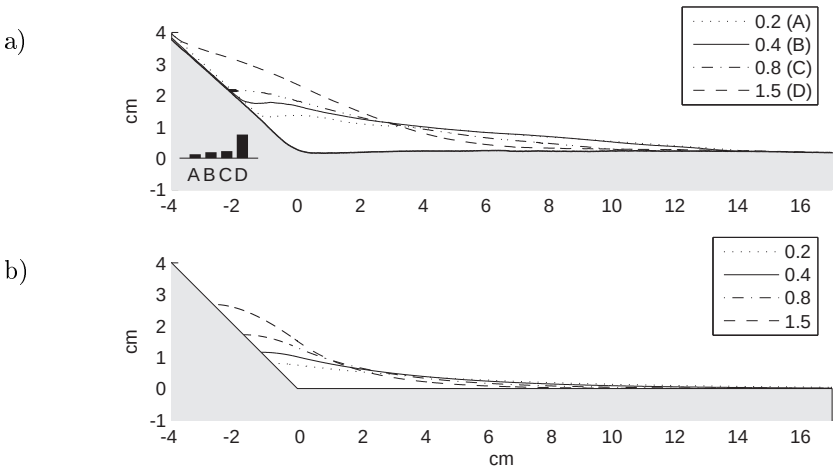

Figure 8: *Interface positions obtained for different f in a) laboratory experiments and b) from theory. The bars on the left in figure (a) show the maximum excursion of the interface from its mean position at the ridge break. Legends show values of f (s^{-1}) and the letter identifying the corresponding "variability-bar".*

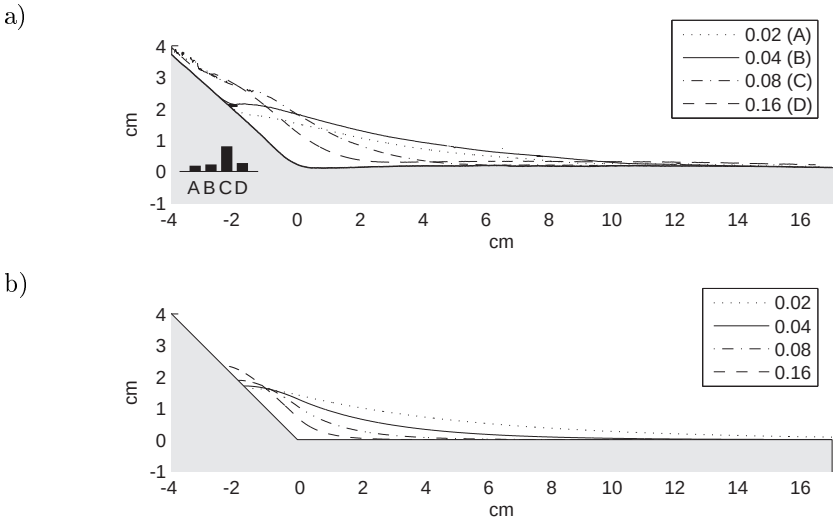

Figure 9: *As in Fig. 8, but with different s. Legends show values of s and the letter identifying the corresponding "variability-bar".*

a)

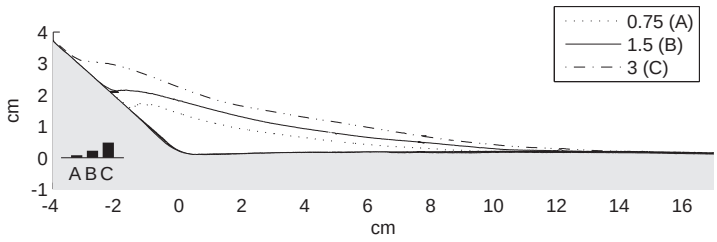

b)

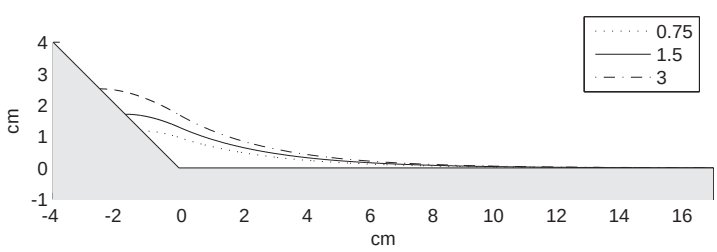

Figure 10: *As in Fig. 8, but for different Q and constant γ. Legends show values of Q (cm^3/s) and the letter identifying the corresponding "variability-bar".*

a)

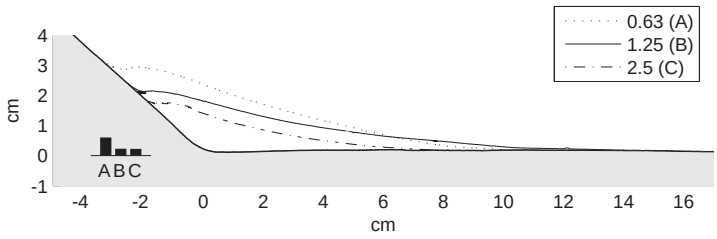

b)

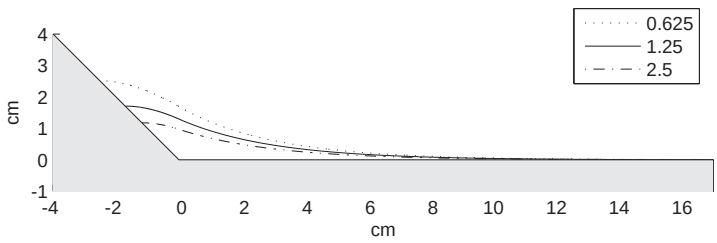

Figure 11: *As in Fig. 8, but for different g' and constant γ. Legends show values of salinity and the letter identifying the corresponding "variability-bar".*

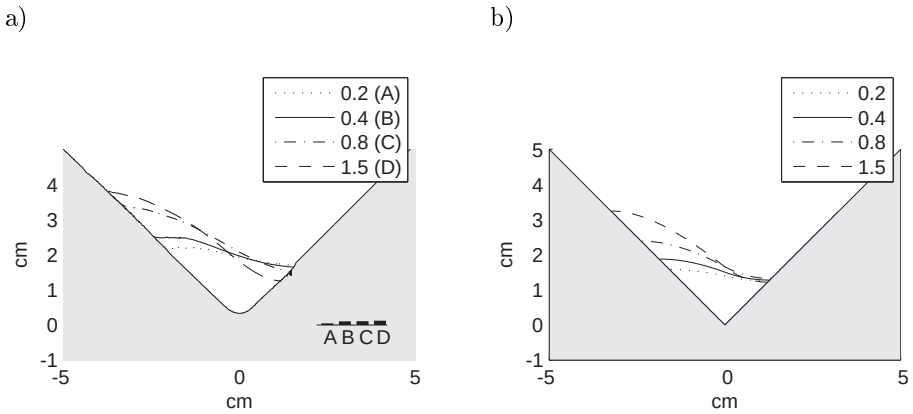

Figure 12: *Interface positions obtained for different f in a) laboratory experiments and b) from theory. The bars on the right in figure (a) show the maximum excursion of the interface from its mean position at the center of the canyon. Legends show values of f (s^{-1}) and the letter identifying the corresponding "variability-bar".*

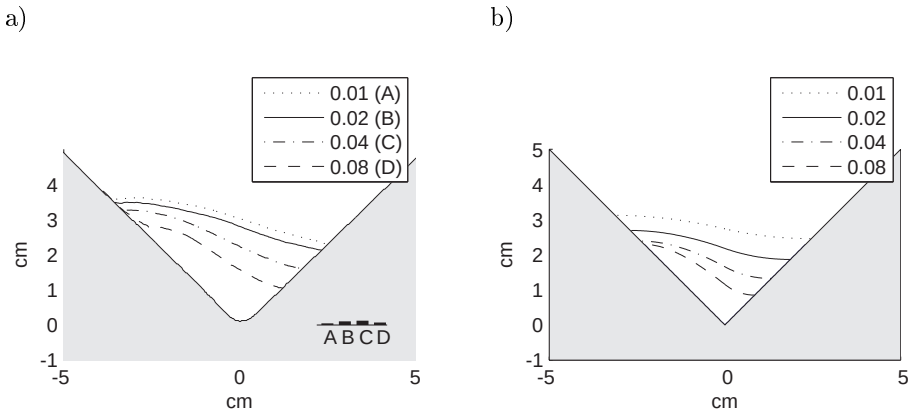

Figure 13: *As in Fig. 12, but for different s. Legends show values of s and the letter identifying the corresponding "variability-bar".*

a) b)

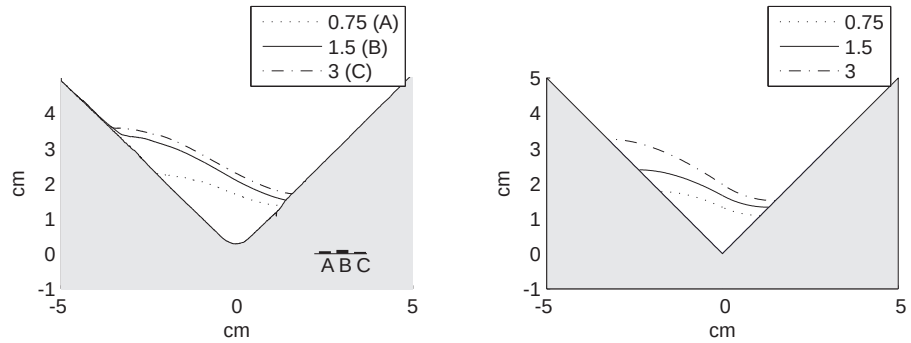

Figure 14: *As in Fig. 12, but for different Q and constant γ. Legends show values of Q (cm^3/s) and the letter identifying the corresponding "variability-bar".*

a) b)

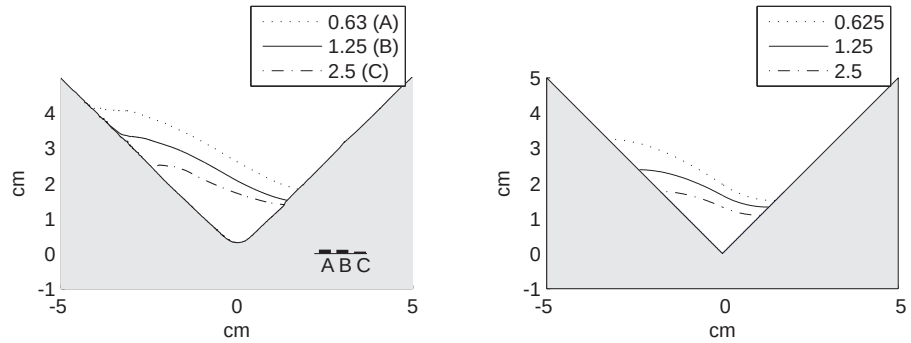

Figure 15: *As in Fig. 12, but for different g' and constant γ. Legends show values of salinity and the letter identifying the corresponding "variability-bar".*

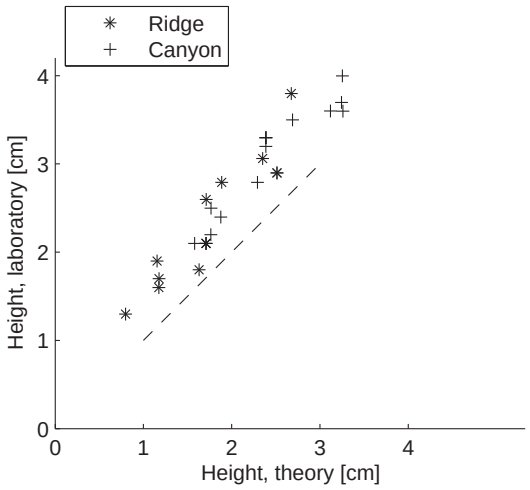

Figure 16: *Theoretical versus laboratory interface height, as defined in Fig. 6a. The dashed line shows a 1:1 relationship.*

The profile obtained in the center of the canyon for the first parameter combination (Table 1) is shown in Fig. 18a and that obtained 1 cm to the left of the center in Fig. 18b. In the interior (0.8 cm above the bottom) the measured along canyon velocities are 0.8 (1.0) cm/s in the center (to the left) of the canyon and 0.08 (0.08) cm/s across it, i.e. close to geostrophic. The velocity profiles show a vertical structure with a 2-3 mm thick bottom Ekman layer and indications of a weaker interfacial Ekman layer. Superposed on the measurements in Fig. 18 are the velocity profiles given by Ekman theory (e.g. Cushman-Roisin (1994)),

$$\begin{aligned} u(z) &= U_0[1 - e^{-2z/\delta}cos(z/\delta)] - V_0 e^{-2z/\delta}sin(2z/\delta) \\ v(z) &= U_0 e^{-2z/\delta}sin(2z/\delta) + V_0[1 - e^{-2z/\delta}cos(2z/\delta)] \end{aligned} \tag{10}$$

where U_0 and V_0 are the interior velocities (from LDV) and $\delta = (\nu/2f)^{1/2}$ the Ekman layer thickness.

Measurements from the second parameter combination (Table 1) gave similar profiles but a thinner dense layer and a sub geostrophic velocity (1.4-1.5 cm/s along the canyon). It is hypothesized that the layer was too thin for a geostrophic interior to develop. Time series from point measurements 1-1.5 cm above the bottom showed that the flow oscillated

a)

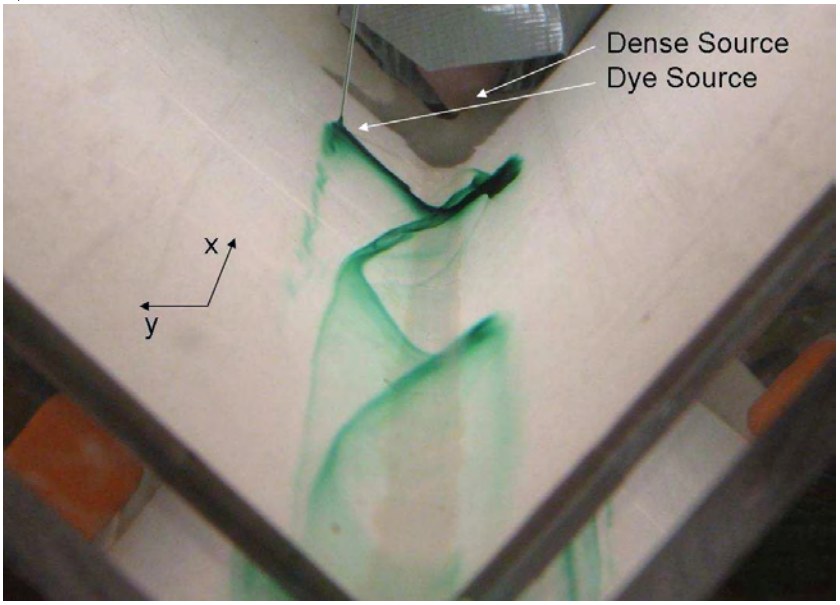

b)

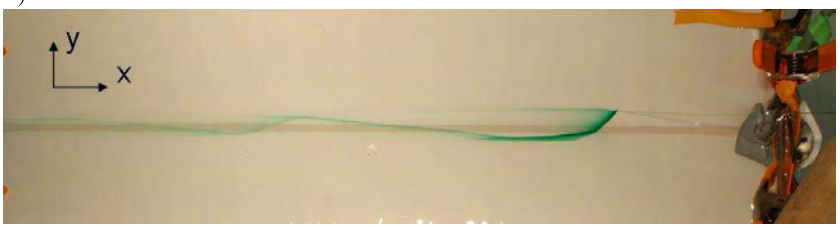

Figure 17: *The "Ekman helix" traced out by dye injected in the bottom boundary layer seen a) up the canyon and b) from above. The secondary circulation makes a particle follow a helix-like path down the canyon, and not a straight line.*

with an amplitude $\Delta u \sim 0.1$ cm/s and a period $T \sim 100$ s.

4.5 Other velocity measurements

Velocity data is also available from other experiments, where the velocity was estimated from photographs of intermittently released dye. Velocities were found to vary (with a factor of two or less) for many of the ridge experiments, while there was little variability in the canyon experiments. This agrees with the observations of wave-like features in many of the ridge

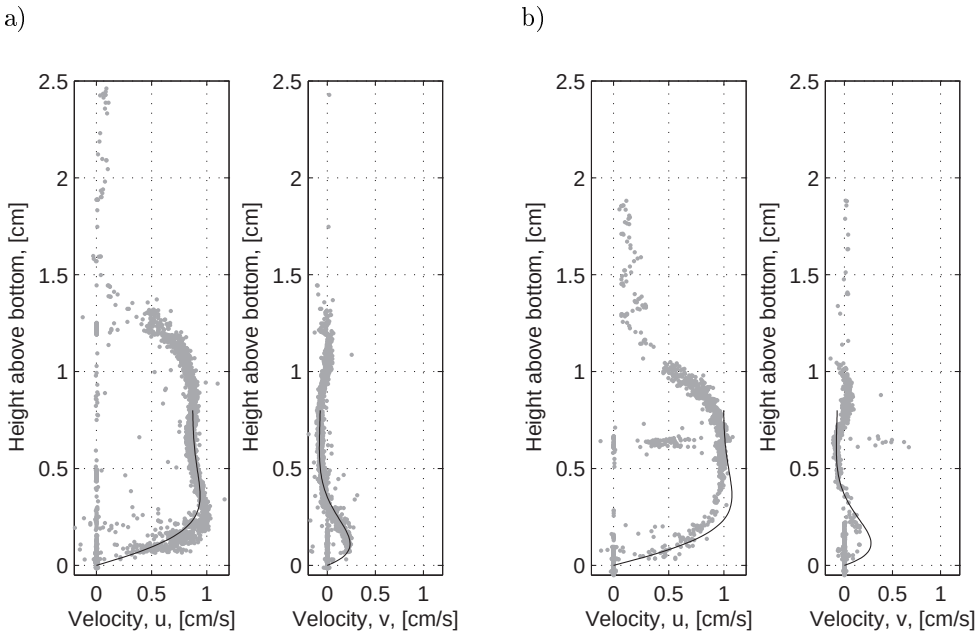

Figure 18: *Velocity profile from a) the center of the canyon and b) 1 cm to the left (looking up the canyon) as measured with LDV (dots) in experiment (i), see Table 1. The theoretical velocity profiles from Ekman theory (10) are shown in black.*

experiments. The ridge velocity measurements were not considered confident and were thus discarded. The measured canyon velocities agree relatively well with geostrophic velocities (calculated using the slope of the interface obtained from the fluorescent transects), but they are (in all but one case) lower (Fig. 19).

5 Discussion

Most theoretical and laboratory studies of dense plumes describe flow on uniform slopes where the downslope transport is associated with friction and viscous Ekman drainage or eddies. The continental slopes are, however, not smooth, but generally transversed with canyons and ridges that can potentially steer dense plume water downslope. This has been observed in the Filchner overflow, Antarctica (Darelius & Wåhlin 2007, Foldvik et al. 2004), along the Wywille Thompson Ridge (Sherwin et al. 2007, Sherwin & Turrell 2005), and in the laboratory (Wåhlin et al. 2007, Baines & Condie 1998), and it was confirmed in the present study. Previous theoretical work (Darelius & Wåhlin 2007, Wåhlin 2004, 2002) sug-

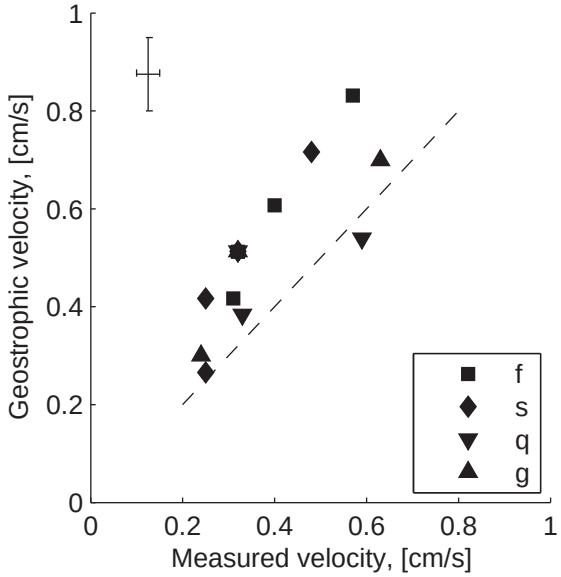

Figure 19: *Measured velocity versus the geostrophic velocity calculated from the observed interface slope. The dashed line indicates a 1:1 relationship. Typical error bars are included in the upper left corner.*

gests a dynamical regime in which the Ekman transport associated with the downslope flow balances the geostrophic component directed across the corrugation. If the net-transport across the corrugation is zero then a steady state is possible in which the dense water flows downslope leaning on the wall. The secondary, transverse flow hence restricts the primary, downslope flow, as it determines the position of the interface and limits the amount of water that the corrugation can steer downslope.

In this study, results from an analytical model including these dynamics (Darelius & Wåhlin 2007, Wåhlin 2002, 2004) are compared with laboratory experiments on dense downslope flows in V-shaped corrugations. Despite the simplifications involved in the derivation of the theoretical expressions for layer thickness, they agree qualitatively well with the experimental results. The shape of the dense layer is recaptured, as well as the response to variations in the governing parameters, indicating that the analytical model captures the physics of the experiments. The slope of the layer interface (across the corrugation) increases with increasing slope (s) and rotation (f, hence for decreasing Ekman layer thickness, δ), i.e. for increasing γ, as expected from theory. Changes in flux, (Q), and reduced gravity (g'), do not affect the interface slope, but only the interface height (see Fig. 6a for defini-

tion). The increase in interface height with increasing Q and decreasing g' is in line with the theoretical predictions. The interface height is, however, underestimated by a factor of about 0.8. This means that $Q_{corrugation}$ is overestimated, since it is proportional to the interface height squared. This discrepancy may partly be attributed to the assumption that Q and g' are constant along the channel, i.e. that entrainment is negligible. The interface is distinct and well defined, which indicates that mixing is limited, but some entrainment can nevertheless be expected, especially close to the source. Entrainment will increase Q while reducing g', and cause the interface height to increase. In addition, entrainment along the path will make the interfacial Ekman layer more important, i.e. increase the effective δ and reduce γ. The LDV measurements revealed the presence of a weak interfacial Ekman layer. The interfacial Ekman layer can be included in the model by letting $\delta = \delta_{bottom} + \delta_{interface}$, as done by Davies et al. (2006) (hereafter D06). Here a value of $\delta = 1.5 \times \delta_{bottom}$ is used in the theoretical calculations to account for the interfacial Ekman layer. In the theoretical calculation the geostrophic transport is considered (eq. 5-6), and the reduction of the transport in the Ekman layer is not taken into account. This will cause an over-estimation of the transport capacity and consequently an under-estimation of the interface height. Assuming that the downslope transport within the Ekman layer is reduced by 50%, gives a reduction of the total transport of 5% and an increase in interface height of 2-3% for $\delta = 0.1h$.

D06 has previously compared a similar analytical model to laboratory simulations of the Faroe Bank Outflow and found it agreed well. Their experiment differed from those presented here on a number of points. Firstly, the D06 experiment was performed in a widening canyon or channel, representing the actual Faroe Bank Channel geometry. This caused a "bulge" to develop on the left flank of the channel as the flow adjusted to the shifting transport capacity of the widening canyon. In the present experiments constant geometries were used and no "bulge" was observed. Secondly, the D06 flow was turbulent with relatively high Reynolds number, $\mathrm{Re} = UW/\nu$, ($\mathrm{Re} \sim 1600 - 8000$), while the experiments presented here were laminar with lower Reynolds numbers (typically $\mathrm{Re} \sim 200$). The difference in turbulence level influences the strength of the interfacial Ekman layer. The transverse flow at the interface was more pronounced, and clearly observed, in the turbulent experiments, while in this study it was weaker and observed only in the LDV measurements. Thirdly, the theoretical expressions in D06 made use of a different non-dimensionalisation, while the expressions presented here follow the derivation in Darelius & Wåhlin (2007). Finally, D06 define the Ekman layer thickness $\delta = (C_D + E)\frac{g'\alpha}{f^2}$ where α is the slope of the side wall and E the entrainment coefficient, i.e. δ is the sum of the interfacial and the bottom Ekman layer thicknesses.

Two visual observations warrant further comments: the development of waves and the wedge-shaped interface.

In a few experiments the interface height and shape varied slowly and the surface appeared wavelike. These disturbances were noted for large fluxes and/or large rotation and

slopes and mostly in the ridge experiments. The LDV measurements revealed a certain time-dependence in the fastest canyon flow (ii), where an oscillation in both u and v with a period $T \simeq 100$ s and an amplitude of 0.05-0.1 cm/s was found. The flow can nevertheless be described as "quasi-steady", since the waves were slowly evolving and the temporal Rossby number, $\mathrm{Ro}_T \sim 1/fT$, consequently low (about 0.01). Similar wave structures were observed along the ridge and canyon in the large scale Coriolis experiments (Wåhlin et al. 2007), but their origin is unclear. Curiously, a data set from a mooring placed in the vicinity of a ridge crosscutting the path of the dense Filchner Overflow plume, Antarctica (Foldvik et al. 2004) shows strong oscillations with a period of 6 days (Darelius et al. 2007) that existing theories are unable to explain. A rotation period (T_r) of 16 s and an oscillation period of 100 s would correspond to a period of 6 days. This, however, may be coincidental.

A wedge-shaped interface was observed in all experiments. The interface was sharp away from the wall and more diffuse in the vicinity of it. This has previously been observed in canyons both in the ocean e.g. in the Faroe Bank Channel (Mauritzen et al. 2005, Saunders 1990, Borenäs & Lundberg 1988) and in laboratory experiments (Davies et al. 2006, Johnson & Ohlsen 1994). The same wedge-shaped area is found in inviscid rotating hydrualic control models (Hogg 1983). According to the present study, the phenomena also appears in the vicinity of a ridge. The secondary circulation provides two possible explanations for these observations. The first involves the vertical movement of water between the Ekman layer and the interior. Johnson & Sanford (1992) suggested that water leaving the Ekman layer and moving up into the interior on the right side (away from the wall) would compress the density surfaces and create a sharp interface there. Close to the wall water moves downward into the the Ekman layer, presumably making the interface diffuse (Ezer 2006). The second explanation proposed is that light fluid entering the Ekman layer on the left side is "dragged" below denser water in the interior, causing static instability and convection (Moum et al. 2004). It is not possible from the current data set to determine whether either of the suggested processes, or a combination of them, are at play.

The secondary circulation was visualized with dye and quantified with LDV measurements. These resolve the bottom Ekman layer and show vertical velocity profiles that are well described by Ekman theory. To our knowledge, this has not previously been recorded in a laboratory experiment. The secondary circulation is similar to that observed in the Faroe Bank Channel (Johnson & Sanford 1992) and in exchange-flow experiments (Johnson & Ohlsen 1994).

The analytical model is idealized, and relies on a number of assumptions, of which the most important are discussed below (others have been discussed above, e.g. negligible entrainment (page 97)).
(1) The flow is geostrophically balanced
As discussed by Darelius & Wåhlin (2007) the theory is strictly valid only for geostrophically balanced flow, i.e. when the advection terms $(u \cdot u_x + v \cdot u_y, u \cdot v_x + v \cdot v_y)$ are zero. The terms

can be neglected if the Burger number (Bu= $g'H/f^2/W^2$) or γ^2Bu is small. The standard parameter values used here (Table 1) and an approximate height and width scale of 3 cm gives $Bu \approx 2$ and γ^2Bu ≈ 1. Advection might thus be expected to affect the solutions, but it is unclear in what way. It would be of great interest to apply a numerical model to the problem, so that the effect of advection, both horizontal and vertical, on these flows can be considered.
(2) The ambient water is motionless
The LDV measurements indicate that the ambient water is close to motionless, as assumed in the analytical model. Kämpf (2005) showed in a numerical model and in laboratory experiments that a dense downslope flow within a canyon may incite a barotropic counterflow in the upper layer. However, the LDV measurements show no flow in the upper layer, indicating that such a counterflow does not exist in the present parameter regime and set-up. The presence of a barotropic pressure field would considerably modify the model results, since a larger interface tilt is needed to compensate for that of the free surface.

Despite the simplifications, the analytical model was found to describe the laboratory experiments relatively well, indicating that the model captured the relevant physics. The flow is governed by the dimensionless parameter $\gamma = sW/\delta$, which in the parameter range covered during the experiments, takes values of $\gamma = 0.1 - 3.2$. Approximate ocean values of γ are similar, e.g. about 1/2.5/4 for the Faroe Bank Channel, Wyville Thompson Ridge Overflow and the Filchner Overflow respectively (using δ ~35 m). The Reynolds number is many orders of magnitude larger in the ocean, R e$\sim O(10^8)$, than in the laboratory, Re $\sim O(10^2)$, and the oceanic plumes are fully turbulent whereas the laboratory plumes are laminar. This aspect of the flow is incorporated in the definition of δ. Entrainment, which is neglected here, is an essential feature of oceanic plumes (Price & Baringer 1994) and the increased velocity in the topographically steered flows may further increase entrainment (Wåhlin et al. 2007, Baines & Condie 1998). Entrainment will, as discussed above, increase Q while g' and the transport capacity are reduced, and in the case of an entraining plume, dense water may be expected to constantly flow over the wall. In addition, entrainment represents an interfacial stress, modifying the presented theory. The interfacial stress was, in the Faroe Bank Outflow, found to be small compared with the bottom stress (Mauritzen et al. 2005), although it is uncertain how representative that finding is for other plumes. The LDV-profiles presented here show an interfacial Ekman layer, indicative of interfacial stress and entrainment, but they do not alter the underlying physics.

The continental slopes are generally replete with topographic corrugations on scales less than 10 km. This study, along with the earlier theoretical work upon which it builds (Darelius & Wåhlin 2007, Wåhlin 2002) and the experiments reported on by Wåhlin et al. (2007) and Baines & Condie (1998), suggests that such small-scale corrugations may effectively channel relatively large quantities of dense water downslope, and that their effect on dense plumes and overflows cannot be neglected. The experiments described here provide evidence to support the physical regime proposed by Wåhlin (2002) and verify an analytical

model (Darelius & Wåhlin 2007, Wåhlin 2002), which allows for a first-order estimate of the transport capacity of canyons and ridges cross-cutting a slope.

Acknowledgements I am thankful to Prof. P. Rhines at the School of Oceanography, University of Washington for making the lab available and to E. Lindahl for technical assistance during the experiments. The stay at University of Washington was funded by World University Network, WUN. The stay in Grenoble was supported by the European Community's Sixth Framework Programme through the grant to the budget of the Integrated Infrastructure Initiative HYDRALAB III, Contract no. 022441 (RII3), and the experiments were carried out with help from S. Viboud, H. Didelle, J. Sommeria, G. Lane-Serff, J. Buck and A. Wåhlin. Discussions and suggestions from P. Rhines, E. Lindahl, G. Lane-Serff, A. Wåhlin and T. Eldevik were greatly appreciated, as was assistance with Fig. 1 from F. Chiche.

References

Baines, P. G. & Condie, S. (1998), Observations and modelling of antarctic downslope flows: a review, *in* S. S. Jacobs & R. F. Weiss, eds, 'Ocean, Ice, and Atmosphere - Interaction at the Antarctic Continental Margin', Vol. 75, AGU, Washington D.C.

Borenäs, K. M. & Lundberg, P. A. (1988), 'On the deep-water flow through the Faroe Bank Channel', *Journal of Geophysical Research-Oceans* **93**(C2), 1281–1292.

Cenedese, C., Whitehead, J. A., Ascarelli, T. A. & Ohiwa, M. (2004), 'A dense current flowing down a sloping bottom in a rotating fluid', *Journal of Physical Oceanography* **34**(1), 188–203.

Cushman-Roisin, B. (1994), *Introduction to Geophyscial Fluid Dynamics*, Prentics-Hall Inc., Upper Saddle River, New Jersey.

Darelius, E. & Wåhlin, A. (2007), 'Downward flow of dense water leaning on a submarine ridge', *Deep Sea Research* **56**(7), 1173–1188.

Darelius, E., Smedsrud, L., Østerhus, S., Foldvik, A. & Gammelsrød, T. (2007), 'On the structure and variability of the Filchner Overflow plume', (Manuscript).

Davies, P., Wåhlin, A. & Guo, Y. (2006), 'Laboratory and analytical model studies of the FBC deep water outflow', *Journal of Physical Oceanography* **36**(7), 1348–1364.

Ezer, T. (2006), 'Topographic influence on overflow dynamics: Idealized numerical simulations and the Faroe Bank Channel overflow', *Journal of Geophysical Research* **111**(C02002).

Foldvik, A., Gammelsrød, T., Østerhus, S., Fahrbach, E., Rohardt, G., Schrøder, M., Nicholls, K. W., Padman, L. & Woodgate, R. A. (2004), 'Ice shelf water overflow and bottom water formation in the southern Weddell Sea', *Journal of Geophysical Research-Oceans* **109**(C2).

Garrett, C. (2004), 'Frictional processes in straits', *Deep-Sea Research Part II - Topical Studies In Oceanography* **51**(4-5), 393–410.

Hogg, N. G. (1983), 'Hydraulic control and flow separation in a multi-layered fluid with applications to the Vema Channel', *Journal of Physical Oceanography* **13**(4), 695–708.

Jiang, L. & Garwood, R. W. (1998), 'Effects of topographic steering and ambient stratification on overflows on continental slopes: a model study', *Journal of Geophysical Research-Oceans* **103**(C3), 5459–5476.

Johnson, G. C. & Sanford, T. B. (1992), 'Secondary circulation in the Faroe Bank Channel Outflow', *Journal of Physical Oceanography* **22**(8), 927–933.

Johnson, G. C. & Ohlsen, D. R. (1994), 'Frictionally modified rotating hydraulic channel exchange and ocean outflows', *Journal of Physical Oceanography* **24**(1), 66–78.

Kämpf, J. (2000), 'Impact of multiple submarine channels on the descent of dense water at high latitudes', *Journal of Geophysical Research-Oceans* **105**(C4), 8753–8773.

Kämpf, J. (2005), 'Cascading-driven upwelling in submarine canyons at high latitudes', *Journal of Geophysical Research-Oceans* **110**(C2).

Mauritzen, C., Price, J., Sanford, T. & Torres, D. (2005), 'Circulation and mixing in the Faroese Channels', *Deep-Sea Research Part I-Oceanographic Research Papers* **52**(6), 883–913.

Moum, J. N., Perlin, A., Klymak, J. M., Levine, M. D., Boyd, T. & Kosro, P. M. (2004), 'Convectively driven mixing in the bottom boundary layer', *Journal of Physical Oceanography* **34**(10), 2189–2202.

Ott, M. W., Dewey, R. & Garrett, C. (2002), 'Reynolds stresses and secondary circulation in a stratified rotating shear flow', *Journal of Physical Oceanography* **32**(11), 3249–3268.

Price, J. & Baringer, M. (1994), 'Outflows and deep-water production by marginal seas', *Progress in Oceanography* **33**(3), 161–200.

Saunders, P. M. (1990), 'Cold outflow from the Faroe Bank Channel', *Journal of Physical Oceanography* **20**(1), 29–43.

Sherwin, T. J. & Turrell, W. R. (2005), 'Mixing and advection of a cold water cascade over the Wyville Thomson Ridge', *Deep-Sea Research Part I-Oceanographic Research Papers* **52**(8), 1392–1413.

Sherwin, T., Griffiths, C., Inall, M. & Turrell, W. (2007), 'Quantifying the overflow across the Wyville Thomson Ridge into the Rockall Trough', *Deep Sea Research* (submitted).

Tanaka, K. & Akitomo, K. (2001), 'Baroclinic instability of density current along a sloping bottom and the associated transport process', *Journal of Geophysical Research-Oceans* **106**(C2), 2621–2638.

Wåhlin, A. K. (2002), 'Topographic steering of dense currents with application to submarine canyons', *Deep-Sea Research Part I-Oceanographic Research Papers* **49**(2), 305–320.

Wåhlin, A. K. (2004), 'Downward channeling of dense water in topographic corrugations', *Deep-Sea Research Part I-Oceanographic Research Papers* **51**(4), 577–590.

Wåhlin, A. K. & Walin, G. (2001), 'Downward migration of dense bottom currents', *Environmental Fluid Mechanics* **1**, 257 – 259.

Wåhlin, A. K., Darelius, E., Cenedese, C. & Lane-Serff, G. (2007), 'Laboratory observations of enhanced entrainment in the presence of submarine canyons and ridges.', *Deep Sea Research* (submitted).

Laboratory observations of enhanced entrainment in the presence of submarine canyons and ridges

A. Wåhlin[1]***, E. Darelius***[2,3]***, C. Cenedese***[4] ***& G. Lane-Serff*** [5]
(1) Earth Science Center, Göteborg University, Sweden
(2) Geophysical Institute, University of Bergen, Norway
(3) Bjerknes Centre for Climate Research, Bergen, Norway
(4) Woods Hole Oceanographic Institution, USA
(5) School of Mechanical, Aerospace and Civil Engineering, University of Manchester, UK

Abstract

The continental slopes are often covered by small-scale topographic features such as submarine canyons and ridges. Dense plumes flowing geostrophically along the slope may encounter such features and all, or part of, the dense water can be steered downslope. A set of laboratory experiments was conducted at the rotating Coriolis platform to investigate the effect of small-scale topography on plume mixing. A dense water source was placed on top of a slope, and experiments were repeated with three topographies: a smooth slope, a slope with a ridge, and a slope with a canyon, and for three flow regimes: laminar, wave-, and eddy-generating plumes. When a ridge or a canyon was present on the slope the dense plume was steered downslope and waves developed along the ridge and canyon wall, regardless of the flow characteristics on the smooth slope. Froude numbers were estimated, and were found to be higher for the topographically steered flow than for flow on smooth topography. The stratification in the collecting basin was monitored and the mixing inferred. The total mixing increased when a ridge or a canyon was present, and the increased entrainment rate was hence more important than the shortened path. The difference in mixing levels between the regimes was smaller when topography was present, indicating that it was the small-scale topography and not the large-scale characteristics of the flow that determined the properties of the end product. Eddies were observed to degenerate when encountering topography, and the dense water trapped beneath them was steered downslope.

1 Introduction

Density currents supply bottom water to the deep ocean and the process by which these mix with the ambient water influences the basin stratification. It has been shown in laboratory experiments (e.g. Wells & Wettlaufer (2005), Baines (2001, 2005), Baines & Turner (1969)) how an entraining plume builds stratification in the basin that it 'feeds', and that the mixing in the plume determines the stratification in the basin. The sensitivity of ocean stratification to plume entrainment and its parameterization has been studied in regional ocean models

(e.g. Chang et al. (2005)) and in more idealized basins and models (e.g. Hughes & Griffiths (2006), Wåhlin & Cenedese (2006)).

Laboratory studies (e.g. Adduce & Cendese (2007), Cenedese et al. (2004), Ellison & Turner (1959)) show that the entrainment rate increases with the Froude number, i.e. the ratio between the current velocity and the speed of a long internal wave. For supercritical flows, where the Froude number is greater than one, instabilities may develop, which give rise to enhanced entrainment rates. This has been observed, for example, in Lake Geneva (Fer et al., 2001, 2002). For subcritical flows, the entrainment rates are smaller than for supercritical flows, but they are still an increasing function of the Froude number (Adduce & Cendese 2007, Cenedese et al. 2004). The same dependency is found in the ocean (e.g Girton & Sanford (2003), Price & Baringer (1994)), although oceanic supercritical flows are rare, perhaps because of the large entrainment rates that these flows have. Given the comparatively large entrainment rates for supercritical flows, a first-order description is that they entrain ambient water until they become subcritical. In one-dimensional 'streamtube' descriptions of the plume (e.g. Smith (1975) and Price & Baringer (1994)) the entrainment rate depends strongly on the average slope of the bottom (Wåhlin & Cenedese 2006).

Small-scale topographic features, such as submarine ridges and canyons, can act to steer dense water downslope. This has been observed in the Wyville Thompson Ridge Overflow (Sherwin et al. 2007, Sherwin & Turrell 2005), in the Adriatic Sea (Vilibic et al. 2004), in the Filchner Overflow (Darelius et al. 2007, Foldvik et al. 2004) in laboratory experiments (Darelius 2007, Davies et al. 2006, Kämpf 2005, Baines & Condie 1998) and in numerical models of dense outflows (Kämpf 2000, Jiang & Garwood 1998). As the water is steered downslope by topography the plume thickness and velocity, and thereby the Froude number, change. The entrainment rate of a plume is increased in the vicinity of topography (Jiang & Garwood 1998, Baines & Condie 1998), but the descent rate, and thus the plume path and the distance over which mixing places, decreases for a topographically steered plume. The effect of small-scale topography on dense plumes is generally not considered; neither the channeling and increased downslope transport that they induce nor the increased entrainment that may be associated with the enhanced downslope flow. The aim of our study is to investigate to what extent small-scale topography affects the mixing in a dense plume.

A set of laboratory experiments was conducted at the Coriolis rotating platform in Grenoble. The three parameter regimes described by Cenedese et al. (2004) were investigated. These, on a smooth topography, produced a laminar flow, a flow with roll-waves, and a flow with eddies. Each of these experiments was repeated, first with a submarine ridge, and then with a canyon, positioned on the slope. The total mixing was measured by sampling the basin water with vertically traversing probes every 5 minutes. This method appears to give a reliable estimate of the mixing provided the length of the slope exceeds the frictional drainage length scale (Lane-Serff & Baines 1998), so that artificial mixing at the end wall is avoided. In all three regimes, the total mixing was larger when small-scale

topography was present on the slope than when it was not. The increased entrainment rate is hence more important than the shortened path.

2 Experimental set-up

The experiments were conducted on the Coriolis rotating platform, in a 13 m diameter tank. Fig. 1 shows a sketch of the experimental set-up. A sloping bottom, making an angle $\alpha = 6^\circ$ with the horizontal (i.e. a 1:10 aspect ratio) and measuring 8 x 2.5 m was placed in the tank. The slope was connected to a 25 cm high horizontal shelf on one side and on the other side, via vertical false walls, to the outer circular wall, sealing off a semi-circular basin. The dashed area in Fig. 1c indicates the position of a removable section, where the smooth slope could be replaced by a canyon or a ridge. From now on ridge and canyon will be referred to jointly as "corrugation" and directions (right/left) are referred to looking upslope. The ridge (canyon) was 16 cm wide and 10 cm high (deep), and oriented perpendicular to the along-slope direction. A dense water source was placed on the top-right side of the slope, 25 cm from the shelf break. The source consisted of a rectangular plastic box filled with horsehair and an assemblage of thin (0.5 cm in diameter) plastic tubes through which the dense water flowed (Fig. 1b). The source was 2.5 cm high and 20 cm wide.

The tank was initially filled with fresh water to a depth D and spun up to a rotation period $T = 60$ s ($f = 0.21$ s^{-1}). The injected water was either (approximately) 0.04% or 0.1% denser than the ambient fluid, which corresponds to a reduced gravity of 0.004 m/s^2 and 0.01 m/s^2. At the start of the experiment the source was opened, releasing dense water at a rate $Q_0 = 10$ l/min. The ambient water depth was kept constant by an open surface drain, which could be adjusted vertically, in the opposite side of the tank. The flow was visualized by coloring the source water red and videotaping it from above. The dye was added from a separate pump with a flow rate that could be adjusted manually, hence it was possible to switch the dye source on and off during the experiment. The experiments were normally run for about an hour before the first recording. To visualize the motion in the upper layer, floating markers were sprinkled on the free surface. The salinity in the enclosed basin was monitored with two vertically traversing probes, C4 and C5 (see Fig. 1c for position). The probes were lowered with a speed of 1 cm/s making one profile every 5 minutes during the course of the experiments. Only data recorded during the downcasts are considered here.

The source flow rate, density, and ambient water depth were tuned in order to produce three different flow regimes characterized by laminar flow, roll-waves, and eddies (see Cenedese et al. (2004)). In addition, two criteria had to be fulfilled:
1) the frictional drainage length L_D (see e.g. Lane-Serff & Baines (1998)),

$$L_D = \frac{Q f^{\frac{3}{2}}}{g' \alpha \sqrt{2\nu}} \tag{1}$$

where Q is the source flow rate, f the Coriolis parameter, g' the reduced gravity and ν the

Regime	Topography	D (cm/s)	$\Delta\rho_0$ (kg/m^3)	L_D	$Q_{C/R}$	U_N
Laminar	Smooth	65	3.7	2.9	-	1.7
	Ridge	65	4.4	2.4	19	2.1
	Canyon	65	3.9	2.8	16	1.8
Waves	Smooth	35	11	1.1	-	5.1
	Ridge	35	9.4	1.1	41	4.4
	Canyon	35	9.2	1.2	37	4.3
Eddies	Smooth	35	4.3	2.9	-	2.0
	Ridge	35	4.3	2.9	19	2.0
	Canyon	35	3.1	3.5	13	1.5

Table 1: *Values of ambient water depth (D), source density difference ($\Delta\rho_0$) and derived parameters.*

kinematic viscosity of water, had to be smaller than the length of the slope (8 m); and 2) the source flow rate Q_0 had to be smaller than the transport capacity $Q_{C/R}$ of the corrugations (see Appendix). Table 1 shows the ambient water depth and the density difference used to obtain the three regimes, together with L_D, $Q_{C/R}$ and the Nof velocity

$$U_N = \frac{g'\alpha}{f}. \tag{2}$$

Bulk estimates of the plume velocity obtained from the videotapes show that the actual velocity was up to 30% smaller than U_N, as also observed by Adduce & Cendese (2007). Since no more accurate velocity measurements were performed, the Nof velocity is taken as representative for the plume.

For each regime three experiments were carried out using a smooth slope, a slope with a canyon, and a slope with a ridge, giving a total of 9 experiments. Each experiment lasted between 4 and 8 hours and ended as the dense source was turned off. Only data from the first 4 hours will be used here.

The conductivity sensors were calibrated regularly using water with a known salinity and temperature. In addition, the bottom and surface density and temperature were measured prior to and at the end of each experiment using an Anton Paar DMA35N handheld density meter.

3 Results

3.1 Smooth slope

As the dense fluid was released, it adjusted and deflected to the right under the effect of rotation. The dense plume flowed with an along-slope component due to rotation and a

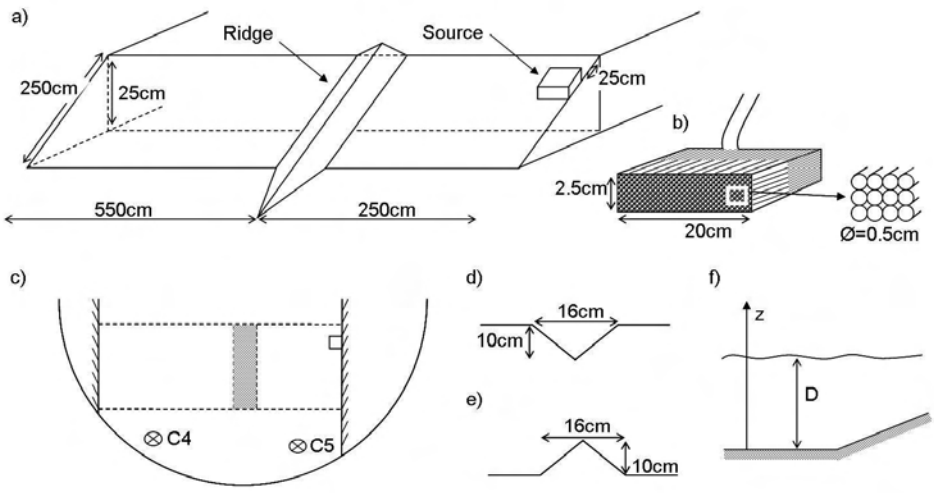

Figure 1: *Sketch of the experiment set-up (not to scale). a) Overview of the topography, b) dense source, c) top view. C4 and C5 mark the position of vertically profiling probes. Side view of d) the canyon, e) the ridge, and f) the shelf*

downslope component due to friction. The speed of the current was somewhat smaller than the Nof velocity, 2 - 5 cm/s, the current width increased from around 30 cm, close to the source, to a couple of meters far downstream, and the thickness of the current, H_p, varied from a few cm at the source to a few millimeters far downstream. In the laminar regime experiment (Fig. 2a), the dense fluid had a constant thickness and the interface between the dense current and the ambient fluid was sharp, indicative of little (or no) mixing. In the wave regime experiment (Fig. 2b), roll-waves developed at the interface between the dense and ambient fluid. Crests (darker color) and troughs (lighter color) can be seen in Fig. 2b. As the waves moved downslope, they grew in amplitude but they did not break in the three-dimensional fashion observed by Adduce & Cendese (2007). We expect that these non-breaking waves will cause a small amount of mixing between the light ambient fluid and the dense fluid, as observed by Adduce & Cendese (2007) and Cenedese et al. (2004). However, they will significantly increase the downslope transport as the speed of the wave fronts is 30-40% greater than the mean flow (Fer et al. 2001). Finally, in the eddy regime experiment (Fig. 2c), cyclonic eddies formed periodically in the water above the dense current and moved along-slope with a small across-slope velocity component. The dense current fluid below the eddies was observed to dome upwards due to the low pressure generated by the cyclonic eddies. In Fig. 2c the darker color represents the increased height of dense water in the dome structure. Possible mechanisms of eddy generation are described in Cenedese et al. (2004), Spall & Price (1998) and Lane-Serff & Baines (1998).

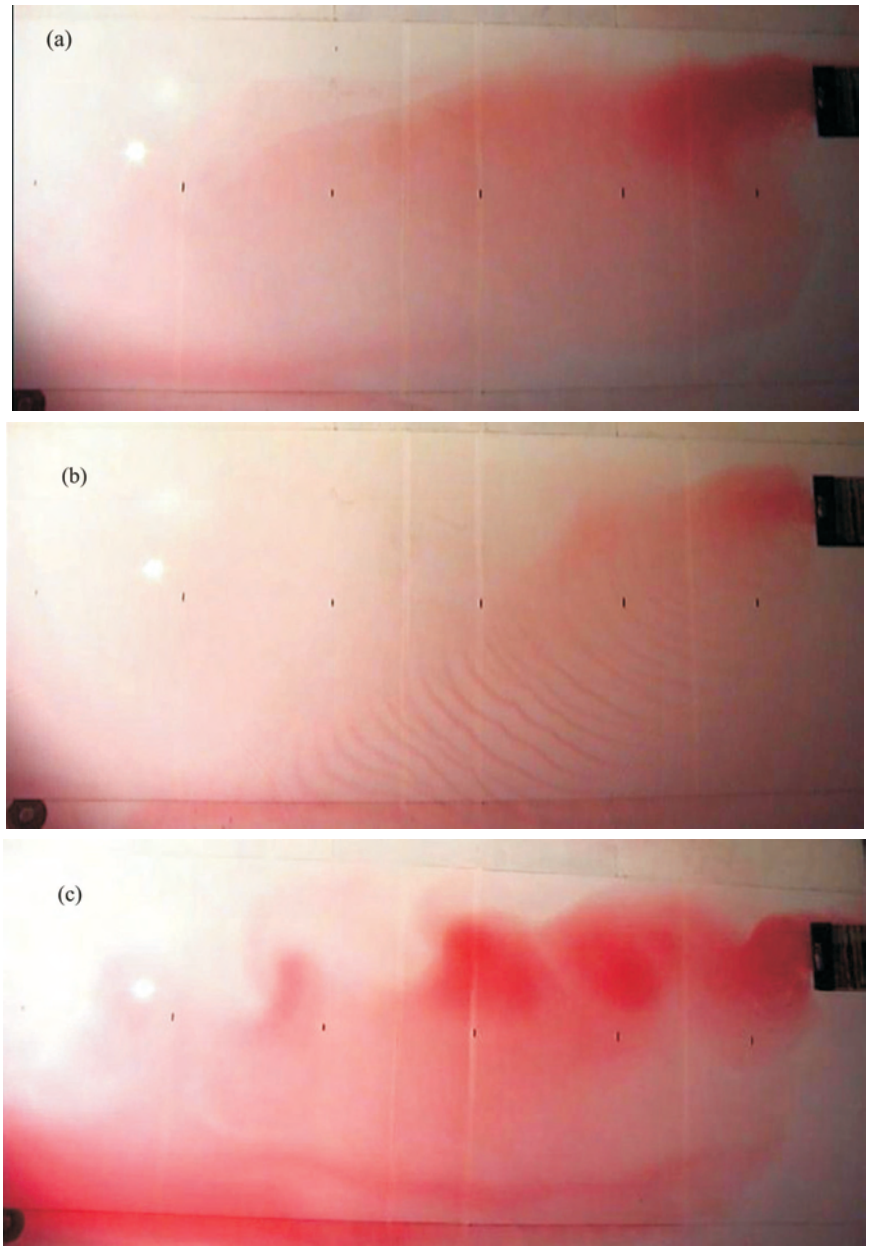

Figure 2: *Images from the three regimes of the smooth slope experiments. The black marks on the middle of the slope are 1 m apart. a) Laminar regime, b) Wave regime, c) Eddy regime. The color shift from weak on the left side to stronger on the right side may be partly due to the non-uniform illumination.*

3.2 Effect of topography

When a corrugation was present on the slope, it channeled the dense current downslope. The downslope flow induces an Ekman transport to the right, and if the downslope velocity is sufficiently large the frictional transport counteracts the geostrophic tendency to flow along the depth contours and out of the corrugation region (Wåhlin 2002). An analytical 1.5-layer model have been proposed, which gives the velocity and thickness of the plume as a function of the distance from the sloping canyon (Davies et al. 2006, Wåhlin 2002) or ridge center (Darelius & Wåhlin 2007). The model results have been shown to agree with laboratory experiments of V-shaped ridges and canyons (Darelius 2007, Davies et al. 2006). The analytical expressions for plume thickness, velocity, and transport capacity ($Q_{C/R}$), or the maximum amount of water that the corrugations used in the experiment can channel downslope, are given in the Appendix.

In the present experiments, the source flow Q_0 was smaller than $Q_{C/R}$ for all flows, and the entire plume is expected to be steered downslope by the corrugation. Fig. 3 shows top views of the three regimes in the presence of the ridge, and Fig. 4, of the canyon. The plume became narrower and thicker (the red color is darker) and it accelerated as it was deflected downslope. Waves and instabilities developed along the corrugation wall (Fig. 5), also in the laminar and eddy regimes.

The introduction of a corrugation on the slope influenced the eddies in the eddy regime. Fig. 6 shows the tracks of particles that were sprinkled on the free surface in order to monitor the motion of the ambient water. The particles moved with an anticlockwise motion while approaching the ridge. When the ridge was encountered the dense water seemed to be "released" from the upper water column, flowing downslope along the ridge, while the particles became close to stationary or moved up beyond the slope to where the bottom is flat. The same behavior was observed in the presence of the canyon (not shown here).

3.3 Salinity in the basin

Fig. 7 shows the salinity in the basin as a function of time and depth during the laminar experiment with smooth topography. Almost undiluted source water is deposited at the bottom of the basin in a thickening layer. Also inserted is a (dashed) line $h(t)$ showing the reference level, i.e. the thickness that the plume water layer would have had if there had been no mixing at all:

$$\int_0^{h(t)} A(z)dz = V(t) = \int_0^t Q(\xi)d\xi \tag{3}$$

where $A(z)$ is the basin area as a function of distance above bottom, $V(t)$ the volume of source fluid in the basin, and $Q(t)$ the source volume flux. In the present experiments, $A(z) = A_0 + \gamma z$ where $A_0 = 2$ m^2 and $\gamma = 4$ m, and $Q(t) = Q_0$ where $Q_0 = 10$ l/min.

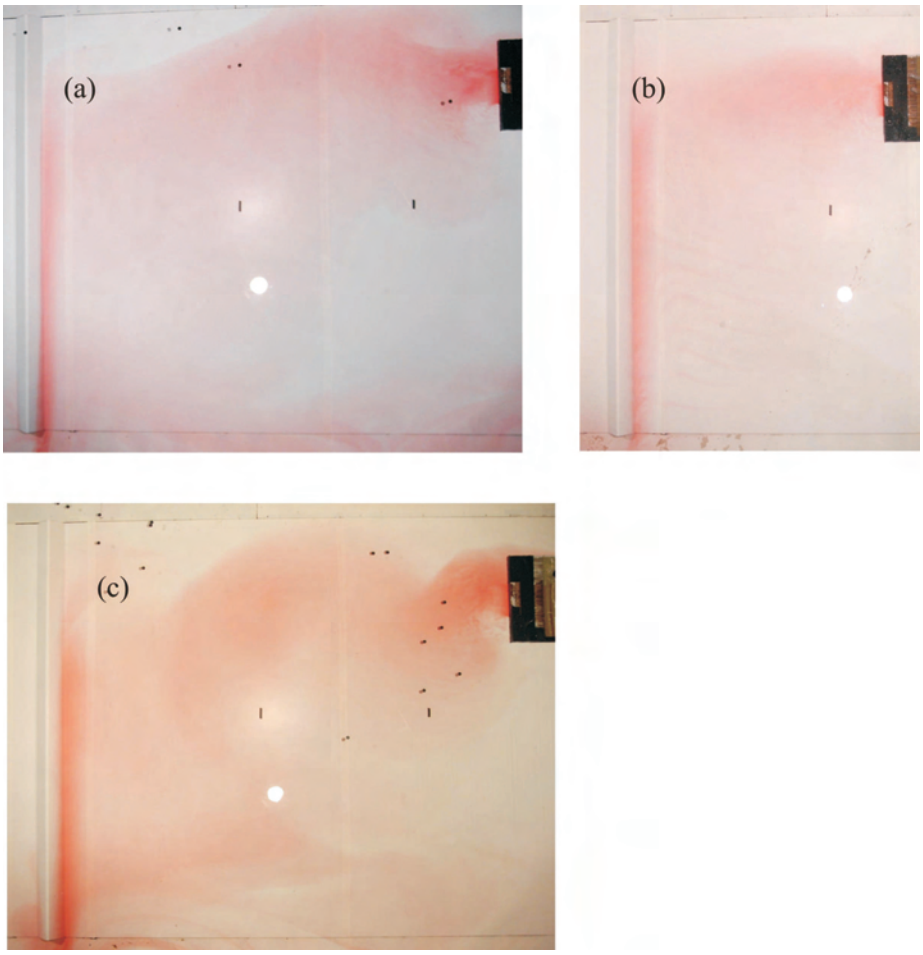

Figure 3: *Top view photographs of the flow with a ridge present on the slope. The black marks on the middle of the slope are 1 m apart. The scattered dots are black floats that were released in order to monitor motions in the ambient layer. a) Laminar regime, b) Wave regime, and c) Eddy regime. The source was moved closer to the ridge in the wave regime, from 2.5 m to 1.5 m, because otherwise the flow would have drained completely before it encountered the ridge.*

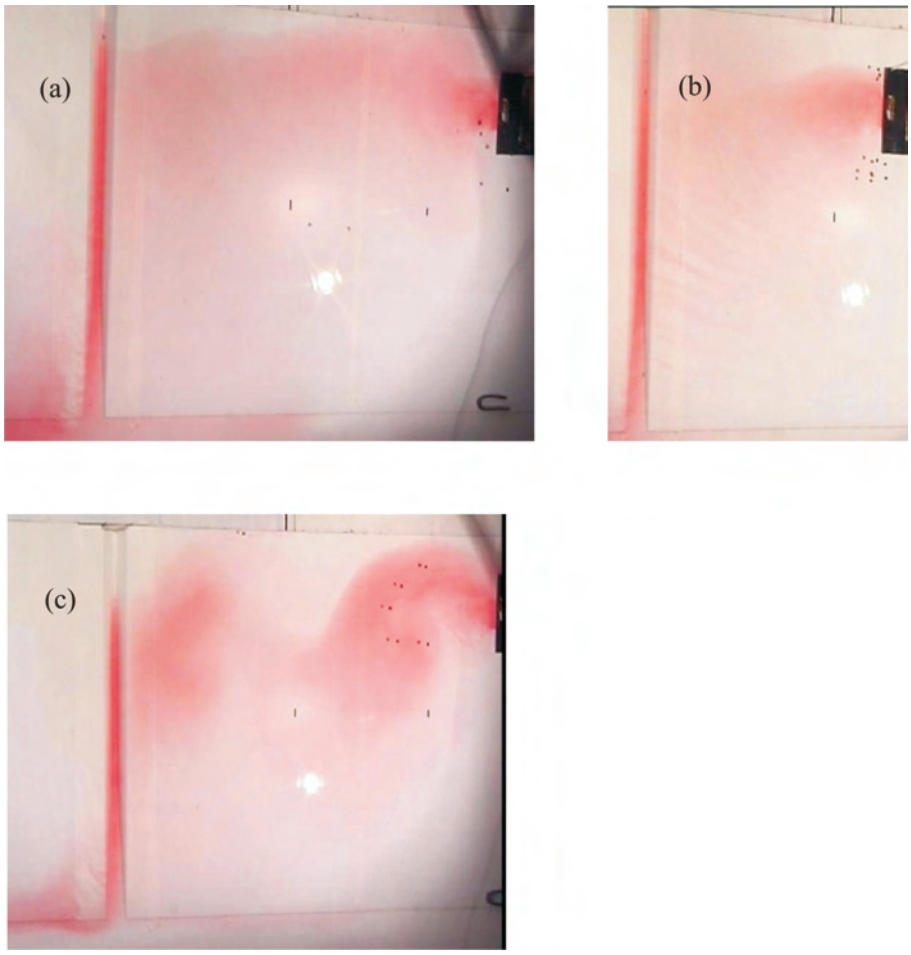

Figure 4: *Top view photographs of the flow with a canyon present on the slope. The black marks on the middle of the slope are 1 m apart. The scattered dots are black floats that were released in order to monitor motions in the ambient layer. a) Laminar regime, b) Wave regime, and c) Eddy regime. The source was moved closer to the canyon in the wave regime, from 2.5 m to 1.5 m, because otherwise the flow would have drained completely before it encountered the ridge.*

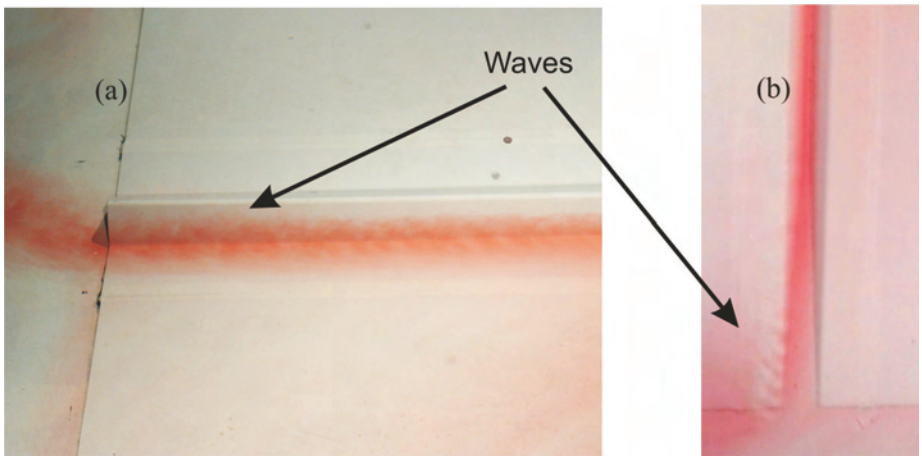

Figure 5: *Waves forming along the topography. a) ridge b) canyon.*

Inserting these expressions into (3) gives

$$h(t) = -\frac{A_0}{\gamma} + \sqrt{\frac{A_0^2}{\gamma^2} + 2\frac{Q_0 t}{\gamma}}. \tag{4}$$

There is a certain time-lag corresponding to the time it takes for the dense water to reach the sondes (the placement of the two sondes can be seen in Fig. 1c), and the curves have been shifted so that $t = 0$ when the plume first reaches the sonde. The dense interface oscillates, presumably because of waves that travel over the basin. Fig. 8 shows the same plot for the laminar experiment with a ridge. A larger volume of less dense water is found in the basin, indicating that more ambient fluid has been mixed into the plume compared with the experiment without ridge. This is also evident in Fig. 9, the laminar experiment with a canyon.

4 Mixing induced by the topographic features

The large size of the tank made it possible to avoid collision of the dense current with the wall at the end of the slope. The drainage length-scale, L_D (cf eq. (1)), was shorter than the length of the slope (8 m) for all three regimes (see Fig. 2 and Table 1), although the actual drainage length appears to be somewhat larger than (1). The dense water drained gradually downslope into the basin, or was channeled downslope by topography. Since the flow did not collide with the wall at the end of the slope, "artificial" mixing was minimized,

a)

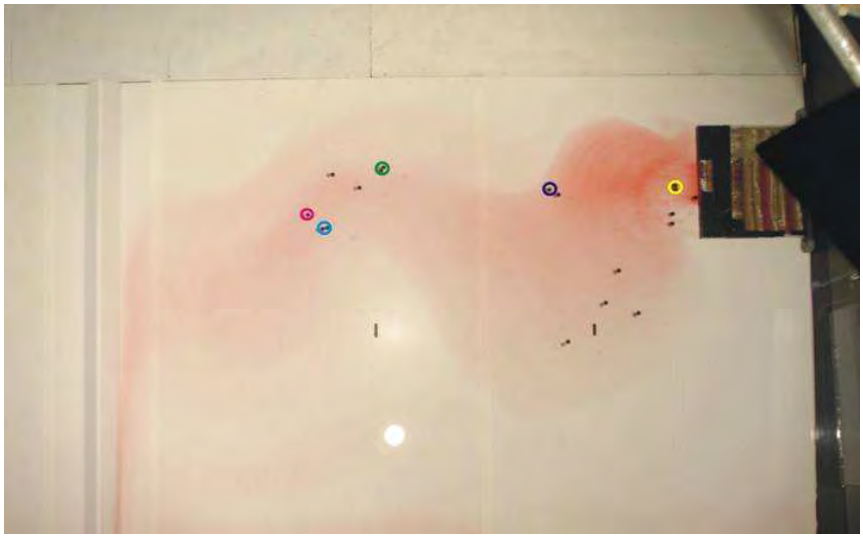

b)

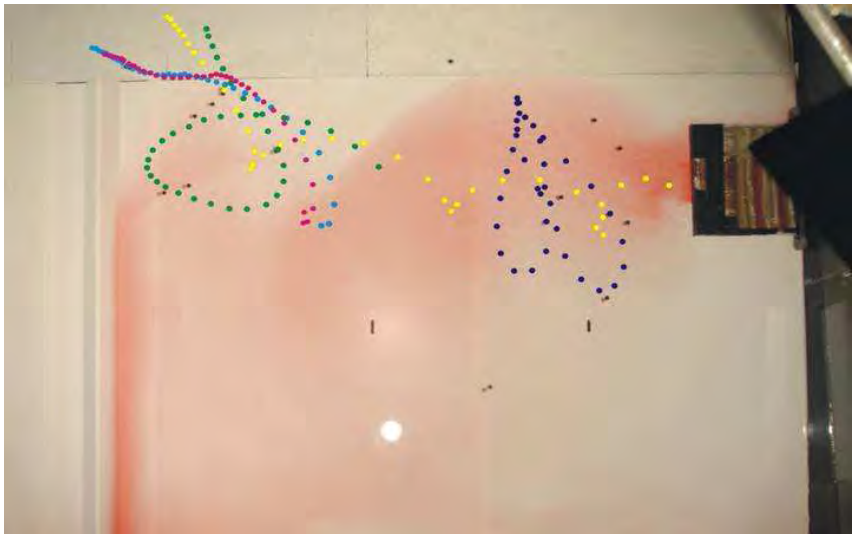

Figure 6: *Top view photographs of the flow in the eddy regime with a ridge present on the slope. The black dots are floats that were distributed on the surface. a) 140 min after experiment start. The colored circles mark floats that are traced in (b). b) 146 min after experiment start. The colored dots mark the positions of the floats in the time between (a) and (b), at interval 10 s.*

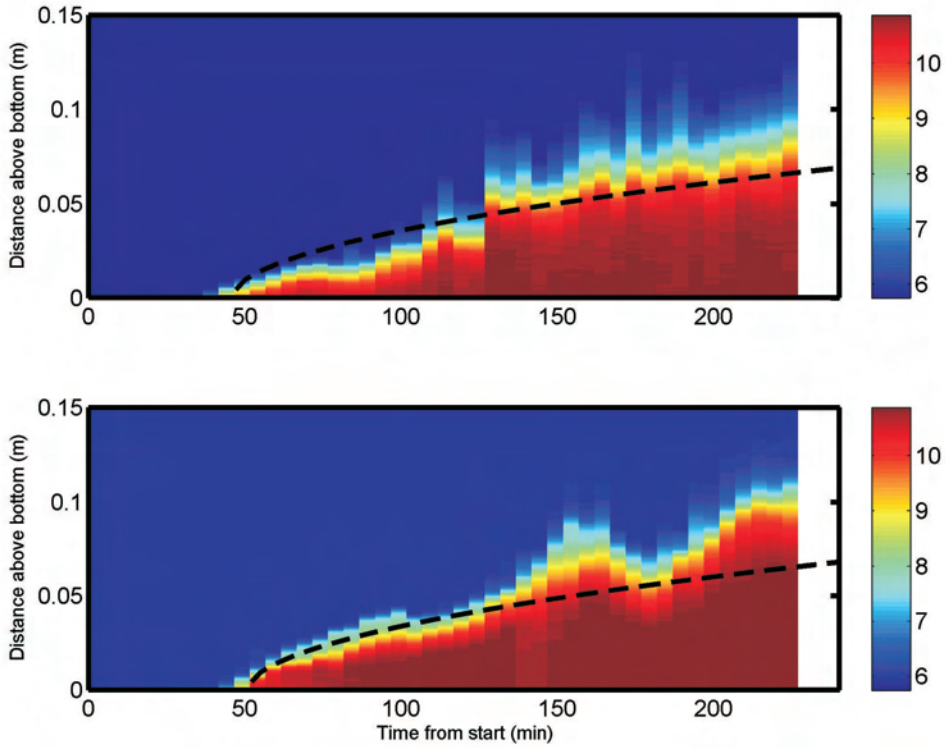

Figure 7: *Salinity as a function of time and distance above bottom (cm) for laminar experiment with smooth topography. Colors indicate salinity according to the colorbar, the scale has been adjusted so that red is pure source water (salinity 10.8) and blue is pure basin water (salinity 5.8). Top panel: Sonde C4. Lower panel: Sonde C5. Black dashed line shows the reference level at which the interface would be if there was no mixing between plume and ambient water. The curve has been shifted so that $t = 0$ at the time when the dense fluid first reaches the sonde.*

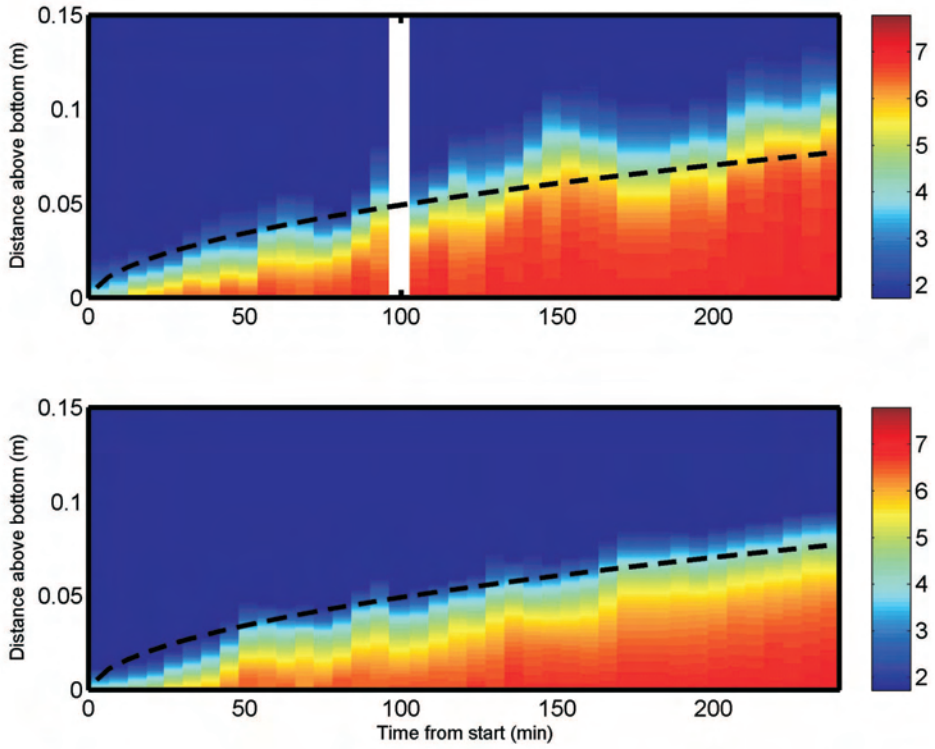

Figure 8: *Same as in Fig. 7, but for ridge topography. The color scale has been adjusted so that red is pure source water (salinity 7.7) and blue is pure basin water (salinity 1.8). Because of the presence of residual fluid in the basin from a previous experiment the black dashed line has not been shifted. The white areas indicate missing data.*

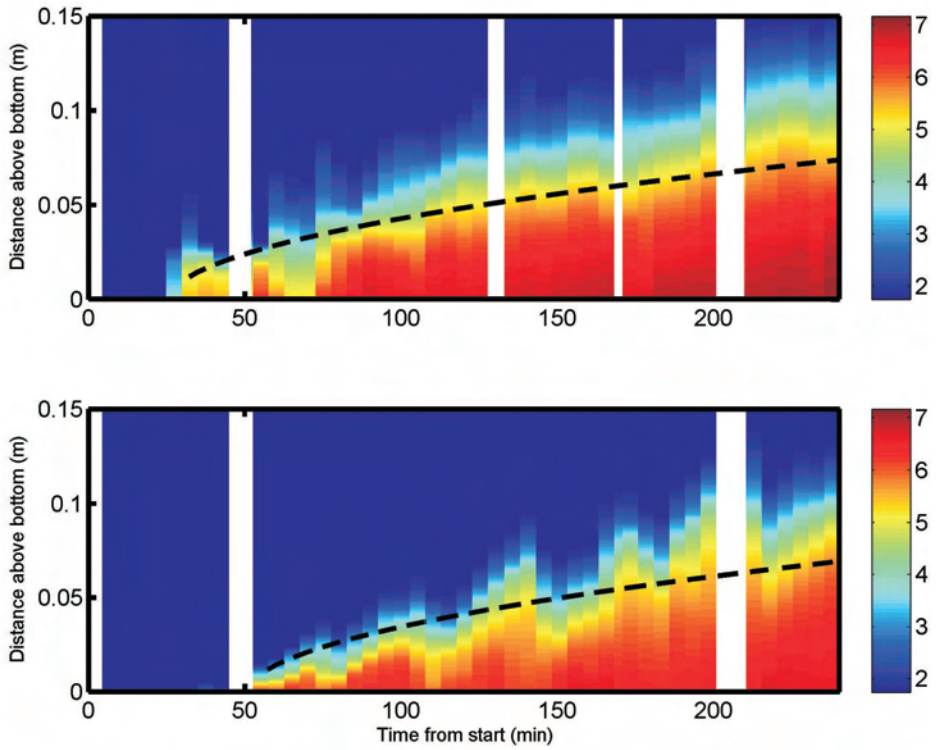

Figure 9: *Same as in Fig. 7 but for a canyon topography. The color scale has been adjusted so that red is pure source water (salinity 7.1) and blue is pure basin water (salinity 1.8). The white areas indicate missing data.*

and it is believed that the observed dilution of the source water was caused by entrainment processes on the slope itself. The measurements in the basin can thus be used to estimate the mixing in the plume. Because of the time variability, the time lag, and the difference between the two sondes, some caution is required when estimating the entrainment. Since the time lag is unknown the volume of plume water in the basin cannot be used to calculate the total entrainment. It can, however, be estimated from the dilution of the plume water in the basin. It is tempting to take the average of the two sondes and to low-pass filter the data in order to reduce the variability. Such a procedure "creates" artificial mixing since the profiles are smoothed compared with the original data. Instead a bulk mixing ratio, r_b, has been obtained, similarly to Cenedese et al. (2004). First, a mean plume density anomaly $\Delta\rho_P$ was calculated from the last profile at $t = t_f$, when $\rho(t_f, z) = \rho_F(z)$, using

$$\Delta\rho_P h_B = \int_0^D (\rho_F(z) - \rho_A) dz. \tag{5}$$

In the above, ρ_A is the ambient background density and h_B the thickness of the dense layer in the basin, defined as the level where the density first exceeded ρ_A by 0.001 kg/m^3 or more in the last profile. Next, r_B was calculated by dividing $\Delta\rho_P$ with the source density anomaly $\Delta\rho_0 = \rho_0 - \rho_A$, i.e. $r_B = \Delta\rho_P/\Delta\rho_0$.
Finally, the average of the mixing ratios from the two sondes was calculated. The results are shown in Table 2. No mixing gives $r_B = 1$, while $r_B = 0$ for complete mixing. The mixing ratio is smallest (indicating much mixing) for the wave regime and largest (indicating less mixing) for the laminar regime. The largest topography-induced decrease, over 50%, of the mixing ratio occurs for the laminar regime. The canyon and ridge mixing ratios are comparable in the laminar and wave regimes but somewhat larger in the eddy regime.

A bulk estimate of the total entrained transport, Q_E, is obtained from the expression $Q_E = Q_0(\frac{1}{r_B} - 1)$ (Cenedese et al. 2004). A mean value of the entrainment velocity w_E is then given by

$$w_E = \frac{Q_E}{A_P} \tag{6}$$

where A_P is the total surface area of the plume (see Table 2). Assuming that the plume velocity U is approximately equal to the Nof speed (2), the entrainment coefficient E, defined by $w_E = EU$, can be calculated using (5) and (2),

$$E = \frac{fQ_E}{g'\alpha A_P}. \tag{7}$$

The results are shown in Table 2. In order to compare the obtained E with previous studies a representative value of the Froude number Fr_B, $Fr_B = U_N/\sqrt{g'H_P}$, where H_P is the plume thickness, was estimated. The plume thickness varies between 2 cm at the source down to the Ekman layer thickness of 1.3 mm in the drainage layer, and these values gave

Regime	Topography	r_b	Q_E (l/min)	A_p (m^2)	E $\cdot 10^{-4}$	Fr_B	Fr_T
Laminar	Smooth	0.76	2.4	8.75	2.7	0.6-2.5	
	Ridge	0.63	3.7	6.75	4.4		4.7
	Canyon	0.60	4.0	6.75	5.4		4.9
Waves	Smooth	0.54	4.6	6.25	2.4	1.1-4.3	
	Ridge	0.50	5.1	3.25	5.9		6.4
	Canyon	0.44	5.6	3.25	6.7		6.9
Eddies	Smooth	0.70	3.0	14.4	1.7	0.7-2.7	
	Ridge	0.59	4.1	6.21	5.4		4.7
	Canyon	0.56	4.4	6.21	8.0		4.9

Table 2: *Mixing ratio (r_b), surface area (A_p) and entrainment coefficient (E) for the different regimes and topographies.*

Density class	r_b	Basin water (% of volume)
Basin water	<0.3	>70
Highly diluted source water	0.3-0.7	30-70
Moderately diluted source water	0.7-0.95	5-30
Pure source water	> 0.95	<5

Table 3: *Definition of the water masses studied in Figs 10-12.*

the upper and lower values of Fr_B quoted in Table 2. The obtained values for E and Fr_B conform qualitatively to those reported in Adduce & Cendese (2007), although it should be stressed that the uncertainties in the present experiments are large, in particular with regard to the Froude number.

All three regimes show evidence of increased mixing in the presence of a corrugation, probably induced by the waves and billows that were observed along the canyon wall (Fig. 5). Theoretical estimates of plume velocity and thickness in the vicinity of the corrugation can be used to estimate a topographic Froude number, Fr_T. This has been done (see Appendix), using the source density and spatial averages of the analytical model results for velocity and thickness. The results are shown in Table 2. The topographic Froude numbers are all larger than the slope values, Fr_B, which may explain the enhanced entrainment rates.

Fig. 7 - 9 show the stratification in the basin. The plume water was divided into four density classes defined by the mixing ratio between basin and source water (see Table 3). The volume of each density class in the basin could then be calculated from the vertical profiles. The results are shown in Fig. 10 - 12, which show the percentage of the volume (up to 30 cm depth) that each density class occupies as a function of time. There are no abrupt changes in the rate of increase of each density class, indicating that the mixing processes were constant during the experiments and that no regime shift occurred.

As expected, the volume of "pure" basin water decreases with time as it is replaced by plume water. In the laminar regime (Fig. 10) the experiments with a corrugation have a larger and more rapidly increasing volume of "highly diluted" (Fig. 10b) and "moderately diluted" (Fig. 10c) source water than the experiment with smooth topography. There is less "pure" source water in the experiments with a corrugation than with a smooth topography (Fig. 10d).

In the wave regime (Fig. 11) the mixing on the smooth slope is enhanced compared with the laminar regime (Fig. 10d and 11d). There is no "pure" source water in the basin in the wave regime (for any of the topographies), while there is so in the laminar regime. Fig. 11b and 11c show that the presence of a corrugation increased mixing; there is more "highly diluted" source water with a corrugation and more "moderately diluted" water with the

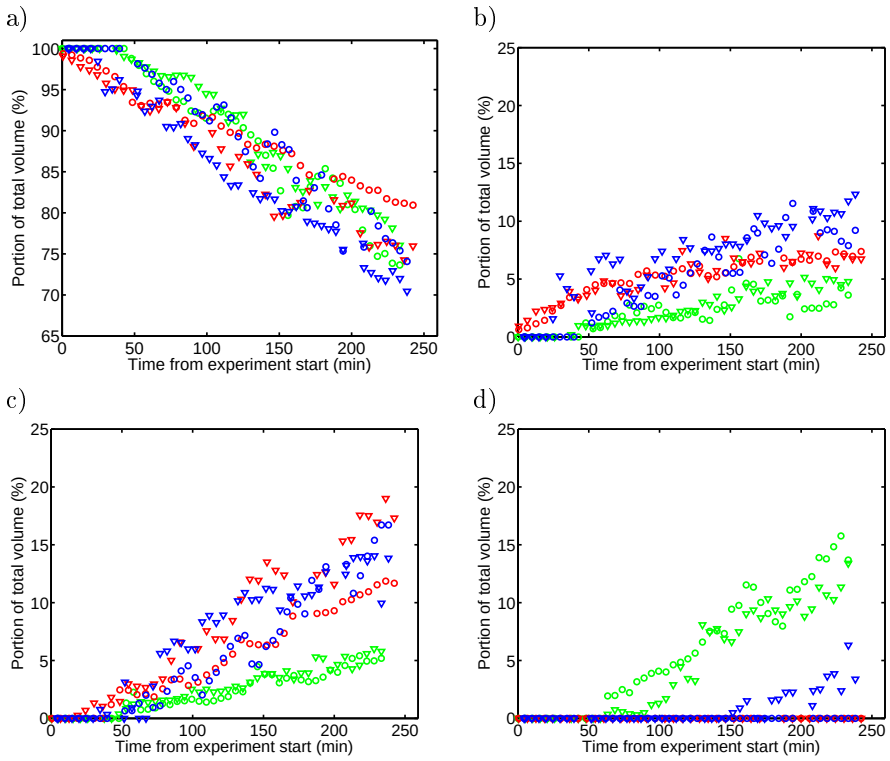

Figure 10: *Volume of water within the four density classes as a function of time. Data from the laminar experiments with smooth topography (green), ridge topography (red) and canyon topography (blue). Circles show data from C4, triangles data from C5. a) Basin water, b) Highly diluted source water, c) Moderately diluted source water, and d) Pure source water.*

smooth topography.

In the eddy regime (Fig. 12) the influence of the topography is not as clear. Fig. 12d shows that only small volumes of "pure" source water reached the basin when the canyon is present and Fig. 12c shows that there is somewhat more "moderately diluted" source water compared with the smooth topography. There is no clear difference between the topographies in the production of "highly diluted" source water.

In all regimes the canyon induces more mixing than the ridge, and as can be seen in Table 2, the canyon experiments has larger theoretical Froude numbers than the ridge experiments.

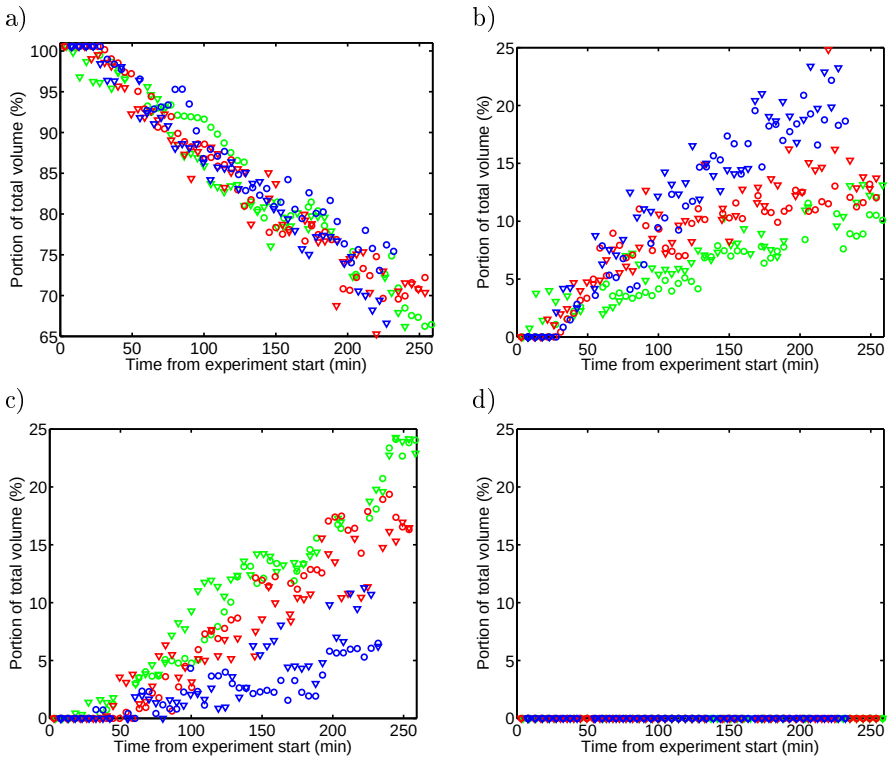

Figure 11: *Same as Fig. 10, but for the wave regime.*

The nine experiments show similar results for the two sondes, but there are certain differences. For example, it can be seen in Fig. 10c and 12c that the densest water is recorded by C5. This may be caused by Ekman drainage ahead of the corrugation transporting nearly undiluted source water down to the sonde.

5 Discussion

Experiments were conducted in three parameter regimes characterized by laminar flow (deep ambient water; small source density), waves (large source density), and eddies (shallow ambient water; small source density). The experiments displayed several properties that are in accordance with previous studies of dense plumes on sloping topography, and new observations of how a dense plume is affected by the presence of a ridge or a canyon. The laminar flow had a smooth dense layer that moved along the slope, while dense water continuously

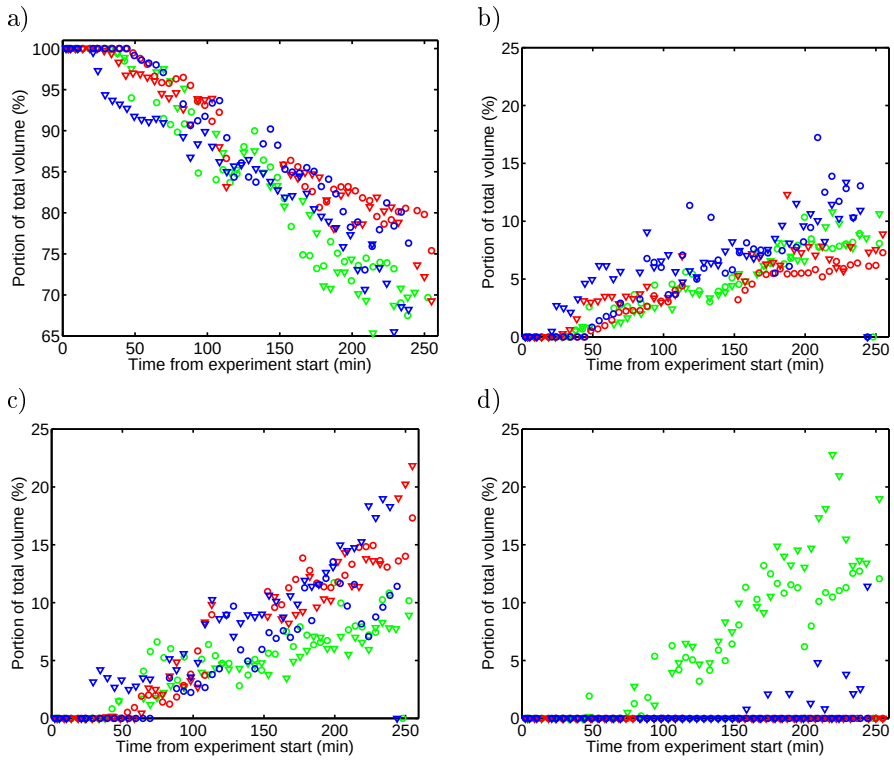

Figure 12: *Same as Fig. 10, but for the eddy regime.*

was drained downslope by Ekman transport through the lower edge. In the basin, a sharp interface separated a thickening layer of dense water from the ambient water, indicative of little mixing. The flow was similar to previous observations (e.g. Adduce & Cendese (2007), Cenedese et al. (2004), Lane-Serff & Baines (1998)). When a corrugation was placed on the slope, the dense water was steered downslope along it. The dense water accelerated, and waves developed. The mixing was enhanced compared with that observed with a smooth slope.

When the source density was increased, the flow switched into the roll-wave regime, and mixing increased. This is in accordance with findings in e.g. Adduce & Cendese (2007) and Cenedese et al. (2004). The layer of diluted plume water in the basin was separated from the ambient water by an interface that was less sharp than in the laminar experiment. With a corrugation in place, the dense water was steered downslope and waves were observed. These waves were similar in amplitude and wavelength to the roll-waves, but traveled down-

slope next to the corrugation, rather than at an angle along the slope. The basin water was somewhat more mixed compared with the experiment with no corrugation.

By decreasing the ambient fluid depth and/or increasing the source transport (not reported here) the flow switched into the eddy regime, and the plume broke up into a train of domes that were trapped underneath cyclonic eddies moving along the slope in the upper layer. The formation of eddies and the trapping of dense fluid was similar to previous observations by Cenedese et al. (2004) and Lane-Serff & Baines (1998). This regime was characterized by high variability and slightly increased mixing compared with the laminar flow. When a corrugation was introduced, the eddies first moved along the slope, but, as soon as they encountered the corrugation, they disintegrated or moved upslope beyond the slope to the flat bottom. The dense water trapped below the eddies was steered downslope next to the corrugation, as in the other two regimes. Growing waves were observed on the left hand side of the corrugations, and total mixing was increased in the presence of a corrugation. The increase in mixing ratio was smaller than that observed for the laminar flow.

The eddy results suggest that small-scale topography can act to separate and release dense water that is trapped underneath eddies in the upper layer, and even destroy the eddies themselves. The observations are in contrast to existing theories of vortex-drift induced by topography that predict an along-slope motion of the eddies (Jacob et al. 2002, Nof 1983). When an eddy has a strong barotropic component, such as ours, it is expected to have a downhill component in the drift (Jacob et al. 2002). However, existing theories have only been applied to topography with a length-scale larger than the eddy size, and laboratory studies pertaining to topography, which is smaller than or comparable to the eddy size, show that the eddies may instead split up and move around the obstacles (Adduce & Cenedese 2004, Wang & Dewar 2003). This may explain the upslope motion.

Bulk estimates of the entrainment coefficient and the Froude number for the smooth slope experiments conform qualitatively with previous experiments for flows on a smooth slope (Adduce & Cendese 2007, Cenedese et al. 2004). Bulk estimates of the entrainment coefficient show that the values obtained with a corrugation present on the slope have the same magnitude regardless of the regime of the large-scale current. The larger entrainment rate is compensated by a larger descent rate, i.e. by a shorter plume path, and the increase in the final mixing ratio of the product water is substantially smaller than the increase in E. Froude numbers were calculated, but the upper and lower estimates span a wide range. In the vicinity of the corrugation a theoretical plume thickness and velocity can be found (Darelius & Wåhlin 2007, Davies et al. 2006), assuming a first-order force balance between the pressure gradient, the Coriolis force and the frictional force. These predictions have been shown to agree with laboratory experiments (Darelius 2007, Davies et al. 2006), and imply supercritical flow in the vicinity of the corrugation for all of the present experiments. The results suggest that it is the small-scale topography that determines the mixing properties of the plume, rather than the large-scale characteristics of the plume.

Enhanced mixing caused by tidal flow over submarine canyons has previously been observed e.g. on the Mid-Atlantic Ridge (see e.g. Ledwell et al. (2000), and in the laboratory (Wells & Helfrich 2006). The mixing process studied is not driven by tides but by the plume water's release of potential energy as it flows downhill. The results suggest that the presence of corrugations will reduce basin density and stratification. There are no models available that capture these small-scale processes and which are simple enough to be used in a subgrid parameterization of dense overflows or process studies of density driven circulations.

Data from the Filchner Outflow, Antarctica, show evidence of acceleration of the plume as it is steered downslope by a ridge in the region (Foldvik et al. 2004), although no measurements of mixing have been performed. Somewhat contradictory to the results presented here, almost undiluted plume water is occasionally observed to flow downslope with relatively high speed (up to 1 m/s) in the vicinity of the ridge at 2100 m depth. More field data is needed to assess whether topographic steering of dense water is indeed an agent that is of importance to ocean stratification.

Acknowledgements Expert technical assistance and scientific discussions with H. Didelle, S. Viboud, J. Buck, J. Sommeria, L.H. Smedsrud and A. Engqvuist are highly valued. AW was funded by the Swedish Research Council and ED in part by Meltzer Stiftelsen, for which we are grateful. The work described in this publication was supported by the European Community's Sixth Framework Programme through the grant to the budget of the Integrated Infrastructure Initiative HYDRALAB III, Contract no. 022441 (RII3).

References

Adduce, C. & Cenedese, C. (2004), 'An experimental study of a mesoscale vortex colliding with topography of varying geometry in a rotating fluid', *Journal of Marine Research* **62**(5), 611–638.

Adduce, C. & Cendese, C. (2007), 'Mixing in a density driven current down a slope in a rotating fluid', *Journal of Fluid Mechanics* (submitted).

Baines, P. G. (2001), 'Mixing in flows down gentle slopes into stratified environments', *Journal of Fluid Mechanics* **443**, 237–270.

Baines, P. G. (2005), 'Mixing regimes for the flow of dense fluid down slopes into stratified environments', *Journal of Fluid Mechanics* **538**, 245–267.

Baines, W. D. & Turner, J. S. (1969), 'Turbulent buoyant convection from a source in a confined region', *Journal of Fluid Mechanics* **37**.

Baines, P. G. & Condie, S. (1998), Observations and modelling of antarctic downslope flows: a review, *in* S. S. Jacobs & R. F. Weiss, eds, 'Ocean, Ice, and Atmosphere - Interaction at the Antarctic Continental Margin', Vol. 75, AGU, Washington D.C.

Cenedese, C., Whitehead, J. A., Ascarelli, T. A. & Ohiwa, M. (2004), 'A dense current flowing down a sloping bottom in a rotating fluid', *Journal of Physical Oceanography* **34**(1), 188–203.

Chang, Y. S., Xu, X. B., Ozgokmen, T. M., Chassignet, E. P., Peters, H. & Fischer, P. F. (2005), 'Comparison of gravity current mixing parameterizations and calibration using a high-resolution 3D nonhydrostatic spectral element model', *Ocean Modelling* **10**(3-4), 342–368.

Darelius, E. (2007), 'Topographic steering of dense overflow plumes: laboratory experiments with V-shaped canyons and ridges', *Manuscript*.

Darelius, E. & Wåhlin, A. (2007), 'Downward flow of dense water leaning on a submarine ridge', *Deep Sea Research* **56**(7), 1173–1188.

Darelius, E., Smedsrud, L., Østerhus, S., Foldvik, A. & Gammelsrød, T. (2007), 'On the structure and variability of the Filchner Overflow plume', (Manuscript).

Davies, P., Wåhlin, A. & Guo, Y. (2006), 'Laboratory and analytical model studies of the FBC deep water outflow', *Journal of Physical Oceanography* **36**(7), 1348–1364.

Ellison, T. H. & Turner, J. S. (1959), 'Turbulent entrainment in stratified flows', *Journal of Fluid Mechanics* **6**(3), 423–448.

Fer, I., Lemmin, U. & Thorpe, S. A. (2001), 'Cascading of water down the sloping sides of a deep lake in winter', *Geophysical Research Letters* **28**(10), 2093–2096.

Fer, I., Lemmin, U. & Thorpe, S. A. (2002), 'Observations of mixing near the sides of a deep lake in winter', *Limnology and Oceanography* **47**(2), 535–544.

Foldvik, A., Gammelsrød, T., Østerhus, S., Fahrbach, E., Rohardt, G., Schrøder, M., Nicholls, K. W., Padman, L. & Woodgate, R. A. (2004), 'Ice shelf water overflow and bottom water formation in the southern Weddell Sea', *Journal of Geophysical Research-Oceans* **109**(C2).

Girton, J. B. & Sanford, T. B. (2003), 'Descent and modification of the overflow plume in the Denmark Strait', *Journal of Physical Oceanography* **33**(7), 1351–1364.

Hughes, G. O. & Griffiths, R. W. (2006), 'A simple convective model of the global overturning circulation, including effects of entrainment into sinking regions', *Ocean Modelling* **12**, 46–97.

Jacob, J. P., Chassignet, E. P. & Dewar, W. K. (2002), 'Influence of topography on the propagation of isolated eddies', *Journal of Physical Oceanography* **32**(10), 2848–2869.

Jiang, L. & Garwood, R. W. (1998), 'Effects of topographic steering and ambient stratification on overflows on continental slopes: a model study', *Journal of Geophysical Research-Oceans* **103**(C3), 5459–5476.

Kämpf, J. (2000), 'Impact of multiple submarine channels on the descent of dense water at high latitudes', *Journal of Geophysical Research-Oceans* **105**(C4), 8753–8773.

Kämpf, J. (2005), 'Cascading-driven upwelling in submarine canyons at high latitudes', *Journal of Geophysical Research-Oceans* **110**(C2).

Lane-Serff, G. F. & Baines, P. G. (1998), 'Eddy formation by dense flows on slopes in a rotating fluid', *Journal of Fluid Mechanics* **363**, 229–252.

Ledwell, J. R., Montgomery, E. T., Polzin, K. L., St Laurent, L. C., Schmitt, R. W. & Toole, J. M. (2000), 'Evidence for enhanced mixing over rough topography in the abyssal ocean', *Nature* **403**(6766), 179–182.

Nof, D. (1983), 'The translation of isolated cold eddies on a sloping bottom', *Deep-Sea Research Part A-Oceanographic Research Papers* **30**(2), 171–182.

Price, J. & Baringer, M. (1994), 'Outflows and deep-water production by marginal seas', *Progress in Oceanography* **33**(3), 161–200.

Sherwin, T. J. & Turrell, W. R. (2005), 'Mixing and advection of a cold water cascade over the Wyville Thomson Ridge', *Deep-Sea Research Part I-Oceanographic Research Papers* **52**(8), 1392–1413.

Sherwin, T., Griffiths, C., Inall, M. & Turrell, W. (2007), 'Quantifying the overflow across the Wyville Thomson Ridge into the Rockall Trough', *Deep Sea Research* (submitted).

Smith, P. C. (1975), 'A streamtube model for bottom boundary currents in the ocean', *Deep Sea Research* **22**.

Spall, M. A. & Price, J. F. (1998), 'Mesoscale variability in Denmark Strait: The PV outflow hypothesis', *Journal of Physical Oceanography* **28**(8), 1598–1623.

Vilibic, I., Grbec, B. & Supic, N. (2004), 'Dense water generation in the north adriatic in 1999 and its recirculation along the Jabuka Pit', *Deep-Sea Research Part I-Oceanographic Research Papers* **51**(11), 1457–1474.

Wåhlin, A. K. (2002), 'Topographic steering of dense currents with application to submarine canyons', *Deep-Sea Research Part I-Oceanographic Research Papers* **49**(2), 305–320.

Wåhlin, A. K. & Cenedese, C. (2006), 'How entraining density currents influence the stratification in a one-dimensional ocean basin', *Deep-Sea Research Part II-Topical Studies In Oceanography* **53**(1-2), 172–193.

Wang, G. H. & Dewar, W. K. (2003), 'Meddy-seamount interactions: Implications for the Mediterranean salt tongue', *Journal of Physical Oceanography* **33**(11), 2446–2461.

Wells, M. G. & Wettlaufer, J. S. (2005), 'Two-dimensional density currents in a confined basin', *Geophysical And Astrophysical Fluid Dynamics* **99**(3), 199–218.

Wells, J. R. & Helfrich, K. R. (2006), 'Mixing at the head of a canyon: a laboratory investigation of fluid exchanges in a rotating, stratified basin', *Journal of Geophysical Research-Oceans* **111**(C12).

APPENDIX

A Theory: Topographically steered flows

Flow in a linear canyon was considered in Davies et al. (2006), but the expressions presented here follows the derivation in Darelius & Wåhlin (2007). Fig. 13 shows a sketch of the canyon flow, with the dense interface given by the analytical model (Darelius & Wåhlin 2007, Davies et al. 2006, Wåhlin 2002), i.e.

$$h(y)+D(y)=\begin{cases} H_0\left[\left(-\frac{1}{\gamma}+\frac{2}{\gamma}e^{\gamma}\right)e^{\gamma y/W}-\frac{1}{\gamma}\right] & W\cdot Y_L\le y<-W \\ H_0\left[-\frac{1}{\gamma}e^{\gamma y/W}+\frac{1}{\gamma}\right] & -W\le y\le 0 \end{cases}. \tag{8}$$

In the above $D(y)$ is the bottom elevation, $h(y)$ is the thickness of the dense layer, $\gamma = sW/\delta$, s is the slope of the canyon axis, W is half of the effective width of the canyon, $\delta=\sqrt{2\nu/f}$ the thickness of the Ekman layer, $Y_L=\frac{1}{\gamma}\ln\left(\frac{1}{2e^{\gamma}-1}\right)$ is the position where the dense layer intersects the left wall and H_0 is the height to which the layer climbs on the wall. The geometrical definitions are shown in Fig. 13.

Similarly, the position of the interface for flow leaning on a linear ridge is given by

$$h(y)+D(y)=\begin{cases} H_0\left(\frac{1}{\gamma}\left[e^{-\gamma}-1\right]\right)e^{\gamma y/W} & y\le -W \\ \frac{H_0}{\gamma}\left(1-e^{\gamma y/W}\right) & -W<y<0 \\ 0 & y\ge 0 \end{cases}. \tag{9}$$

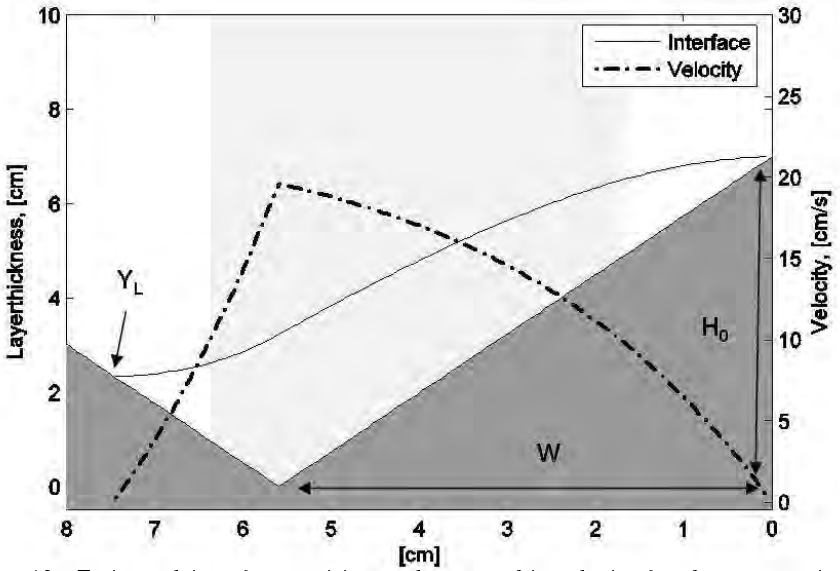

Figure 13: *Estimated interface position and geostrophic velocity for the wave regime. The grey shading indicates the area from which values are used in the calculation of mean thickness and velocity.*

The maximum downslope flow, Q_C, that can be supported by the corrugation is obtained when the corrugation is completely 'filled', i.e. when H_0 equals the height (depth) of the ridge (canyon) and W its width. The geostrophic transport is given by

$$Q_G = \int_{-\infty}^{\infty} h\,(y)\,u_G\,(y)dy \tag{10}$$

where u_G is the geostrophic velocity along the corrugation. Using (8) and (9) in (10) gives Q_C for the canyon,

$$Q_C = \frac{g'}{f} H_C^2 \frac{1}{\gamma_C^2}(2e^{-\gamma_C} - 2 + \ln(2e^{\gamma_C} - 1)) \tag{11}$$

where H_C is the canyon depth, $\gamma_C = sW_C/\delta$ and W_C is the canyon width. For the ridge we have

$$Q_R = \frac{g'}{f} H_R^2 \frac{1}{\gamma_R^2}(\gamma_R - 1 + e^{-\gamma_R}) \tag{12}$$

where H_R is the ridge height, $\gamma_R = sW_R/\delta$ and W_R is the ridge width. Using the kinematic viscosity of water $\nu = 10^{-6}$ m^2/s and $f = 0.21$ s^{-1} gives $\delta = 13$ mm. With the experiment

Topography	g' (m/s^2)	$H_0^\dagger$ (cm)	$\bar{h}^\dagger$ (cm)	$\bar{u}^\dagger$ (cm/s)	Fr_T
Ridge	0.04	5.9	2.4	14	4.7
	0.10	3.4	1.7	26	6.4
Canyon	0.04	7.0	2.5	15	4.9
	0.10	4.4	2.0	31	6.9

Table 4: *Interface height (H_0), mean height and velocity ($\bar{h}$, $\bar{u}$) and the estimated Froude number (Fr_T) for the experiments with topography. Parameters marked with † are derived from the analytical model.*

geometry, $H_C = 10$ cm, $W_C = 8$ cm and $s = 0.1$, this gives $\gamma = 5.2$ and a transport capacity $Q_C = 0.0014g'/f$ for the canyon and $Q_R = 0.0016g'/f$ for the ridge, which when evaluated with the appropriate g' and f gives the values quoted in Table 4.

The obtained transport capacities for the corrugations are larger than the source volume flux for all experiments, and as expected all the water in the plume was steered downslope by the corrugation. To obtain the theoretical plume thickness and velocity in the topographically steered flow, H_0 was found through iteration using the source flux, $Q_0 = 10$ l/min, and the transport capacity $Q_{C/R}$. The results are listed in Table 4. Fig. 13 shows the estimated position of the interface and the velocity for the wave regime.

The Froude number, Fr, can be written as

$$Fr = \frac{u}{\sqrt{g'h}} \tag{13}$$

where U and h are the velocity and the thickness of the dense layer and g' is the reduced gravity. For each experiment the theoretical Froude number, Fr_T, was calculated using the lateral mean values of the theoretical layer thickness, $\bar{h}$, and the velocity, $\bar{u}$. In order to obtain a representative mean value this was calculated in the area where $h > 0.5h_{max}$, where h_{max} is the maximum thickness of the dense layer (the area is shaded in Fig. 13). The results are presented in Table 4.

On the Structure and the Variability of the Filchner Overflow Plume

E. Darelius [1,2], ***L.H. Smedsrud*** [2], ***S. Østerhus*** [2], ***A. Foldvik*** [1], ***& T. Gammelsrød*** [1]

(1) Geophysical Institute, University of Bergen, Norway

(2) Bjerknes Centre for Climate Research, Bergen, Norway

Abstract

The Weddell Sea is one of the major generation sites for Antarctic Bottom Water. The cold and dense Ice Shelf Water that is formed under the Filchner-Ronne Ice Shelf is a precursor to the Antarctic Bottom Water, and it exits the ice-shelf cavity through the Filchner Depression forming a dense plume on the continental slope. Ice Shelf Water spills over the sill at a rate of 1.6 Sv (Foldvik et al. 2004). Properties of the dense plume are described using data from all available current meter records and CTD-stations in the region, focusing mainly on meso-scale variability and three distinct oscillations that have periods of about 35 hours, 3 days and 6 days. The oscillations are close to barotropic and are seen in both temperature and velocity records. The observations are compared with theories on eddies generated in overflow plumes and on continental shelf waves, but none of them seems to describe well the phenomena observed.

Twenty-five years of CTD data (more than 300 profiles) were synthesized to give a "mean-picture" of bottom temperature and plume thickness. Low temperatures and relatively thin layers of dense plume water are observed at great depth in the vicinity of a ridge, while profiles west of the ridge show higher temperatures and thicker layers. The three pathways suggested by Foldvik et al. (2004) are coupled to theories on topographic steering by canyons and ridges and discussed in relation to the presented data.

1 Introduction

Deep water formation at high latitudes is an important part of the thermohaline circulation, and has a central role in discussions of climate change. The Weddell Sea is traditionally thought to be the largest source of bottom water in the southern hemisphere (Orsi et al. 1999, Foldvik & Gammelsrød 1988, Deacon 1937), although rates and formation areas are a matter of debate (Schlitzer 2007, Fahrbach et al. 2001, Broecker et al. 1998). The distribution of bottom temperature and oxygen content around Antarctica show, however, that the coldest and most oxygen-rich water has its source in the Weddell Sea region (Orsi & Whitworth 2004, Deacon 1937), but dense water is also formed in the Ross Sea (Gordon

et al. 2004) and off the Adélie coast. Part of the deep water "raw-material" in the Weddell Sea is formed as the ocean interacts with the Filchner-Ronne Ice Shelf (FRIS) in the south-western Weddell Sea. The water mass, often referred to as Ice Shelf Water (ISW), has a temperature lower than the surface freezing point and is formed as a result of the depression of the freezing point with increasing pressure.

Cold and saline shelf water formed on the relatively shallow and wide continental shelves during winter enters and fills the FRIS cavity through the Ronne Depression in the west and from the Berkner Bank further east (Nicholls et al. 2001). The shelf water, although at its surface freezing point (-1.9°C), is, at depth, warmer than the *in situ* freezing point, and it can thus be cooled further as its available heat is given off to warm and melt the cold glacial ice with which it is in contact. The cooled shelf water mixes with the glacial meltwater, and the resulting water mass is less dense than its origin and tends to rise along the shelf (see e.g. Nøst & Foldvik (1994)). Frazil ice formation is initiated within the rising plume as it becomes supercooled due to the increase in its *in situ* freezing point (Smedsrud & Jenkins 2004, Dieckmann et al. 1986, Foldvik & Kvinge 1974). The ice crystals rise and settle under the ice shelf forming a layer of marine ice, and the salinity of the water increases again. The ISW is colder and slightly fresher than the original water mass, and it escapes the cavity through the Filchner Depression as a subsurface northward flow. Spilling over the sill, it turns left due to the Earth's rotation, and forms a gravity driven plume on the continental slope (Foldvik et al. 2004). The ISW plume mixes with the overlying Weddell Deep Water (WDW) to form Weddell Sea Bottom Water (WSBW) and eventually Antarctic Bottom Water (AABW).

The plume of Ice Shelf Water exiting from the Filchner-Ronne Ice Shelf through the Filchner Depression was first observed in 1977 by Foldvik et al. (1985*a,b*). Since then, a number of mooring arrays have been placed on the slope and in the Filchner Depression proper in order to monitor the flow. The data were synthesized by Foldvik et al. (2004) who estimated the flux of ISW to be 1.6±0.5 Sv, corresponding to a WSBW formation rate of 4.3±1.4 Sv. They further suggested that the ISW plume follows three main pathways down the slope, and concluded that two prominent ridges crosscutting the shelf slope influence the flow of the cold plume water. Laboratory experiments (Darelius 2007, Wåhlin et al. 2007) have shown that ridges (and canyons) can effectively steer plume water downslope and a theoretical framework for such topographically steered flows has been presented by Darelius (2007) and Wåhlin (2002).

Greatly simplified, one would expect the dense water spilling over the sill of the Filchner Depression to adjust geostrophically and to flow along the isobaths, with the (upslope) Coriolis force balancing the (downslope) pressure force. Friction would slow down the flow and cause it to deflect slightly downslope (Killworth 2001). Dense fluid would constantly be drained downslope from the lower part of the plume through Ekman drainage (Wåhlin & Walin 2001). However, most laboratory and model experiments indicate that this picture is

too simple. Eddies, waves and subplumes may develop that greatly alter the shape and the velocity patterns of the plume (Ezer 2006, Cenedese et al. 2004, Jungclaus et al. 2001, Etling et al. 2000, Lane-Serff & Baines 1998, Jiang & Garwood 1996, Smith 1977). Observations from overflow regions indicate that eddies or waves are formed in the ocean (see e.g. Geyer et al. (2006), Käse et al. (2003) and Høyer & Quadfasel (2001) for evidence from the Faroe Bank Overflow and Denmark Strait), and it will be shown here that, as suggested by Foldvik et al. (2004), such disturbances are probably generated within the Filchner Overflow.

Mesoscale features, like eddies and waves, impact mixing processes (Adduce & Cendese 2007, Wåhlin et al. 2007, Cenedese et al. 2004, Jiang & Garwood 1996) and descent rates (Tanaka & Akitomo 2001) and they will thus influence the final properties and destiny of the plume water. These processes determine, to some extent, the composition of the water masses found in the deep oceans and therefore the characteristics of large scale circulation (Willebrand et al. 2001). An understanding of these processes - and a correct representation of them in climate models - is a necessity if one seeks to understand and predict our future climate (Saunders 2001).

We revisit and discuss the Filchner area and the Filchner plume, focusing on meso-scale variability. A surprisingly large variability is found that cannot satisfactorily be explained by existing theory. A description of the general plume structure, water properties and pathways is included.

2 Data and Methods

This work is based primarily on data from 20 current meter moorings that were deployed in the Filchner Overflow area between 1968 and 1999. An overview of deployments, instruments and data records is given by Foldvik et al. (2004). Fig. 1 shows the position of the moorings and the mean current from the bottom-most instrument at each mooring (Foldvik et al. 2004). A total of 44 Aanderaa current meters (models RCM 4/5 and 7/8) was used, recording current (speed and direction) and temperature data. The instruments were placed from 10 to 433 m above bottom (mab) and moorings on the slope recorded data once every hour. The accuracy for an individual speed and direction measurement is ± 1 cm/s and $\pm 5^\circ$ respectively, according to the manufacturer. For low speeds (<1 cm/s) systematic errors might occur, but the velocities in the discussed time series are always well above this threshold. The record length varies from 15 to 837 days, but is about one year for most instruments. The F1-4 moorings (see Fig. 1) were equipped with Seabird MicroCat (SBE-37) conductivity-temperature sensors in addition to the current meters. These were placed 9 mab, and they have an accuracy of $<0.01^\circ$C for temperature and <0.004 S/m for conductivity, according to the manufacturer.

To facilitate comparison between records, the local coordinate system was rotated in

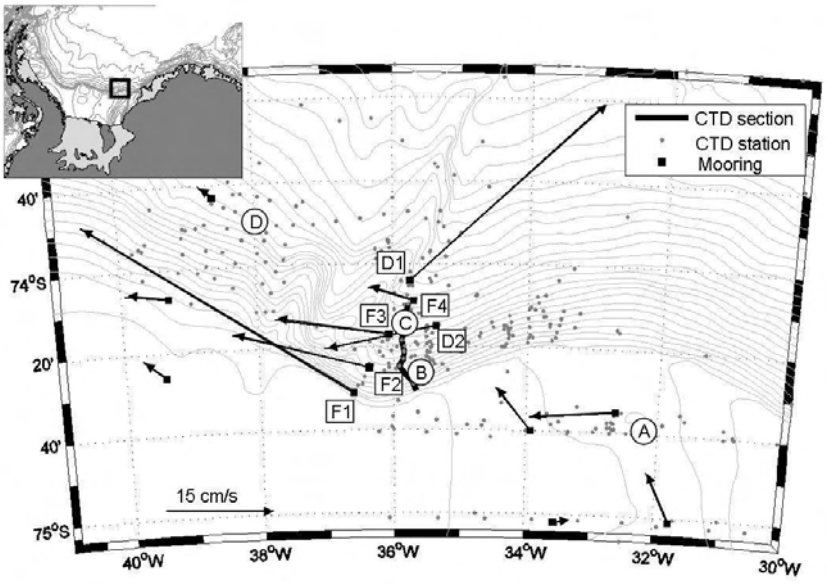

Figure 1: *Map of the study area showing bathymetry and mooring and CTD positions. The arrows indicate the mean current (from Foldvik et al (2004)) at the bottom-most instrument on each mooring. A, B, C and D show the location of the CTD-profiles discussed in the text.*

order to align the x-axis with the isobaths. u is thus always directed along and v across the slope.

Analysis of the current meter data revealed variability and oscillations. Fourier analysis was used to identify energy-containing frequencies. Eight Hanning windows with 50% overlap were used in the Fourier analysis (i.e. the length of each window is 2/9 x L, where L is the length of the time-series). The results from the Fourier analysis are presented in variance-preserving diagrams. The data were not de-tided prior to the analysis, but tidal frequencies (diurnal and semi-diurnal) are not presented. In addition to "normal" Fourier analysis on the u and v components of the flow, a rotational Fourier analysis was performed. An oscillation can be divided into a clockwise (CW) and a counter-clockwise (CCW) part, and the analysis identifies energy-containing frequencies in the two rotation directions. It should be noted, and it will be commented on in the discussion, that it is the rotation of the velocity vector locally that is obtained through this analysis, and not that of the large-scale motion.

Wavelet analysis (Torrence & Compo 1997) was used to locate episodic oscillations, i.e. to show when energy is present at a certain frequency. Prior to the Wavelet analysis the data were filtered using a 3-hour Hanning-filter and then decimated at intervals of four hours. The series was zero-padded and analyzed using a Morlet base (Torrence & Compo 1997).

In addition to current meter records, CTD data from a number of years are used. Data from the Norwegian Antarctic Research Expeditions (NARE) are largely unpublished, and are from 1977, 1979, 1980, 1985, 1987, 1989, 1990, 1992, 1993 and 1995. The 1977 and 1979 data were presented in Foldvik et al. (1985*a,b*) and a few stations from 1990 were presented in Foldvik et al. (2004). CTD data from the Ronne Polynya Experiment (ROPEX) in 1998 (Nicholls et al. 2003), two AWI cruises in 1986/87 and 1995 (Wilfried & Oerter 1997, Miller & Oerter 1990), and data from WOCE (Orsi & Whitworth 2004) have been added to the analysis. More than 300 stations have been analyzed. The uncertainty in the data generally decreased for more recent cruises, but is assumed to be better than $\pm 0.006^\circ$C for temperature and ± 0.01 for salinity. Fig. 1 shows the CTD stations. All CTD data were collected during the Austral summer, since it is difficult to reach the area in wintertime due to harsh sea-ice conditions. The deepest measurement of the CTD is occasionally deeper than the echo-depth added manually to the data records, and this measurements has been used as the "true" bottom depth at these stations, whereas the echo-depth has been used at all other stations.

The thickness of the plume at each station was determined from the CTD temperature profiles. In the absence of the plume, the deeper part of the water column is occupied by WDW with a relatively constant temperature profile. The WDW temperature is close to 0.5°C at 1000 m depth and decreases linearly to 0°C at 2000 m depth. The thickness of the plume, when present, could be detected from the depth at which the temperature profile deviates from the WDW-profile, i.e. where the temperature decrease is larger than for the WDW. The criterion for detecting the cold bottom plume is $\frac{dT}{dz} > 5.0^\circ$C/1000 m (positive z upward). False detections of the plume thickness due to inversions in the temperature profile were removed manually.

Mean bottom temperature and plume thickness fields (Fig. 3) were found as follows. Only data between 30°W and 40°W and with depths between 800 and 3200 m were included. The CTD data were first divided into depth bins of 200 m (i.e. 800-1000, 1000-1200, ..., 3000-3200) and then into 0.25° bins zonally (i.e. 30-30.25, 30.25-30.50, ..., 39.75-40.00). The mean bottom temperature and plume thickness were calculated for each depth-longitude bin, and a corresponding color was applied to the map using the GEBCO bathymetry. When no stations were located in the bin, it was left white. The GEBCO depth and the depth recorded in the CTD data do not always agree, and the data may then be slightly displaced. The data from the Filchner Depression have not been divided into depth bins but have been projected onto 74°40'S.

3 Results

The CTD data from the Filchner Overflow area between 1977 and 1998 is first presented, providing a picture of the mean structure and properties of the plume. It will later be shown that the overflow is highly variable on relatively short temporal and spatial scales, and single CTD casts and sections must thus be thought of as "snap shots". The plume water can be distinguished from the ambient Weddell Deep Water based on temperature alone, and so only temperature data are presented.

3.1 Spatial structure

Before spilling over the sill, the ISW is found as a northward flowing subsurface layer in the Filchner Depression. Prior to 1989, observations showed a dense bottom layer of High Salinity Shelf Water (HSSW) underlying the ISW, but due to changing sea-ice conditions the supply of HSSW ceased and ISW now occupies the deepest portion of the trough (Nøst & Østerhus 1998). The ISW-interface tilts towards the west, and the upper limit is located at 500 m depth on the eastern side, and at 400 m depth on the western side (Foldvik et al. 2004). The ISW is stratified by salinity, which increases towards the bottom to a salinity between 34.6 and 34.7. A typical temperature profile from the Filchner Depression is presented in Fig. 2a (profile A, see Fig. 1 for locations), where the surface freezing point ($T_f \sim -1.9°C$) is marked. ISW, or water with temperatures lower than -1.9°C, is found below about 500 m depth. The minimum bottom temperature recorded in the Filchner Depression is -2.22°C.

When spilling over the sill, the ISW forms a dense plume that mixes with and entrains ambient WDW and the temperature profiles evolve accordingly. Fig. 2a shows three temperature profiles from the slope (profiles B-D: Fig. 1), that are characteristic of the area and show the "evolution" of the cold bottom plume layer. Profile C shows a thin, cold bottom layer, while profiles B and D show thicker layers with a higher minimum temperature. Most of the profiles from the area west of the ridge are similar to profile D, whereas those east of the ridge are often more similar to C.

The height at which the temperature profile deviates from the background WDW-profile is indicated in Fig. 2 by black diamonds. The plume thickness is defined as the distance between this transition point and the bottom, as illustrated by the vertical arrow in Fig. 2a for profile D (about 730 m). The maximum plume-thickness observed on the slope is 860 m. Stations that have a bottom temperature close to the freezing point generally have a plume thickness below 300 m, but mooring data occasionally show low temperatures at shallower depths (e.g. 433 mab at mooring F2). The bottom temperature of the thickest plume layers is usually in the range -1.0 to -0.5°C.

Among the years with available CTD-stations, 1985 has the best coverage and Fig. 2b shows a temperature section obtained this year. The section crosses the slope from 600 to 2000 m depth and runs parallel to the ridge along 36°W (see Fig. 1 for location). Only

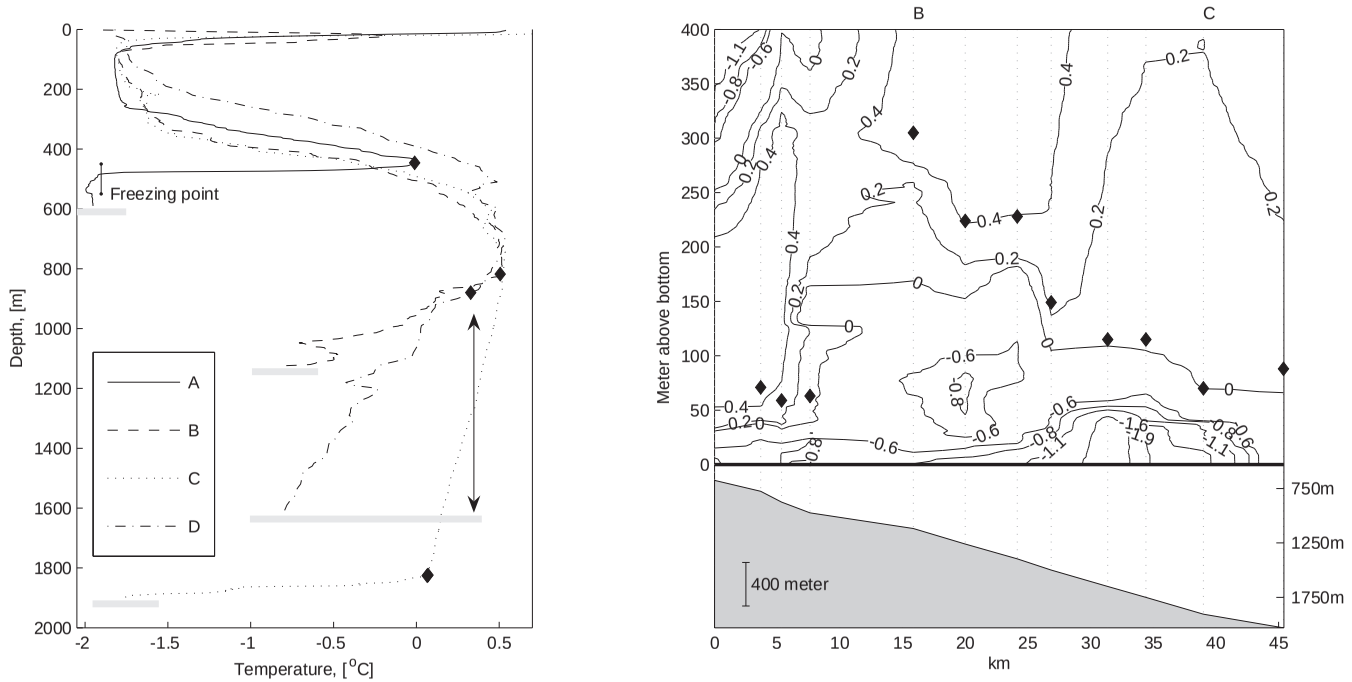

Figure 2: *a) Temperature profiles. The positions of the stations are marked in Fig. 1. Profiles A-C are from NARE 1985 (stations 13, 80, 86) and profile D is from Glacier 1978 (station 74). The black diamonds indicate the height of the plume and the arrow indicates the plume-thickness for profile D. The bottom is marked in gray. b) Temperature-section from NARE 1985. The position of the section is marked with a black line in Fig. 1. Only data from the 400 m closest to the bottom are shown. The dotted lines show the positions of the stations (stations shown in (a) are indicated with their respective letter). The lower panel shows the corresponding bottom topography.*

data from the bottom-most 400 m are included. A main cold core of the plume is visible around 1700 m depth (35 km) where the bottom temperature is -1.91°C. Profile C (40 km) has a plume thickness of about 120 m, and the transition towards the WDW is detected at 0.04°C. A second "core" is visible at 950 m depth (7 km) where the bottom temperature is -0.82°C and the plume about 60 m thick. Between the two "cores" the plume has a larger vertical extension (∼300 m), and a higher minimum temperature (profile B).

The "mean" bottom temperature and plume thickness are shown in Fig. 3 (See Section 2 for calculation details). As many of the stations do not capture the lower-most few meters, or tens of meters, we use 50 m as the lowest "plume thickness". Thickness values smaller (larger) than 50 (450) m are indicated as 50 (450) m, respectively. Stations where no plume was observed is marked with an asterisk. The background WDW temperature is 0°C at 2000 m depth, and -0.15°C at 3000 m depth.

A near-constant layer of ISW is seen in the Filchner Depression (west of 31°W along 74°40'S), where the bottom temperature is below -1.9°C and the layer thickness about 200 m. Stations on the slope with a cold bottom layer are usually found west of 33°30'W. The bottom temperature generally increases towards the north (deeper waters) and west (Fig. 3a), and the plume thickness increases (Fig. 3b). The core of the cold plume at ∼1000 m depth can be found around 34°W (Fig. 3a), but cold bottom temperatures are also found further west. The plume moves west while sinking down, and around 2000 m depth the plume is found west of 35°W. As the plume advances, it encounters the first ridge cross-cutting the slope, and Fig. 3a shows that low bottom temperatures and small layer thicknesses are found in the vicinity of this ridge at relatively large depths. Comparing temperatures from the same depth level east and west of the ridge, it is evident that it is warmer on the west side, where the temperatures are around -1°C at 1500 m depth and increase to -0.5°C at 2500 m and where the plume is 400 m thick or thicker. No thin cold stations, such as profile B in Fig. 2a, are found west of the ridges. The plume location cannot be easily defined in the west, where the dense water seems to occupy most of the slope between 800 and 2500 m depth. Fig. 3a show mean bottom temperatures from the moorings. The coldest moorings are F2 and F3 at 1200 and 1700 m depth close to 36°W (see Fig. 1 for location). They have mean temperatures around -1.6°C, which is close to the mean value from the CTD-stations.

The deepest patches of 'close to undiluted' ISW are found east of the ridge at 36°W at 2000 m depth. The absolute minimum at a station in this region is -1.64°C at 2175 m depth, while mooring D1 at 2100 m depth recorded a minimum temperature of -1.92°C and 8% of the data points from the lowest instrument are below -1.64°C.

The "mean" picture from the CTD data can be complemented with temperature and salinity records from the F1-F4 moorings, crosscutting the slope from 650 to 2000 m depth close to 36°W. The moorings have good temporal, but poor spatial resolution. Fig. 4 shows the (low-passed) Seabird MicroCAT temperature and salinity record in a Hovmöller

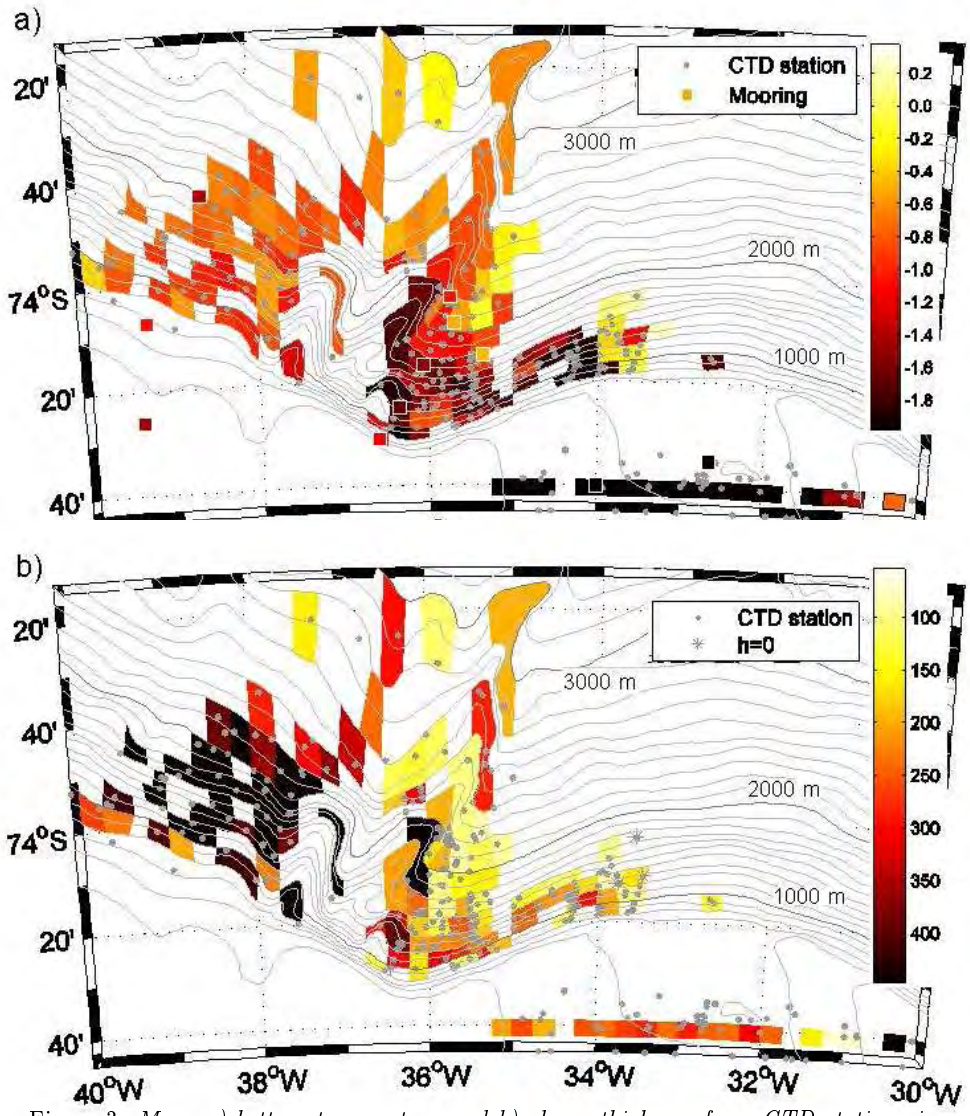

Figure 3: *Mean a) bottom temperature and b) plume thickness from CTD-stations in the Filchner Overflow area. The gray small dots indicate the positions of individual CTD-stations. The color shading represents calculated means over depth ranges of 200 m and in 0.25° longitude bins. More than 300 stations below 800 m depth are included. In (a) bottom moorings are shown as squares, with their color indicating the mean temperature over the length of the records. The plume thickness in (b) is found using the vertical temperature profiles as illustrated in Fig. 2. The asterisks in (b) indicate stations that have no cold bottom layer.*

diagram for February-March and June-July. The cold plume is generally present at the middle two moorings (F2 and F3; Fig. 1), which were located in the area with the lowest bottom temperature in Fig. 3a, and which recorded temperatures lower than -1.2°C most of the time . The plume is occasionally present at the lower and the upper mooring (F4 and F1; Fig. 1). The bottom temperatures were generally lower during the austral winter than during the summer, especially at the upper part of the slope, and the salinity was lower. The apparent variability will be the focus of the next section.

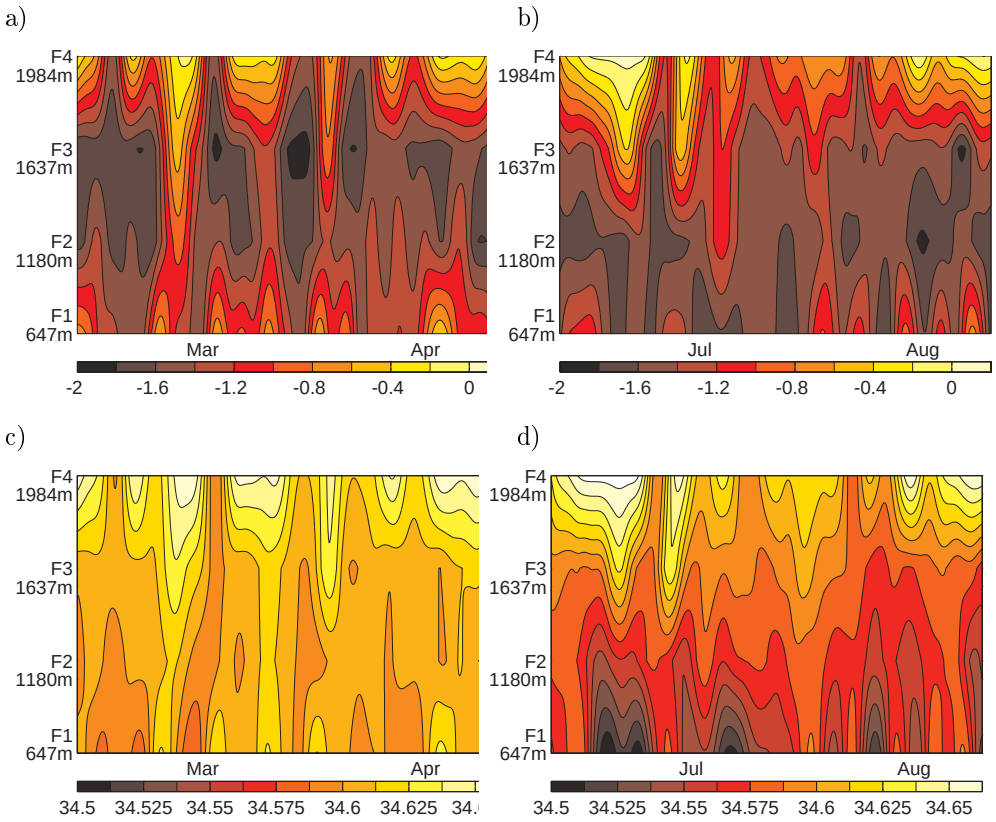

Figure 4: *Hovmöller diagram of bottom temperature in a) austral autumn and b) winter and bottom salinity in c) austral autumn and d) winter at mooring F1-4. Locations are shown in Fig. 1.*

3.2 Variability

A large part of the temporal plume variability is due to oscillations at more-or-less distinct frequencies. The tides, which are strong in the area, have been discussed elsewhere (Middleton et al. 1987, Foldvik et al. 1990), and the focus is here on the oscillations with periods of 35 hours, 3 days and 6 days that are repeatedly found in the mooring records. The oscillations will first be shown as they appear on individual moorings and then their geographical and temporal distributions will be presented. Individual moorings are generally referred to by their "names", as given in Fig. 1.

3.2.1 The 35-hour oscillation

Mooring F2 (Fig. 1) was placed in the center of the plume path at 1180 m depth in 1998 and recorded at 4 levels; 10, 56, 202, and 433 mab. The mean thickness of the plume in this area is 250-300 m (Fig. 3b, previous section). The lower current meter (10 mab) recorded a mean temperature of -1.63°C and is submerged in water with low temperatures most of the time (75% of the data points are below -1.5°C). Only occasionally does the temperature rise to 0°C. (3% of the data points are above -0.5°C). The middle instrument (56 mab) shows a similar temperature record, with temperatures being only slightly higher. The shallowest current meter (433 mab) is usually above the plume and within the WDW at 0.5°C (85% of the data points are above 0°C), but on a few occasions the temperature drops drastically (2% of the data points are below -1.5°C). The rise (drop) in temperature at the lower (upper) instruments often occurs during longer periods of temperature oscillations, such as the one depicted in Fig. 5a where the temperature at the lower instruments is seen to oscillate between a minimum of -2°C and a maximum of 0.5°C with a period of about 35 hours. The 35-hour oscillation is evident in the velocity data (Fig. 5b), where the oscillation in the along-slope component lags the across-slope component, giving a clockwise (CW) rotation. The amplitude of the oscillation is 10 cm/s, and the signal is seen, unattenuated, at all depths.

During this period, the same oscillation is observed at F1 (not shown), located further up the slope at 647 m depth. Here the temperature at all instrument depths (10, 100, 207 mab) oscillates between -1.8°C and 0.5°C. The amplitude of the velocity oscillation is smaller than at the deeper F2, but the signal is again almost vertically homogenous. Contrary to F2, the along-slope component leads, and the oscillation is counter-clockwise (CCW).

The 35-hour oscillation is present further down the slope, at F3 (1637 m, not shown). The oscillation here is mainly seen in the deeper (10 and 56 mab) temperature records and it is not recognizable (at least during this period) in the shallowest record, which is dominated by a slower oscillation (3 day). The bottom temperature and velocity records from the slope (F1-4) during the period are shown in Fig. 6.

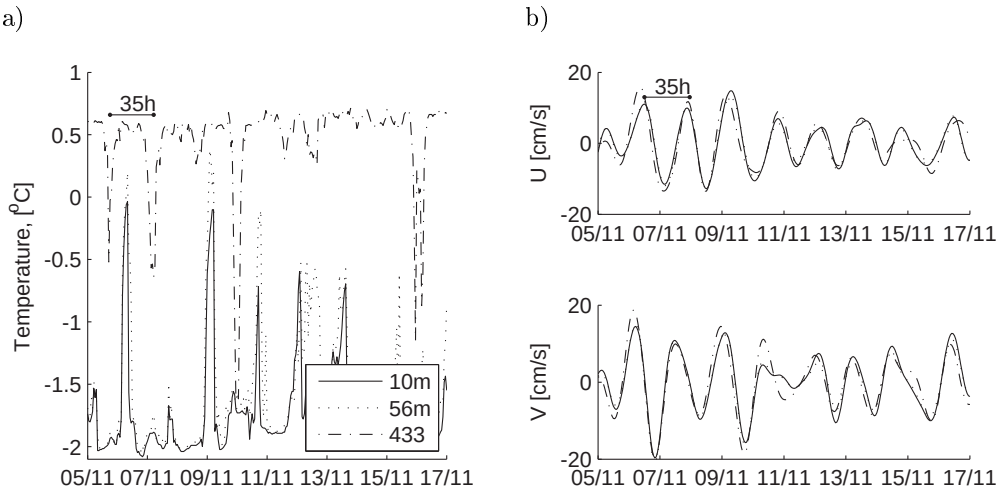

Figure 5: *a) Temperature and b) velocity from F2 (1180 m depth) in November 1998 showing a 35-hour oscillation. The records have been filtered (band passed 24-72h). The key in (b) applies to all graphs.*

3.2.2 The 3-day oscillation

The data records from mooring F3, located at 1637 m depth and probably on the lower side of the plume (see Fig. 1, 3, 4) show similar oscillations in temperature and velocity. The upper instrument (433 mab) has a mean temperature of 0.4°C and it is normally well above the plume since its temperature rarely drops below 0°C (0.5% of the data points). The bottom-most instrument (9 mab) recorded a mean temperature of -1.46°C with 80% of the data points being colder than -1°C.

Fig. 7 shows the temperature and velocity records from March 1998. The temperature at 433 mab is seen to oscillate between 0.3 and 0.4°C with a period of about 3 days. The same oscillation is present in the across-slope velocity record, where the amplitude is 20 cm/s. The data are unfiltered and contain a certain level of noise, but no clear vertical attenuation or phase shift is discernible. The oscillation is less clearly seen in the temperature records from the lower instruments, which are, during the end of the period shown, dominated by a faster 35-hour oscillation. The same is true for the along-slope velocity component (not shown) in which a 3-day oscillation can be distinguished initially and a 35-hour period towards the end of the period.

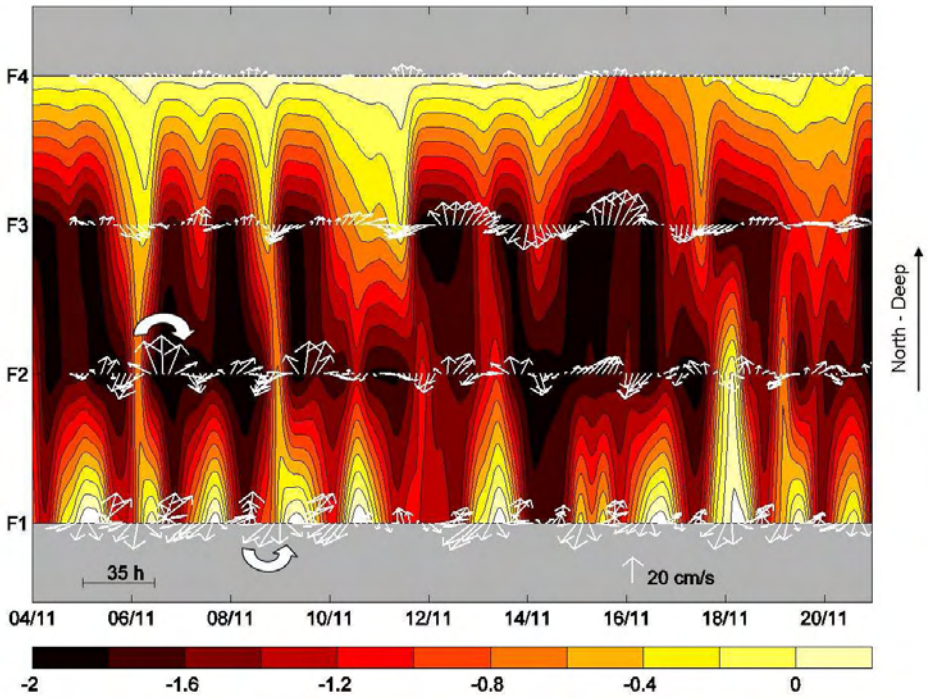

Figure 6: *Hovmöller diagram of bottom (9 mab) temperature from F1-4 during the episode with a 35-h oscillation shown in Fig. 5.*

3.2.3 The 6-day oscillation

Mooring F4 is situated at 1984 m depth and is generally below the main path of the plume (see Fig. 4). The mean temperature is -0.4°C and only 18% of the data points from 9 mab are below -1.0°C (5% are below -1.5°C). Fig. 8 shows velocity and temperature records from F4 during the winter months. A 6-day oscillation is seen at all depths, both in the temperature and velocity records, and its initiation is associated with a sudden drop in temperature at the bottom mooring. The temperature decreases from 0° C to close to -2° C (unfiltered data, not shown), indicating that the WDW, which is usually surrounding the mooring, is replaced by almost undiluted ISW. The temperature continues to oscillate with a period of approximately 6 days for about a month, but the amplitude decreases and the temperature at the bottom-most instrument stabilizes. The shallowest instrument (207 mab) is never submerged in cold plume water and so the plume is always thinner than 200 m, in agreement with the mean thickness from the CTD data in Fig. 3b. The oscillation at the upper instrument is out of phase with the deeper ones: low temperatures at the bottom are coupled to a slight increase (∼0.1°C) in temperature at 207 mab.

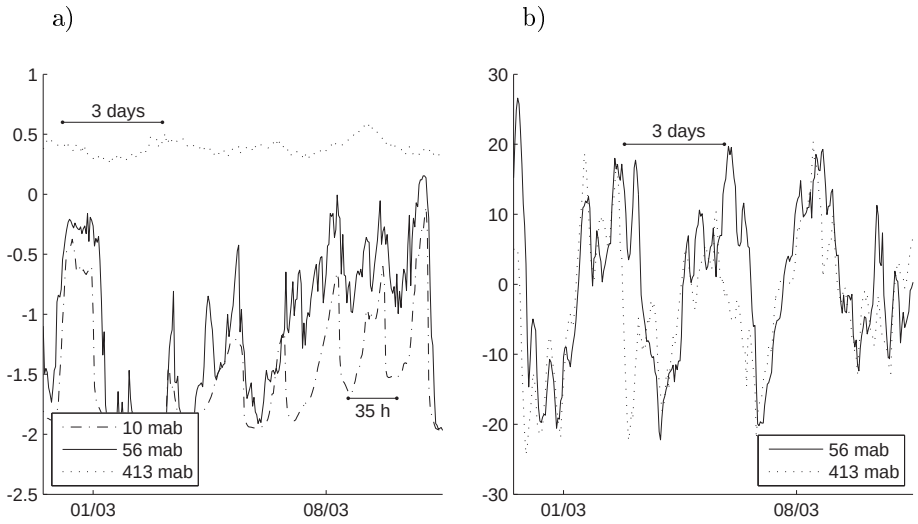

Figure 7: *a) Temperature and b) across-slope velocity (V) records from F3 (1637 m) in March 1998 showing a 3-day oscillation.*

There is a vertical shear in the mean current, with velocities increasing towards the bottom, but the oscillation in velocity is seemingly vertically homogenous with an amplitude of 5-10 cm/s. The velocity vectors trace out a clockwise ellipse in which the cold water is flowing with an eastward component, i.e. opposite to the mean flow.

Oscillations with the same 6-day period were recorded more than a decade earlier at mooring D1 (not shown), which was placed 100 m deeper than F4, 9 km to the north and in the vicinity of a steep rise running perpendicular to the slope. Here the oscillation is restricted to the along-ridge direction, rather than being "circular" as at F4. The amplitude was 35 cm/s and thus roughly equal to the mean speed (37 cm/s). The temperature record was oscillating in phase with the velocities, with low temperatures (∼-1.8° C) corresponding to high speeds (∼70 cm/s), and high temperatures (∼0° C) to slow (or no) currents (∼0 cm/s) (see Foldvik et al. (2004), Fig. 12d). The flow can be characterized as pulses of cold high-speed plume water and intermittent quiescent periods when the mooring is submerged in Weddell Deep Water. The oscillation is seen at both 25 and 100 mab.

3.2.4 Oscillations on the slope

Fourier analysis reveals that the three oscillations, henceforth referred to as O35, O3 and O6, are relatively energetic and reoccur over the slope. The periods are (within the accu-

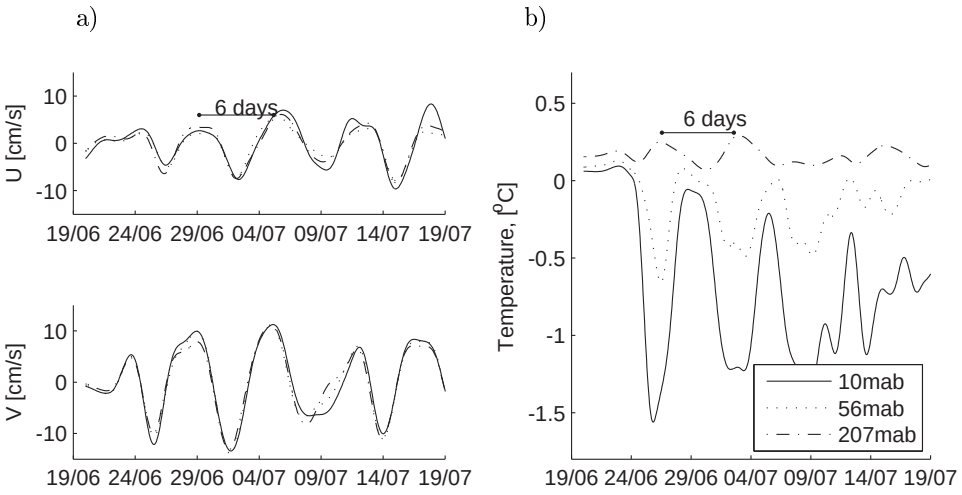

Figure 8: *a) Temperature and b) velocity at F4 (1984 m) in June 1998 showing a six-day oscillation. The records have been filtered (band passed, 3-15days). The key in (b) is valid for all graphs.*

racy of the methods used) multiples of each other: O6 = 2×O3 = 4×O35. Fig. 9 show the Fourier spectra for four instruments on the slope. Some moorings have pronounced peaks (i.e. energy) at all three frequencies (e.g. F3, Fig. 9d) while others have one (e.g. D1, Fig. 9a) or two (e.g. D2/F2, Fig. 9b/c) dominant peaks. At some moorings the peaks are seen in both velocity components (e.g. F2, Fig. 9b), while one component is totally dominant at others (e.g. u at D1, Fig. 9a). At D2, O35 is strongest in the along-shelf component and O3 in the across-shelf component. The shallow moorings west of the ridges have low energy levels and no prominent peaks, other than at tidal frequencies.

Fig. 10 gives an overview of the energy levels at the three frequencies (O35, O3, O6). Each mooring is represented with a pie-chart, whose area is proportional to the sum of the energy levels at the three frequencies and where the distribution of the energy amongst them is indicated by the size of the sector. The energy levels presented are the mean over an interval $f \pm \Delta f$ (shaded gray in Fig. 9) using velocity data from all instrument levels on the mooring. Energy levels are highest in the area west of the Filchner Depression, while lower levels are found in the depression and west of the two ridges. There is a tendency for the shortest period (O35) to be more pronounced at the upper part of the slope, while the longest (O6) is more energetic further down and the intermediate (O3) in the middle part of the slope. Mooring D2 is however an (energetic) exception. The moorings in the Filchner Depression have high energy levels at longer periods (10-15 days), but of the three frequencies discussed here only O6 is observed.

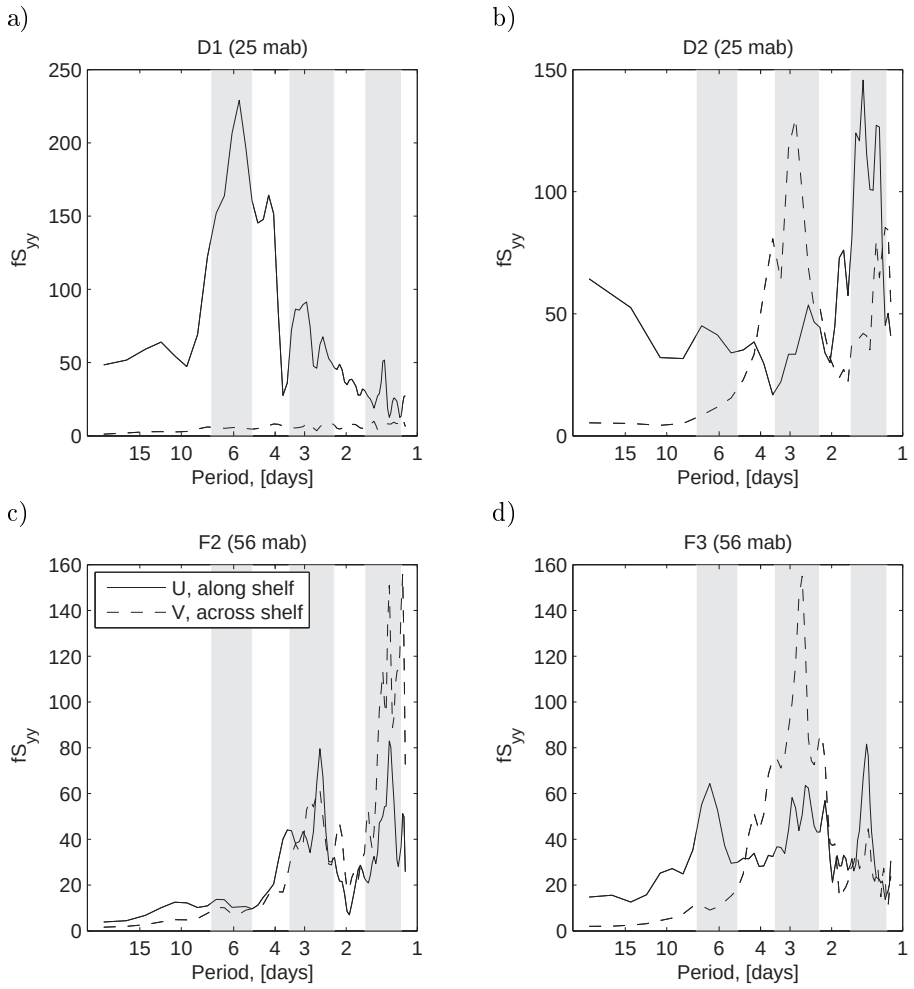

Figure 9: *Fourier spectra for mooring a) D1 (25 mab), b) D2 (25 mab), c) F2 (56 mab) and d) F3 (56mab) for the u (solid line) and v (dashed line) component. The shaded areas indicate the frequency intervals included in Fig. 10.*

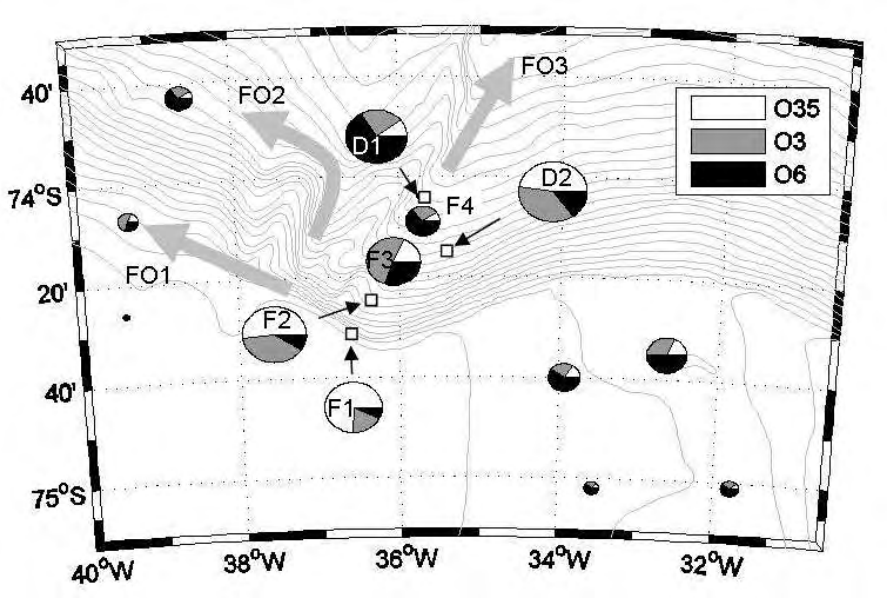

Figure 10: *Partition of energy for the three velocity oscillations discussed, i.e. with periods of 35 hours (O35), 3 days (O3) and 6 days (O6). Each mooring is represented by a pie-chart whose area is proportional to the total mean energy level of the three frequencies and where the distribution of the energy amongst them is indicated by the size of the sector. The energy level is calculated as the mean over an interval (shaded gray in Fig. 9) around the frequencies of interest. Velocity data from all instrument levels on the moorings have been included. The light gray arrows (FO1-3) are the pathways suggested by Foldvik et al (2004) and are discussed in section 4.1.*

The oscillations and the observations at the moorings are summarized in Table 1.

3.2.5 Temporal distribution

The episodic nature of the oscillations at some of the moorings, and their persistency at others, become apparent through wavelet analysis and is summarized in Table 1. Fig. 11 presents results from the wavelet analysis of records from moorings D1 and D2, placed 40 km apart at a depth of 1800 and 2100 m respectively (during 1985). The differences between the two moorings are striking. D1 shows a relatively persistent 6-day oscillation in the along-slope velocity (u, Fig. 11a), while D2 shows an intermittent 35-hour oscillation in the along-slope velocity (u) and temperature (T) and a more persistent tidal (diurnal) and 3-day oscillation in the across-slope velocity (v, Fig. 11b-d). The variations in temperature at D2 are associated with oscillations in u. During periods without the 35-hour oscillation

(in u) the mooring is surrounded by warm ($\sim$0°C) WDW, while the oscillation brings cold water ($T \sim -1.9$°C) to the mooring. The cold water is thus advected along the slope, and not across it. The correlation between u and T over the whole record is high (r = 0.85), with high (50-75 cm/s) westward velocities at low temperatures (see also Foldvik et al. (2004) Fig. 12, section 6.2)

The co-occurrence of low temperatures and oscillations is apparent at other moorings located at the lower (F4 - O6) and upper (F1 - O35) sides of the plume. It is notable that the strong, predominantly diurnal tidal signal (in both u and v) at F1 (close to the shelf break) is apparent in the velocity records but not in the temperature records, while O35 affects both velocity and temperature. The strong tidal signal at F1 is associated with continental shelf waves (Middleton et al. 1987). With a few exceptions, the oscillations are episodic (see Table 1).

3.2.6 Summary

The current meter records from the Filchner area show that oscillations with periods of 35 hours (O35), three days (O3) and 6 days (O6) are present, in addition to tidal motion. These periods are observed at several locations, and in records from different years (Table 1).

- Oscillations in velocity are accompanied by oscillations in temperature
- The oscillatory motion is neither attenuated nor strengthened with depth. This is also apparent when the shallowest instruments are above the dense bottom layer.
- Velocity amplitudes range from 5-10 cm/s to 35 cm/s.
- The (small) temperature oscillations recorded at instruments above the plume (surrounded by WDW) are often out of phase with the (larger) temperature oscillations at the lower instruments, i.e. the temperature increases at height when it decreases at depth.
- The oscillations are (with a few exceptions) episodic and on a number of moorings the oscillations are associated with the presence of cold plume water at the mooring.
- Both CW and CCW motions are observed, with CCW motion located higher up the slope
- The shortest period (O35) is apparently stronger on the upper part of the slope, while O6 is observed at the lower part and O3 in between, with some exceptions.
- Moorings in the Filchner Depression, on the continental shelf and west of the two ridges have relatively low energy levels and no distinct peaks at O35 and O3, while O6 is clearly discernible in the depression and at the deep western mooring.

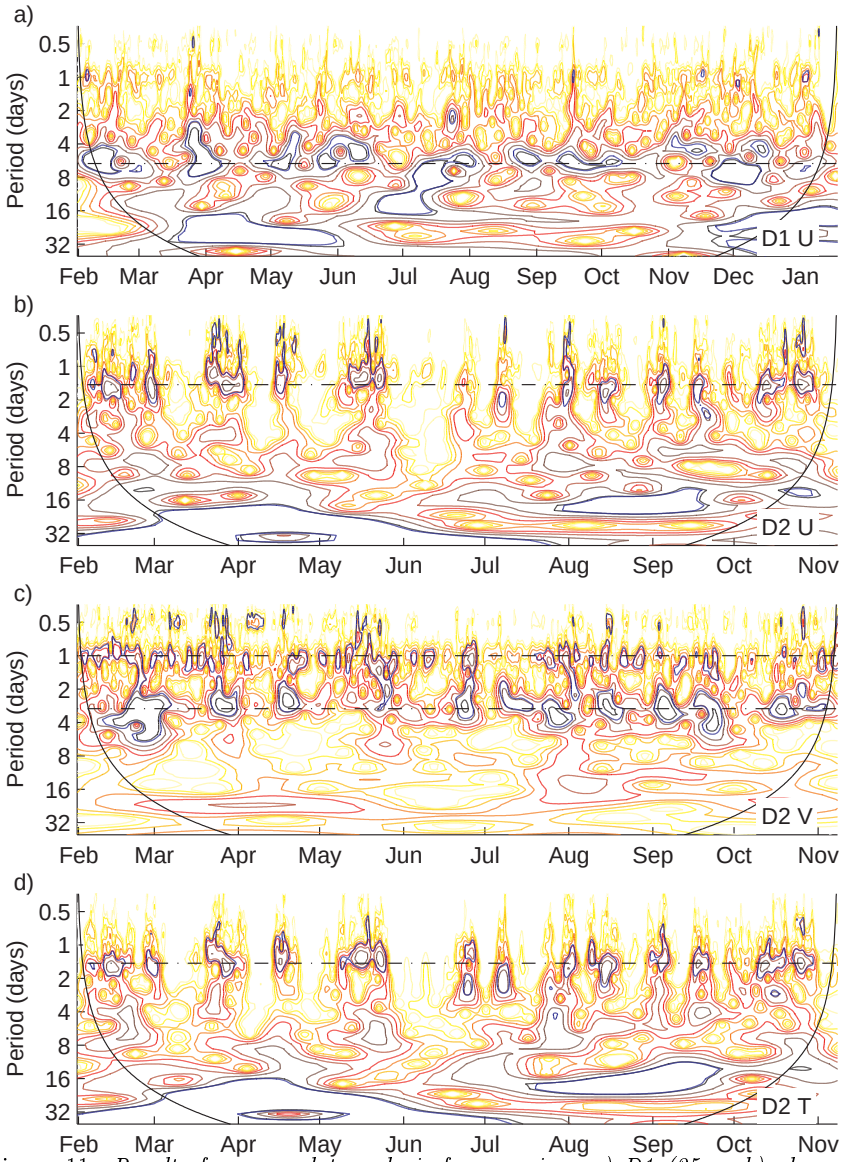

Figure 11: *Results from wavelet analysis for moorings a) D1 (25 mab) along-ridge velocity (u), b) D2 (25 mab) along-slope velocity (u), c) D2 (25 mab) across-slope velocity (v), and d) D2 (25 mab) temperature (T). Dark (brown) contours indicate high energy levels and light (yellow) low levels. The blue contours are 95% confidence levels. Black contours mark the "cone of influence", i.e. where end-effects are expected. Frequencies discussed in the text are marked with dashed lines.*

	Observed at	Depth	U	V	T	CCW/CW	Comments
O35	F1	647	x	x	x	CCW	Episodic, v. homogenous
	F2	1180	(x)	x	x	CW	Episodic, v. homogenous
	F3	1637	x	(x)	x	CW	Episodic, not v. homogenous
	D2	1800	x		x	-	Episodic
O3	F2	1180	x	x	(x)	CCW	Episodic, v. homogenous
	F3	1637	(x)	x	x	CW	Relatively persistent, v. homogenous
	D2	1800		x		-	Relatively persistent
	F4	1980	x	x	x	CW	Episodic
O6	F.D.	∼600	(x)	(x)		CCW	Energy also at lower frequencies
	F3	1637	x			-	Not v. homogenous
	W.R.	1939	(x)	(x)			
	F4	1980	x	x	x	CW	Episodic, v. homogenous
	D1	2100	x		x	-	Persistent

Table 1: *Summary of observations of oscillations (O35, O3, O6) at the moorings. F.D. = Filchner Depression, W.R. = West of Ridge, v. = vertical, and '(x)' means that the oscillation is observed, but that the energy level is relatively low.*

4 Discussion

4.1 Structure

The dense ISW in the Filchner Depression has the potential to sink to the bottom of the Weddell Sea. The initial density difference is not so large; its *in situ* density at sill level (600 m) is 1030.8 kg/m^3 compared with 1030.7 kg/m^3 for the WDW found here, but its low temperature makes it more compressible than the WDW. At 3000 m depth, the ISW would have an *in situ* density of 1041.9 kg/m^3, while the WDW has a density of 1041.7 kg/m^3. Thus thermobaricity, or the effect of temperature on the compressibility of sea water, makes it possible for ISW to penetrate to great depths (Killworth 1977).

The ∼25 years of CTD data presented in Section 3.1 confirm the presence of a cold bottom plume westward of 34°W and deeper than 800 m. Data from the shallower part of the slope have not been included in the analysis, since it is difficult to distinguish the plume from the surface layer of Winter Water (Mosby 1934) by means of temperature.

Bottom temperatures and plume thickness increase westward and there is a qualitative difference between CTD-profiles east and west of the ridges. West of the ridges the plume is thick (>450 m), and it has relatively high bottom temperatures and small vertical temperature gradients. CTD-casts from eastern locations often show low temperatures and thin plumes with large temperature gradients. Mixing and entrainment of ambient WDW is relatively low in the sill region, while it is more important between the eastern and western stations. No attempt has been made to quantify rates of mixing in the region. Cold and almost undiluted ISW is sometimes observed at great depth along the first of the two ridges, contrary to Wåhlin et al. (2007), who observed mixing to be enhanced by topography and topographic steering.

Based on mooring and CTD data, Foldvik et al. (2004) suggested that the ISW-plume follows three different pathways: one following the shelf break and the upper part (600-800 m) of the slope (FO1), one flowing at mid-depth (2500-3000 m) (FO2), and one being channeled downslope by a ridge located at ∼ 36°W (FO3). The partition of the plume is sketched in Fig. 10. Of the three suggested branches, only FO3, following the ridge downslope, can be seen in the mean temperature and thickness fields presented in Fig. 3. FO2 was detected as a cold, low salinity bottom layer around 39°W by Foster & Carmack (1976) in data from 1973 (not included in this study), but it is not apparent here. According to the data presented here, plume water occupies almost the entire slope west of the ridges, i.e. the area between FO1 and FO2. It should be noted that much (but not all) of the data from the area west of the ridges are from 1978. As discussed above, the analysis includes only data >800 m depth, and hence FO1 is too shallow to be detected.

Darelius & Wåhlin (2007) and Wåhlin (2002) showed that ridges and canyons crosscutting the slope can promote the downslope flow of dense water. They further introduced the

concept of transport capacity, i.e. that there is a maximum amount of dense water that a submarine ridge or canyon with given dimensions can steer downslope, and they suggested that a dense plume impinging on a ridge or a canyon would split if its transport capacity is exceeded. FO3 was shown by Darelius (2007) to be a result of topographic steering, and a CTD-section across the ridge shows a dense layer "leaning" on it (See Darelius (2007), Fig. 7). As mentioned above, our data do not support the idea of a clearly defined second path, FO2 at mid depth. If it nevertheless exists, it could be explained by topographic steering. About 20 km west of the first ridge there is a second ridge, extending down to about 2000 m depth (see Fig. 1). The two ridges create a canyon-like structure between them, in which dense plume water can be channeled downslope. At the end of the canyon, at about 2000 m depth, the plume water would again flow on the open slope, following the isobaths geostrophically (FO2). The transport capacity of the first ridge was estimated to be 0.3 Sv ISW by Darelius & Wåhlin (2007) and that of the canyon would be 0.6 Sv, using a ridge width, $W = 7$ km, an Ekman layer thickness, $\delta = 35$ m, a bottom slope, $s = 0.03$, a ridge height, $H = 500$ m, and an idealized cosine shaped canyon. A density difference of $\Delta\rho = 0.1$ kg/m^3 was used in the calculations ($\Delta\rho = 0.05$ kg/m^3 gives 0.15 (0.3) Sv for the first (second) ridge). The total outflow is estimated to be 1.6 Sv (Foldvik et al. 2004) and the two ridges could thus together channel a substantial part of the outflow downslope, and tentatively explain the suggested pathways. The upper pathway (FO1) would be followed by water that initially flows sufficiently high up on the slope to escape the ridges (which emerge a few hundred meters below the shelf break) and by water that flows over the ridges/canyon as their transport capacity is exceeded. Dense water steered by the first ridge follows FO3 and by the second ridge FO2. But again, the observation of a thick layer of plume water west of the ridges does not match this explanation. This water is likely to have passed over the second ridge. It seems strange, that the second ridge would not steer dense water downslope, when the first ridge seems to be so effective in doing so. Unfortunately, there are neither CTD nor mooring data available in the vicinity of the second ridge, so its role remains an open question.

4.2 Variability

Fourier analysis reveals high energy levels for motion with periods of roughly 35 hours (O35), 3 days (O3) and 6 days (O6). Curiously, the periods seems to be (within the accuracy of the methods used) multiplies of each other: O6 = 2×O3 = 4×O35. O35 is most pronounced at the upper part of the slope, with mooring D2 at 1775 m being an energetic exception. O3 is mainly observed in the across-slope direction (v) further down on the slope, while O6 is most pronounced in the vicinity of the ridge and at the deepest moorings. Moorings situated in the Filchner Depression and west of the ridges show low energy levels and no prominent peaks at 035 and O3, while O6 can be identified in the Filchner Depression and at the deep mooring west of the ridges. The current measurements suggest that the oscillations are barotropic or close to barotropic. Although the data records do not extend all the way to the surface, they do in many cases extend well above the dense bottom layer, and the oscillations are generally present, unattenuated, at all instrument levels. The

temperature records from levels above the plume often show a small amplitude oscillation ($\sim 0.1°$C) that is out of phase with that from instruments at lower levels. The observation agrees with general theories on wave-kinematics, where convergence and upward motion in the lower layer is accompanied by divergence and downward motion in the upper layer (and vice versa). The temperature gradient in the overlying WDW is about 0.5°C / 1000 m, and a temperature difference of 0.1°C corresponds to a vertical excursion of about 200 m.

The energetic oscillations found in the overflow area could either be caused by external disturbances or waves traveling into the area, or they could be generated locally and directly related to the overflow. Inertial oscillations in the region would be faster, with a period of 12.4 h. Observations from other overflows (Geyer et al. 2006, Girton & Sanford 2003, Bruce 1995), laboratory experiments (Cenedese et al. 2004, Etling et al. 2000, Lane-Serff & Baines 1998, Smith 1977) and numerical models (Ezer 2006, Tanaka & Akitomo 2001) show that eddies may form within dense overflows and plumes. One external candidate is continental shelf waves (CSW), which would travel westward along the shelf. Such waves were suggested by Foldvik et al. (2004), without further discussion, as an explanation for the 3-6 day oscillations. Shelf waves cause the enhanced diurnal tides observed at the shelf break (Middleton et al. 1987). The observations are compared with existing theories on such eddies and waves below.

Eddies Eddies are generally thought to form in dense overflows and plumes either through vortex stretching (Lane-Serff & Baines 1998, Spall & Price 1998) or baroclinic instability (Swaters 1991). Vortex stretching tends to form strong eddies close to the source, while baroclinic instabilities form as an along-slope flow is established (Lane-Serff 2001). The baroclinic eddies are often accompanied by sub-plumes, such as in laboratory experiments by Etling et al. (2000). Both generation mechanisms will be considered here.

In short, eddies are generated through vortex stretching when the fluid above the dense layer is captured and stretched as the dense fluid descends the slope. To maintain its potential vorticity, a vortical circulation is generated that is transmitted to the lower layer barotropically. The generation mechanisms are described in more detail by Lane-Serff & Baines (1998) and Cenedese et al. (2004), and will not be further commented on here. The eddies so formed are baroclinic, with a strong barotropic component (Lane-Serff & Baines 1998) and the motion is cyclonic and strongest in the upper layer. In contrast, the oscillations found here are all barotropic or close to barotropic, i.e constant with depth. Lane-Serff & Baines (2000) estimated that vortex stretching would cause eddy generation with a period of three days within the Filchner Overflow.

Etling et al. (2000) suggested that eddies were formed through vortex stretching in laboratory experiments when the induced coastal current passed over a plume and was compressed vertically. These eddies propagated seemingly independent of the plume itself, although sometimes trapping dense fluid beneath them. The Antarctic Coastal Current

splits in two just east of the Filchner Depression (at 27°W) with one branch continuing along the slope and one as a coastal current (Gill 1973). The slope current must pass over the plume, possibly generating eddies. These eddies, if trapping dense fluid beneath them, would have a baroclinic component similar to those described above.

The PV-hypothesis was proposed by Spall & Price (1998) to explain the generation of eddies in the Denmark Strait overflow. It is based on vortex stretching, but it is not appropriate for the Filchner Overflow since it requires a three-layer outflow.

Eddies may form from baroclinic instabilities (Tanaka & Akitomo 2001, Jiang & Garwood 1996, Swaters 1991, Smith 1976). Spall & Price (1998) discussed baroclinic instabilities in relation to the Denmark Strait overflow, and concluded that the observed eddies probably were not generated by such instabilities. Many of their arguments can be applied to the Filchner Overflow. The oscillations observed in the Filchner Overflow show little or no vertical phaseshift (Fig. 5, 7, 8), while growing baroclinic waves require a substantial shift. Contrary to the observed barotropic (or close to barotropic) oscillations, eddies formed from baroclinic instabilities are stronger within the dense bottom layer than in the fluid above. The baroclinic eddies are concentrated, or at least much stronger, on the downslope side of the flow and cannot explain the energetic oscillations recorded at the upper part of the slope (Fig. 10). In addition, the development of eddies from baroclinic eddies are relatively slow. Plume water spilling over the sill and advancing with 20 cm/s can be expected to reach the mooring array F1-F4 within 2-3 days, while baroclinic eddies formed in Tanaka's (2006) simulations reached a mature stage only after 17 days in their "Steep slope-High latitude" (SH) scenario, which has a slope, Coriolis parameter, flux and density difference appropriate for the Filchner Overflow, albeit a different outflow geometry. Baroclinic instabilities are initialized on an initially steady current, and there are no observations or indications of such a flow downstream of the Filchner sill. In summary, the observations cannot be explained by baroclinic instabilities.

Continental Shelf Waves Another possible explanation for the observed oscillations is coastally trapped waves or so-called continental shelf waves (CSW). These waves, as their name implies, are trapped along the shelf and propagate (in the southern hemisphere) with the coast to the left (i.e. westward around Antarctica) as a sequence of horizontal eddies with alternating sign (LeBlond & Mysak 1978). Much like topographic Rossby waves, they owe their existence to the combined effect of rotation and variable water depth and they typically have amplitudes of a few centimeters, periods of several days and wavelengths much longer than the Rossby radius (Mysak 1980). CSW can be both barotropic and baroclinic and their amplitude decreases exponentially away from the shelf break. The waves are usually generated by atmospheric forcing or wind (Mysak 1980), but other generation mechanisms are possible, such as interactions between currents and topography and variable discharge from the coast. The observed intensification of the diurnal tidal currents near the

shelf-break in the Weddell Sea is thought to be due to the excitation of shelf waves with tidal frequencies (Robertson 2005, Middleton et al. 1987). In a laboratory setting, Whitehead & Chapman (1986) observed shelf waves to be generated by a low density surface current over a sloping bottom when the speed of the current was smaller than the phase speed of a first mode barotropic shelf wave. Shelf waves could thus propagate into the area, or be generated locally, possibly by mechanisms related to the outflow itself.

Middleton et al. (1982) adapted a barotropic shelf wave model (Saint-Guily 1976) for the southern hemisphere and the continental slope in the Filchner area. Based on data from the older moorings west of the ridges, they provided evidence for the existence of shelf waves with frequencies of 3-60 days in the area. The energy levels at those locations are much lower than those reported for further east, and there are no prominent peaks in the energy spectra. The authors suggest atmospheric forcing as a likely generation mechanism. Looking closer at O35 in respect to shelf waves and the Saint-Guily model, it's seen that the frequency would correspond to a wavelength of about 200 km and that the first mode is the only possible mode (Middleton et al. (1982), Fig. 10a). The first mode corresponds to CCW motion on the upper slope and a CW motion lower down with the transition occurring at roughly 1000 m depth. Mooring F1, located at 687 m depth, shows a strong CCW signal at O35, while F2, at 1180 m depth, shows a strong CW signal (weak CW signal at F3 and F4) - as predicted by the shelf wave model. (This pattern is not, as it will be discussed later, unique for shelf waves.) The oscillations occur episodically and normally lasts a couple of periods. The motions are barotropic or close to barotropic, and strongest at the shallowest part of the slope. When concentrating on the F-moorings it seems plausible that O35 may be related to propagating shelf waves, but D2 (1775 m) shows a relatively strong along-shelf oscillation at O35 (discussed in Foldvik et al. (2003)) and the older moorings, located west of the ridges and close to the shelf break, show no O35 at all. The latter point could possibly be explained by interannual variability, i.e. that the waves were not generated when the moorings west of the ridge were operating, or by the presence of the two ridges between the observation points, as relatively small topographic irregularities have been shown to scatter, reflect or degenerate barotropic shelf waves (Mysak 1980). Shelf waves are strongest at the shelf break and could not satisfactorily explain the oscillations that are observed to be most energetic lower down on the slope, i.e. O3 and O6. Shelf waves can travel far. The frequency (O35) is not mentioned by Fahrbach et al. (1992), who reports on variability from current meter moorings placed on the continental slope further east on Kapp Norvegia (17°W) and it is not seen in data from current meter moorings on the continental slope on the eastern tip (45-55°E, 64°S) of the Antarctic Peninsula (von Gyldenfeldt et al. 2002). (O3 and O6 are not reported on Kapp Norvegia / the Antarctic Peninsula either.) If the oscillations are due to shelf waves, the generation mechanism, and the preference for the observed period(s), remains to be explained.

The rotation at the moorings for O35 (CCW at the top of the slope and CW further down), was shown to agree with the shelf wave model of Middleton et al. (1982). The

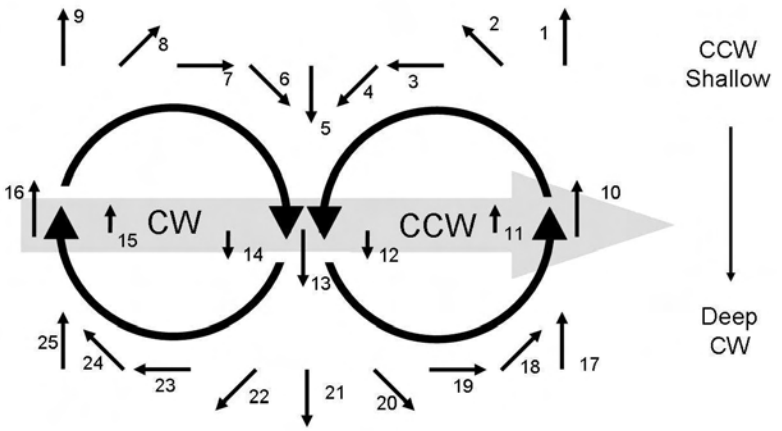

Figure 12: *Sketch of a CW and a CCW eddy passing westward on a continental slope. The gray arrow indicates the direction of eddy-motion and the small, numerated black arrows indicate currents registered at moorings located on the shallow side (1-9), in the center (10-16), and on the deep side (17-25) of the eddies. The mooring at the shallow (deep) side register CCW (CW) motion, while the mooring in the center register an across-slope oscillation.*

observed pattern could, however, be given by any eddy-train, cyclonic, anticyclonic or alternating, traveling westward along the slope and passing the mooring array with the eddy center between F1 and F2. A mooring located on the shallower side of an eddy traveling westward will register a CCW motion, and a mooring located on the deeper side will register a CW motion, regardless of whether the eddy itself is rotating counter-clockwise or clockwise (Fig. 12). A mooring located near the center of the eddy will register an oscillation in the across slope component only. The pattern is readily recognized in Table 1, at least for O35 and O3, where CCW motion is found on the shallower moorings and CW motion on the deeper. The oscillations on D1 are strongly steered by the ridge.

Bearing in mind the low energy levels downstream of the two submarine ridges cross-cutting the shelf, it is interesting to note the laboratory observations made by Wåhlin et al. (2007) regarding eddies intersecting submarine ridges and canyons. They found that the ridge effectively blocked the eddies; the rotary motion in the upper layer ceased and the surface water was partly deflected upslope. Meanwhile, the dense bottom layer "escaped" and flowed downslope along the ridge. In these experiments the ridge was relatively high compared with the water depth. In another set of experiments, eddies were found to pass over topography that was half the height of the water depth (Adduce & Cenedese 2004). The height of the ridges are about 300 and 600 m respectively, and it is possible that they, or at least the second, highest ridge, could be involved in blocking eddies moving westward.

The strong oscillations observed at D1, in the vicinity of the ridge, could, somewhat speculatively, be connected to laboratory observations made by Darelius & Wåhlin (2007) and Wåhlin et al. (2007). They describe wavelike features appearing as dense fluid is steered downslope by the ridge. Potentially, the acceleration of the topographically steered fluid could cause the flow to become supercritical, making it possible for roll waves to develop (Cenedese et al. 2004, Swaters 2003, Fer et al. 2002). Roll-waves can develop in dense gravity plumes if the Froude number is larger than two (Fer et al. 2002), but these instabilities would be super-inertial, i.e. have a frequency larger than the Coriolis parameter f (Swaters 2003). The observed oscillations are, however, sub-inertial. The O6 period is observed in the Filchner Depression, suggesting that the oscillations are generated further upstream.

5 Conclusion

The overflow of cold Ice Shelf Water from the Filchner Depression in the Weddell Sea has been described, based on CTD and current meter data. The plume appears as a 100-300 m thick bottom layer with minimum temperatures close to the surface freezing point at depths >1700 m on the eastern side of two ridges crosscutting the slope close to 36° W. Plume water is effectively guided by the topography, flowing downslope along the first of the ridges. West of the ridges, the temperature of the cold bottom layer is higher, and the plume thickness has increased up to a maximum of over 800 m. Diluted plume water occupies the slope between 800 - 2500 m depth.

Three dominating oscillations, with periods of 35 hours, 3 and 6 days are documented, in addition to tidal oscillations. The three oscillations explain a large part of the variability on the slope. The 35-hour oscillation is strongest at the top of the slope, while the 3-day and 6-day oscillation are most energetic at greater depths. Energy levels are lower west of the two ridges and in the Filchner Depression. The oscillations are seen in both velocity and temperature records, and the motion is seemingly barotropic. Three mechanisms concerning overflow plumes and variability on continental slopes were considered: eddies generated by vortex stretching, eddies generated by baroclinic instabilities and continental shelf waves, but none of them seems to satisfactorily explain the observations.

Acknowledgements We thank all scientists and crew members who have been involved in the collection and preparation of the data.

References

Adduce, C. & Cenedese, C. (2004), 'An experimental study of a mesoscale vortex colliding with topography of varying geometry in a rotating fluid', *Journal of Marine Research* **62**(5), 611–638.

Adduce, C. & Cendese, C. (2007), 'Mixing in a density driven current down a slope in a rotating fluid', *Journal of Fluid Mechanics* (submitted).

Broecker, W. S., Peacock, S. L., Walker, S., Weiss, R., Fahrbach, E., Schroeder, M., Mikolajewicz, U., Heinze, C., Key, R., Peng, T. H. & Rubin, S. (1998), 'How much deep water is formed in the Southern Ocean?', *Journal of Geophysical Research-Oceans* **103**(C8), 15833–15843.

Bruce, J. G. (1995), 'Eddies southwest of the Denmark Strait', *Deep-Sea Research Part I-Oceanographic Research Papers* **42**(1), 13–29.

Cenedese, C., Whitehead, J. A., Ascarelli, T. A. & Ohiwa, M. (2004), 'A dense current flowing down a sloping bottom in a rotating fluid', *Journal of Physical Oceanography* **34**(1), 188–203.

Darelius, E. (2007), 'Topographic steering of dense overflow plumes: laboratory experiments with V-shaped canyons and ridges', *Manuscript*.

Darelius, E. & Wåhlin, A. (2007), 'Downward flow of dense water leaning on a submarine ridge', *Deep Sea Research* **56**(7), 1173–1188.

Deacon, G. (1937), 'The hydrology of the Southern Ocean', *Discovery Report* **15**, 1–24.

Dieckmann, G., Rohardt, G., Hellmer, H. & Kipfstuhl, J. (1986), 'The occurrence of ice platelets at 250 m depth near the Filchner Ice Shelf and its significance for sea ice biology', *Deep-Sea Research* **33**(2), 141–148.

Etling, D., Gelhardt, F., Schrader, U., Brennecke, F., Kuhn, G., d'Hieres, G. C. & Didelle, H. (2000), 'Experiments with density currents on a sloping bottom in a rotating fluid', *Dynamics of Atmospheres and Oceans* **31**(1-4), 139–164. Sp. Iss. SI.

Ezer, T. (2006), 'Topographic influence on overflow dynamics: Idealized numerical simulations and the Faroe Bank Channel overflow', *Journal of Geophysical Research* **111**(C02002).

Fahrbach, E., Rohardt, G. & Krause, G. (1992), 'The Antarctic coastal current in the Southeastern Weddell Sea', *Polar Biology* **12**(2), 171–182.

Fahrbach, E., Harms, S., Rohardt, G., Schroder, M. & Woodgate, R. A. (2001), 'Flow of bottom water in the northwestern Weddell Sea', *Journal of Geophysical Research-Oceans* **106**(C2), 2761–2778.

Fer, I., Lemmin, U. & Thorpe, S. A. (2002), 'Winter cascading of cold water in Lake Geneva', *Journal of Geophysical Research-Oceans* **107**(C6).

Foldvik, A. & Kvinge, T. (1974), 'Conditional instability of sea-water at freezing-point', *Deep-Sea Research* **21**(3), 169–174.

Foldvik, A. & Gammelsrød, T. (1988), 'Notes on Southern-Ocean Hydrography, Sea-Ice and Bottom Water Formation', *Palaeogeography Palaeoclimatology Palaeo-ecology* **67**(1-2), 3–17.

Foldvik, A., Gammelsrød, T. & Tørresen, T. (1985*a*), 'Hydrographic Observations from the Weddell Sea during the Norwegian antarctic Research Expedition 1976/1977', *Polar Research* **3**, 177–193.

Foldvik, A., Gammelsrød, T. & Tørresen, T. (1985*b*), 'Physical oceanography studies in the Weddell Sea during the Norwegian antarctic Research Expedition 1978/79', *Polar Research* **3**, 195–207.

Foldvik, A., Middleton, J. H. & Foster, T. D. (1990), 'The tides of the southern Weddell Sea', *Deep-Sea Research Part A-Oceanographic Research Papers* **37**(8), 1345–1362.

Foldvik, A., Gammelsrød, T., Restad, T. & Østerhus, S. (2003), 'On the structure and variability of the Filchner Overflow plume', *FRISP Report* **14**.

Foldvik, A., Gammelsrød, T., Østerhus, S., Fahrbach, E., Rohardt, G., Schrøder, M., Nicholls, K. W., Padman, L. & Woodgate, R. A. (2004), 'Ice shelf water overflow and bottom water formation in the southern Weddell Sea', *Journal of Geophysical Research-Oceans* **109**(C2).

Foster, T. D. & Carmack, E. C. (1976), 'Frontal zone mixing and Antarctic Bottom Water formation in the Southern Weddell Sea', *Deep-Sea Research* **23**(4), 301–317.

Geyer, F., Østerhus, S., Hansen, B. & Quadfasel, D. (2006), 'Observations of highly regular oscillations in the overflow plume downstream of the Faroe Bank Channel', *Journal of Geophysical Research* **111**(C12020).

Gill, A. (1973), 'Circulation and bottom water production in the Weddell Sea', *Deep Sea Research* **20**, 111–140.

Girton, J. B. & Sanford, T. B. (2003), 'Descent and modification of the overflow plume in the Denmark Strait', *Journal of Physical Oceanography* **33**(7), 1351–1364.

Gordon, A., Zambianchi, E., Orsi, A., Visbeck, M., Giulivi, C., Whitworth, T. & Spezie, G. (2004), 'Energetic plumes over the western Ross Sea continental slope', *Geophysical Research Letters* **31**(21).

Høyer, J. L. & Quadfasel, D. (2001), 'Detection of deep overflows with satellite altimetry', *Geophysical Research Letters* **28**(8), 1611–1614.

Jiang, L. & Garwood, R. W. (1996), 'Three-dimensional simulations of overflows on continental slopes', *Journal of Physical Oceanography* **26**(7), 1214–1233.

Jungclaus, J. H., Hauser, J. & Käse, R. H. (2001), 'Cyclogenesis in the Denmark Strait overflow plume', *Journal of Physical Oceanography* **31**(11), 3214–3229.

Killworth, P. (1977), 'Mixing on the Weddell Sea continental slope', *Deep-Sea Research* **24**, 427–448.

Killworth, P. (2001), 'O the rate of descent of overflows', *Journal of Geophysical Research-Oceans* **106**(C10), 22267–22275.

Käse, R. H., Girton, J. B. & Sanford, T. B. (2003), 'Structure and variability of the Denmark Strait Overflow: Model and observations', *Journal of Geophysical Research-Oceans* **108**(C6).

Lane-Serff, G. (2001), Overflows and cascades, *in* J. Steele, S. Thorpe & K. Turekian, eds, 'Encyclopedia of Ocean Sciences', Elsevier, Amsterdam.

Lane-Serff, G. F. & Baines, P. G. (1998), 'Eddy formation by dense flows on slopes in a rotating fluid', *Journal of Fluid Mechanics* **363**, 229–252.

Lane-Serff, G. F. & Baines, P. G. (2000), 'Eddy formation by overflows in stratified water', *Journal of Physical Oceanography* **30**(2), 327–337.

LeBlond, P. & Mysak, L. (1978), *Waves in the Ocean*, Vol. 20 of *Elsevier oceanography series*, Elsevier Scientific Publishing Company, Amsterdam.

Middleton, J. H., Foster, T. D. & Foldvik, A. (1982), 'Low-frequency currents and continental-shelf waves in the southern Weddell Sea', *Journal of Physical Oceanography* **12**(7), 618–634.

Middleton, J. H., Foster, T. D. & Foldvik, A. (1987), 'Diurnal shelf waves in the southern Weddell Sea', *Journal of Physical Oceanography* **17**(6), 784–791.

Miller, H. & Oerter, H. (1990), Die Expedition ANTARKTIS-V mit FS Polarster 1986/87, Bericht von den Fahrtabschnitten ANT-V/4-5, Reports on Polar Research, Technical Report 57, Alfred Wegener Institute for Polar and Marine Research, Bremerhaven.

Mosby, H. (1934), The waters of the Atlantic Antarctic Ocean, *in* 'Scientific Results of the Norwegian Antarctic Expeditions 1927-1928 et SQQ', Vol. 1, Det Norske Videnskaps-Akademi i Oslo, pp. 1–131.

Mysak, L. (1980), 'Recent advances in shelf wave dynamics', *Reviews of Geophysics and Space Physics* **18**, 211–241.

Nicholls, K. W., Østerhus, S., Makinson, K. & Johnson, M. R. (2001), 'Oceanographic conditions south of Berkner Island, beneath Filchner-Ronne Ice Shelf, antarctica', *Journal of Geophysical Research-Oceans* **106**(C6), 11481–11492.

Nicholls, K. W., Padman, L., Schröder, M., Woodgate, R., Jenkins, A. & Østerhus, S. (2003), 'Watermass modification over the continental shelf north of Ronne Ice Shelf, antarctica', *Journal of Geopysical Research* **108**(C8).

Nøst, O. A. & Foldvik, A. (1994), 'a model of ice-shelf ocean interaction with application to the Filcher-Ronne and Ross Ice Shelves', *Journal of Geophysical Research-Oceans* **99**(C7), 14243–14254.

Nøst, A. & Østerhus, S. (1998), Impact of grounded icebergs on the hydrographic conditions near the Filchner Ice Shelf, *in* S. S. Jacobs & R. F. Weiss, eds, 'Ocean, Ice, and Atmosphere - Interaction at the Antarctic Continental Margin', Vol. 75, AGU, Washington D.C.

Orsi, A. H., Johnson, G. C. & Bullister, J. L. (1999), 'Circulation, mixing, and production of antarctic Bottom Water', *Progress in Oceanography* **43**(1), 55–109.

Orsi, A. & Whitworth, I. (2004), *Hydrographic atlas of the World Ocean Circulation Experiment (WOCE). Volume 1: Southern Ocean*, International WOCE Project Office, Southampthon (http://woceatlas.tamu.edu/).

Robertson, R. (2005), 'Baroclinic and barotropic tides in the Weddell Sea', *Antarctic Science* **17**(3), 461–474.

Saint-Guily, B. (1976), 'Sur la propagation des ondes de seconde classe le long d'un talus continentla', *C.R. Acad. Sci. Paris* **B282**, 141–144.

Saunders, P. (2001), The dense northern overflows, *in* G. Siedler, J. Church & J. Gould, eds, 'Ocean Circulation and Climate', Vol. 77 of *International Geophysics Series*, Academic Press, pp. 401–418.

Schlitzer, R. (2007), 'Assimilation of radiocarbon and chlorofluorocarbon data to constrain deep and bottom water transports in the world ocean', *Journal of Physical Oceanography* **37**(2), 259–276.

Smedsrud, L. H. & Jenkins, A. (2004), 'Frazil ice formation in an ice shelf water plume', *Journal of Geophysical Research-Oceans* **109**(C3).

Smith, P. C. (1976), 'Baroclinic instability in Denmark Strait Overflow', *Journal of Physical Oceanography* **6**(3), 355.

Smith, P. C. (1977), 'Experiments with viscous source flows in rotating systems', *Dynamics of Atmospheres and Oceans* **1**(3), 241–272.

Spall, M. A. & Price, J. F. (1998), 'Mesoscale variability in Denmark Strait: The PV outflow hypothesis', *Journal of Physical Oceanography* **28**(8), 1598–1623.

Swaters, G. E. (1991), 'O the baroclinic instability of cold-core coupled density fronts on a sloping continental-shelf', *Journal of Fluid Mechanics* **224**, 361–382.

Swaters, G. E. (2003), 'Baroclinic characteristics of frictionally destabilized abyssal overflows', *Journal of Fluid Mechanics* **489**, 349–379.

Tanaka, K. (2006), 'Effects of the Earth's rotation and bottom slope on a density current descending a sloping bottom', *Journal of Geophysical Research-Oceans* **111**(C11).

Tanaka, K. & Akitomo, K. (2001), 'Baroclinic instability of density current along a sloping bottom and the associated transport process', *Journal of Geophysical Research-Oceans* **106**(C2), 2621–2638.

Torrence, C. & Compo, G. (1997), 'A practical guide to wavelet analysis', *Bullentin of the American Meteorological Society* **79**(1), 61–78.

von Gyldenfeldt, A. B., Fahrbach, E., Garcia, M. A. & Schroder, M. (2002), 'Flow variability at the tip of the antarctic Peninsula', *Deep-Sea Research Part II-Topical Studies In Oceanography* **49**(21), 4743–4766.

Whitehead, J. A. & Chapman, D. C. (1986), 'Laboratory observations of a gravity current on a sloping bottom - the generation of shelf waves', *Journal of Fluid Mechanics* **172**, 373–399.

Wilfried, J. & Oerter, H. (1997), Die Expedition ANTARKTIS-XII mit FS Polarster 1995, Bericht vom Fahrtabschnitt ANT-XII/3, Reports on Polar Research, Technical Report 219, Alfred Wegener Institute for Polar and Marine Research, Bremerhaven.

Willebrand, J., Barnier, B., Boning, C., Dieterich, C., Killworth, P. D., Le Provost, C., Jia, Y. L., Molines, J. M. & New, A. L. (2001), 'Circulation characteristics in three eddy-permitting models of the North atlantic', *Progress in Oceanography* **48**(2-3), 123–161.

Wåhlin, A. K. (2002), 'Topographic steering of dense currents with application to submarine canyons', *Deep-Sea Research Part I-Oceanographic Research Papers* **49**(2), 305–320.

Wåhlin, A. K. & Walin, G. (2001), 'Downward migration of dense bottom currents', *Environmental Fluid Mechanics* **1**, 257 – 259.

Wåhlin, A., Darelius, E., Cenedese, C. & Lane-Serff, G. (2007), 'Laboratory observations of enhanced entrainment in the presence of submarine canyons and ridges.', *Deep Sea Research* (submitted).